Montanuniversität Leoben

Microstructural investigation of a Fe-Co-Mo alloy by means of SANS and atom probe analysis

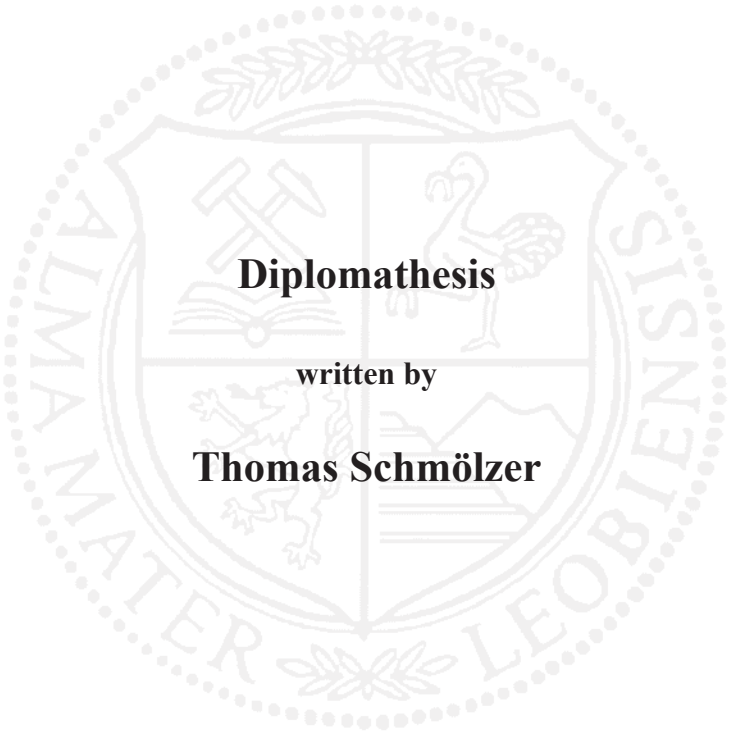

Diplomathesis

written by

Thomas Schmölzer

This thesis was conducted at the Department of Physical Metallurgy and Materials Testing at the University of Leoben.

Affidavit

I declare in lieu of oath, that I wrote this thesis and performed the associated research myself, using only literature cited in this volume

Leoben, 10.08.08

Thomas Schmölzer

Preface and Acknowledgements

After a year of experimenting, analyzing and countless discussions with the collaborators, this diploma thesis has now finally come to a close. The completion of this work marks not only the end of my graduate studies, it is also my first work of scientific significance and therefore the first step on the path I chose to pursue for the next three years in the course of my PhD thesis.
This diploma thesis allowed me to delve deeply into the various difficulties that are faced if a material is characterized on a nanometre scale and taught me to act with care if analysis methods are pushed to – and sometimes beyond – their limits. However, no matter how tedious some tasks that arose during this thesis were, the admiration for the technology that enables us to comprehend a material with near atomic resolution never faded.
I would not have been able to complete this thesis without the support of numerous people that are thankfully acknowledged in the following:

Thank you to Univ.-Prof. Dipl.Ing. Dr. mont. Helmut Clemens for giving me the possibility to conduct this thesis at his department and for showing a personal interest in this work.

I especially want to thank Dipl.Ing. Elisabeth Eidenberger who invested large amounts of time and energy in advising me. Without her help and scientific vision, I never would have been able to write this thesis.

I'm grateful to all the PhD students of the department who were always eager to give advice and always came through for me. Special thanks to Dipl.Ing. Erich Stergar and Dipl.Ing. Michael Schober who made me familiar with the atom probe technique and conducted a large number of experiments, the results of which I used in this thesis.

Thank you to the staff of the Department of Physical Metallurgy who were always supportive and who maintain an ideal environment for doing research.

I'm deeply indebted to my parents who always supported me and raised me to become an inquisitive and ambitious person.

I've gained a colleague and friend during my time at the university that never fails to cheer me up and never stops ignoring my numerous shortcomings. Thank you, Laura.

Thank you to my colleagues and friends at university; Christof Kirchlechner, who is always up for acting as an intellectual sparring partner; Georg Rathmayr, Kurt Satzinger and Michael Reichhart for reminding me that there are things apart from university; My housemates, Karin Ratschbacher, Ines and Simone Goldgruber and Christian Streicher who were always there if I needed somebody; and to Eva Eidenberger who kept me company in my dark moods.

Table of contents

Abbreviations

APT	**A**tom **p**robe **t**omography
CCD	**C**harge-**c**oupled **d**evice
FIM	**F**ield **i**on **m**icroscope
FWHM	**F**ull **w**idth at **h**alf **m**aximum
GKSS	**G**esellschaft für **K**ernenergieverwertung in **S**chiffbau und **S**chiffahrt mbH; Research facility in the vicinity of Hamburg, Germany. Because the research focus has shifted since its founding, only the abbreviation is in use nowadays.
ICF	**I**mage **c**ompression **f**actor
IVAS	Name of the software provided by Imago Scientific Instruments Ltd.
LEAP	**L**ocal **e**lectrode **a**tom **p**robe
MCP	**M**ulti **c**hannel **p**late
PE	**P**oly**e**thylene
PoSAP	**Po**sition **s**ensitive **a**tom **p**robe. Also the name of a software for analysing atom probe data provided by Imago Scientific Instruments Ltd. (originally by Oxford nanoScience Inc.)
PTFE	**P**oly**t**etra**f**luor**e**thylene
SANS	**S**mall **a**ngle **n**eutron **s**cattering
SAS	**S**mall **a**ngle **s**cattering
TEM	**T**ransmission **e**lectron **m**icroscopy
TOF	**T**ime **o**f **f**light
UHV	**U**ltra **h**igh **v**acuum
3DAP	**3 d**imensional **a**tom **p**robe

1 Introduction

Precipitation hardened steels are both economically and ecologically interesting materials that exhibit high strengths and – depending on alloy design – high ductility. To be able to design materials for special applications, it is necessary to understand the principles that govern precipitation hardening. Model alloys offer the opportunity to investigate the ageing behaviour under well defined conditions.

Due to the unique combination of high spatial resolution and the possibility to investigate large sample volumes, scattering techniques are among the most powerful tools scientists have at hand for investigating a materials micro- and nanostructure. Unfortunately, the analysis of the obtained scattering patterns is not always straightforward and assumptions about certain sample properties have to be made. By comparing the results of scattering experiments to data gained by imaging techniques and other complimentary methods, it is possible to validate these assumptions and therefore to thoroughly describe the investigated material.

Over the last decades, the atom probe method has evolved from a tool for analyzing surface chemistry to an instrument that allows determining the chemical composition of bulk materials with near atomic resolution. Sample volumes have increased from a few hundred to 10^5 nm^3 allowing the extraction of statistically relevant data. The characteristic morphology and size of nano-structural features smaller than a few ten-nanometres can be analyzed.

In this thesis a Fe-25m%Co-15m%Mo alloy exhibiting age-hardening behaviour is investigated by means of atom probe tomography (APT) and small angle neutron scattering (SANS). Furthermore hardness tests are conducted to complement the microstructural data. Chemical information on the precipitates and the matrix obtained by atom probe tomography is used for interpreting the SANS patterns. The results of both methods are compared with respect to precipitate size and volume fraction and the discrepancies are discussed.

2 Theoretical background

2.1 Investigated material

2.1.1 Historical background

First papers on the Fe-Co-Mo system were published by Köster and Tonn in 1932 [1, 2]. They suspected that the two intermetallic compounds Fe_3Mo_2 and CoMo constitute a continuous solid solution that was referred to as the θ–phase. Furthermore, alloys in this system show age-hardening behaviour similar to that of precipitation hardened Al-alloys, the material being soft after solution annealing and quenching and exhibiting a considerable increase in hardness during ageing at elevated temperatures. Another property of Fe-Co-Mo alloys is the high thermal stability of its intermetallic precipitates [1, 2].

One of the major drawbacks – and probably one of the reasons why alloys of this system haven not been used in engineering applications – is their extreme brittleness which was pointed out by Houdremont already in 1956 [3].

Further investigations on Fe-Co-Mo alloys were carried out during the 1960's and 70's, primarily in the USSR. Geller [4] investigated the effects of adding V, Ni, Cr, and C. He reported a maximum bending strength of 2600 MPa and toughness values of up to 0.14 MJ/m^2 [4]. In 1975, Geller described the strengthening of low-carbon, high alloy tool steels by intermetallic phases.

The so-called μ-phase with the elemental formula $(Fe, Co)_7(W, Mo)_6$ forms in steels of high thermal stability alloyed with Co, W and Mo. The crystal lattice is hexagonal and the lattice parameters are a=4.74 Å and c=25.48 to 25.63 Å. The hardness of this phase was determined to be 1100 HV [4].

For carbon-free martensite the estimated hardness increase due to the formation of intermetallic precipitates can be as high as 20-40 HRC in contrast to 3-10 HRC that can be achieved by the formation of carbides. Furthermore, the maximum volume fraction precipitated is larger for intermetallics than for carbides. This was verified by electrical conductivity measurements [4, 5].

Investigations by Miyazaki et. al. [6], published in 1979, showed that the precipitates in a Fe-20at%Mo alloy are formed by spinodal decomposition. Doi et. al. [7] report on the development of an ultra high strength steel in which precipitation hardening occurs by spinodal decomposition. In this work, a ternary alloy with a composition of Fe-22 at% Co-8.2 at% Mo was so brittle that tensile tests could not be conducted [7].

In 1984, Raynor and Rivlin [8] published a review paper on ternary alloys of Fe, Mo and Co and assessed the validity of the phase diagrams that were the basis of earlier investigations. They pointed out, that the binary phase diagrams of the Fe-Mo and Co-Mo systems were erroneous and Köster and Tonn therefore came to wrong conclusions concerning the type of intermetallic phases that precipitate upon ageing [8].

The systems that were the basis of Köster and Tonns work contained only the σ-Phase and a phase denoted Fe_3Mo_2. The phase Fe_2Mo was not considered and there was confusion between the R and Fe_7Mo_6 phases. There are also differences between the currently accepted phase diagram of the Co-Mo system and the phase diagram Köster and Tonn used. Now it is assumed that the σ and the Co_7Mo_6 phase are both formed by peritectic reactions. Furthermore, the phase diagram that constituted the basis for earlier investigations contained only the phase CoMo; the phases θ and κ (Co_3Mo) were not considered. [8]

All early studies on alloys of the Fe-Co-Mo system were carried out using specimens that were produced by conventional melting technology [1-8].

In 1998, Karpov et. al. [9] published their research activities about producing alloys for cutting applications by powder metallurgy techniques. Studies were performed on two different alloys, alloy 1 (Fe-25 m% Co-14 m% W-7.5 m% Mo-0.6 m% V) and alloy 2 (Fe-23 m% Co-12.5 m% Mo-4 m% W-0.6 m% V). It was shown, that 97-99% of the true density of the alloys could be attained by liquid phase sintering. Furthermore it was demonstrated, that the liquid phase disappeared during the sintering process. The hardness values after the solution treatment and subsequent annealing reached 71 HRC. Even after annealing at 700°C, the hardness did not decrease below 60 HRC [9].

Investigations about the microstructure by Transmission Electron Microscopy were conducted by Izdinsky et. al. [10] in 2000. They revealed that an orientation relationship between precipitates and the bcc matrix can be established [10].

2.1.2 The Ternary Phase Diagram Fe-Co-Mo

Figure 1 shows the binary diagrams bounding the ternary Fe-Co-Mo system [8]. In the phase diagram Fe-Co a continuous γ-solid solution is formed, while in the Fe-Mo and Co-Mo systems a series of intermetallic compounds occurs (Fig. 1).

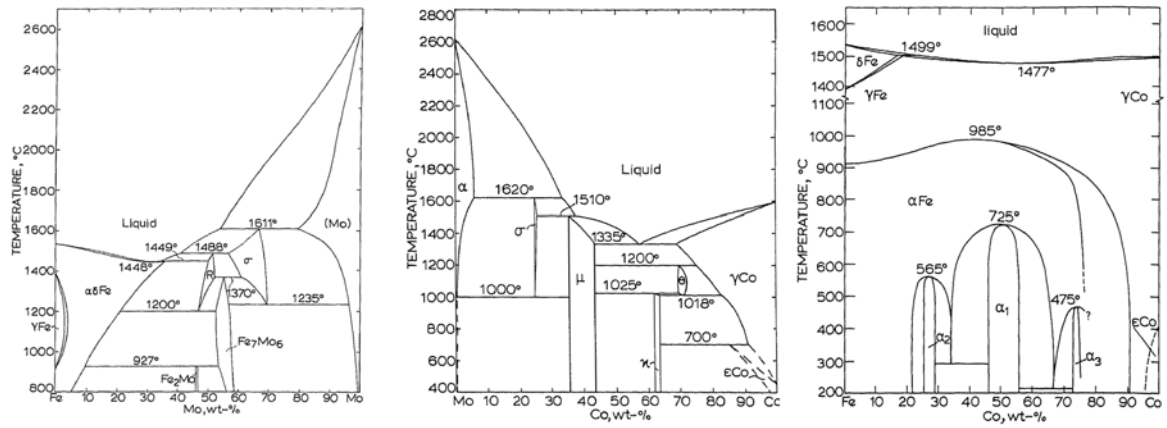

Fig. 1: Binary phase diagrams for the systems Fe-Mo, Mo-Co and Fe-Co [8].

In the Co-Mo system, the intermetallic σ-phase with the composition Co_2Mo_3 [8] is the product of a peritectic reaction of melt and a molybdenum based solid solution at 1620 °C.

The μ-phase with the composition Co_7Mo_6 and a rhombohedral lattice is formed in a subsequent peritectic reaction of melt and σ at 1510 °C and remains stable to room temperature.

For the Fe-Mo system, the sequence that leads to the formation of the μ-phase with the composition Fe_7Mo_6 is quite similar. At 1611 °C, Fe_3Mo_2 forms as a result of a peritectic reaction between melt and Mo based solid solution, the R-phase is the product of another peritectic reaction of melt and σ at 1488 °C. In a third peritectic reaction at 1370 °C these two phases form the μ-phase which is again stable down to room temperature. Since the μ-phase exhibits the same crystal structure and has similar lattice parameters in both systems, a continuous solid solution of Fe_7Mo_6 and Co_7Mo_6 is formed in the ternary system Fe-Co-Mo. Ternary Fe-Co-Mo alloys can be characterized by the primary precipitates formed during solidification. There are six primary phase fields distinguishable, which are presented in Figure 2.

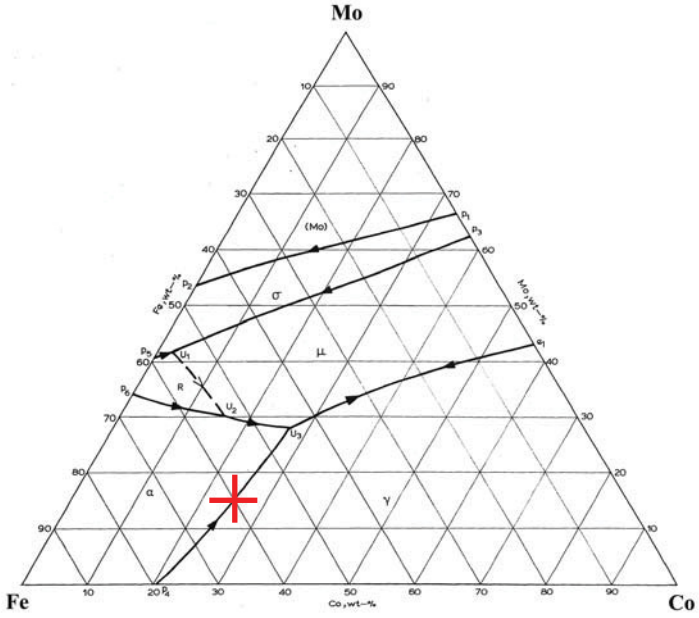

Fig. 2: Projection of the liquidus-surfaces of the Fe-Co-Mo system [8]. The composition of the investigated alloy is marked by the red cross.

If alloys in the α- or γ-field are solidified rapidly, the formation of μ-phase can be suppressed and a supersaturated solid solution is obtained. Ageing of this solid solution enables the system to approach the thermodynamic equilibrium and leads to the precipitation of the intermetallic μ-phase, which constitutes the basis for the age hardening behaviour.

2.1.4 The μ-phase

The μ-phase is a topologically close-packed intermetallic compound with a rhombohedral crystal structure. Its composition is described as $(Fe,Co)_7Mo_6$ in the Fe-Co-Mo system. In

this system, the μ-phase forms a continuous solid solution between the Fe_7Mo_6 and Co_7Mo_6 phases present in the binary system involved. This behaviour can be attributed to the fact, that the phases in the binary systems exhibit the same crystal structure and that its lattice parameters are quite similar (Tab. 1).

Tab. 1: Lattice parameters of the μ-phases in the involved binary systems [8]

Phase	a [nm]	c [nm]	c/a
Fe_7Mo_6	0.4754	2.571	5.409
Co_7Mo_6	0.4767	2.565	5.381

It is possible to suppress its formation by rapid cooling. If the supersaturated solid solution formed is subjected to elevated temperatures, the precipitation of μ-phase occurs. If the precipitation reaction takes place in a crystal with bcc structure, the following orientation relationship can be established between the precipitates and the matrix [10].

$$(1\text{-}10)_\alpha\,[110]_\alpha \parallel (110)_\mu\,[001]_\mu$$

This orientation-relationship enables the coherent precipitation of the μ-phase in a ferritic matrix [6]. Detailed investigations about the structural units the μ-phase consists of have been published in [11].

2.2 Atom probe analysis

2.2.1 Introduction

The atom probe (AP) as it is used today, is a microscope that provides chemical information on the analyzed volume with near atomic resolution in three dimensions.

The first atom probes consisted of two parts; a classical field ion microscope (FIM) and a time-of-flight mass spectrometer. The FIM provided a highly magnified projection of the specimen's surface that enabled the operator to select an atomic scale region for chemical analysis. Atom probes nowadays are able to investigate sample volumes in the range of 10^5 nm^3 and have become valuable tools for conducting investigations on the chemistry of bulk materials.

2.2.2 Basic principles

2.2.2.1 The field ion microscope (FIM)

In the field ion microscope, the specimen that has been prepared to a sharp tip is mounted onto a cryostat and oriented along a vacuum tube (Fig. 3). The vacuum tube is filled with an image gas, typically helium or neon, to a pressure of roughly 10^{-3}Pa.

For both microscopy techniques – FIM and atom probe – Müller [12, 13] exploited the effect of field ionization. In order to field ionize atoms strong electric fields (in the order of

10^{10} V/m) must be applied. Müller was able to realize that by utilizing the strong field enhancement that can be obtained by using sharply pointed specimens. The field F_0 at the apex of a pointed object is given by

$$F_0 = \frac{V_0}{k_f \cdot r_0} \qquad \text{[Eq. 1]}$$

where V_0 is the applied potential, r_0 is the apex radius and k_f is a numerical constant which attains values between 2 and 5 [14]. Voltages necessary for enabling field ionization attain values of a few thousand Volts for tips that have radii in the range of 10^{-7} m.

At the high positive potential applied, nm-sized inhomogeneities of the specimen surface polarize atoms of the image gas. These polarized atoms are drawn towards the apex of the tip where they hit the surface and loose part of their kinetic energy. The atoms may get trapped in the high field region near the tip where they experience further collisions with the specimen surface and are confined to an ever narrowing region of space close to the surface. If the applied electrical field is high enough, atoms beyond a critical distance from the surface are field ionized and repelled by the positively charged tip. The ions are accelerated in radial direction towards the fluorescent screen where they produce a magnified image of the specimen surface.

The limited number of ions that could be desorbed from the surface proved to be a major difficulty that was solved by Müller by admitting a small amount of hydrogen into the vacuum chamber containing the specimen. Later, the hydrogen was replaced by inert gases, typically helium and neon. Another improvement made during the early days of Field Ion Microscopy was to cool the specimen to cryogenic temperatures which enhanced the spatial resolution dramatically. By 1956, the FIM had evolved to such an extent, that it was able to reveal extensive details about the atomic structure of the solid surface [15].

Is the applied field raised to higher values, not only image-gas-atoms may be ionized, but also atoms from the specimen surface are removed by field evaporation. These atoms occupying the most prominent lattice sites on the specimen surface are field desorbed first and a hemispherical tip is formed. It is possible to control the rate of field evaporation in such a way, that surface atoms may be removed one-by-one [16].

The contrast in the FIM-image is obtained by variations in the electric field close to the emitter surface. This can be attributed to the atomic structure as well as to chemical inhomogeneities of the surface leading to variations in the field ion current over the specimen surface. The magnification of the FIM is determined by the ratio of specimen-to-screen distance to specimen tip radius and is usually in the order of 10^6 [17]. A schematic layout of a FIM is shown in Figure 3.

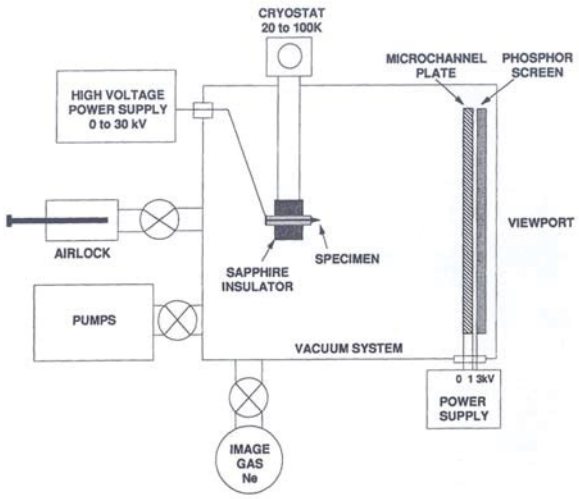

Fig. 3: Schematic drawing of a field ion microscope. [18]

FIM images usually show sets of intersecting concentric rings that reflect the atomic terraces of crystallographic planes on the specimen surface. The brightly imaging regions correspond to sites where field ionization can easily occur, i.e. above the edge or the corners of atomic terraces. A ball model of a hemispherical tip is shown in Figure 4.

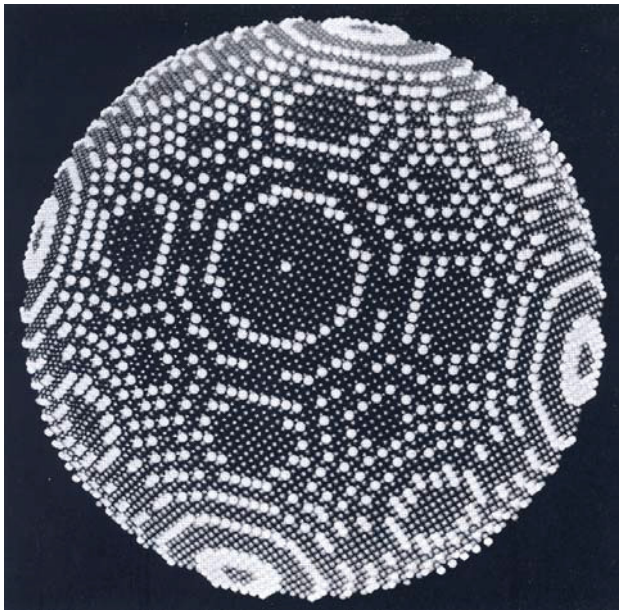

Fig. 4: Ball model of a hemispherical tip. The white atoms indicate prominent lattice sites on which ionization occurs preferentially. The model represents an fcc lattice with the (001) plane at the center and four {111} planes left, right, top and bottom of the model [18].

Hence the overall pattern resembles a stereographic projection of the surface and can be indexed by standard techniques. Crystal defects such as line and planar defects can be identified by the displacement in the concentric ring patterns they cause [16]. In a poly-phase material the magnification of the FIM can vary over the surface, since due to the different evaporation fields of different phases a hemispherical tip may not be obtained. That phase

which requires stronger fields to evaporate forms small ‘bumps’ on the hemispherical tip. These regions which exhibit higher curvatures than the specimen tip cause a locally raised magnification that usually cannot be accounted for in the analysis of the FIM image. Further information can be found in the publications of Müller [12, 13], Müller and Tsong [19] and Melmed [20].

2.2.2.1 The atom probe

The first atom probe (AP) that enabled to select a particular area from the FIM specimen for chemical analysis was developed in 1968, when Müller [12] utilized the time-of-flight principle for analyzing the field desorbed ions with respect to their element type. A small probe aperture was incorporated into the FIM screen that acted as an entrance into the time-of-flight mass spectrometer. Mounting the specimen on a stage that could be rotated and tilted allowed the operator to select a small part of the FIM image for chemical analysis. This is possible only because the trajectories of the image gas ions and the field desorbed ions are considered equivalent. In order to allow the determination of the atoms chemical identity, the detector used in the spectrometer had to have single atom sensitivity [21].

The basic method to conduct an atom probe experiment with this setup would be to produce a field ion image on the screen first. Then, the spot to be analyzed is selected by adjusting the specimen in such a way, that the image of the desired region lies on the “blind spot” of the phosphor screen, which indicates the circular aperture of the spectrometer. After that, the image gas is removed from the vacuum chamber and high voltage pulses are applied to the specimen in order to field evaporate surface atoms. The pulses are usually 10-20 ns in length and generated by discharging a capacitor into a load with a resistance of typically 50 Ω [18].

Only those field evaporated ions whose trajectories lead them through the aperture are analyzed in the mass spectrometer. Since the potential energy of an atom on the surface at an applied voltage V_0 equals the kinetic energy of the field evaporated ion, the mass to charge ratio can be calculated according to:

$$\frac{m}{n} = 2 \cdot e \cdot V_0 \cdot \frac{t^2}{d^2}, \qquad \text{[Eq. 2]}$$

where d is the length of the ion trajectory, e is the elementary charge and t is the flight time of the ion. This equation is only valid under the assumption that the ions attain their final velocity instantaneously which is actually a good approximation of the observed behaviour [18]. In the time-of-flight mass spectrometer the mass of an ion cannot be determined independently from its charge state. Information on the natural abundances of isotopes as well as assumptions concerning the most probable charge states help to assign the right element to the observed mass-to-charge ratio (m/n). This is usually done by looking at the mass-to-charge spectrum of a number of ions collected from the specimen and assigning an

element type to a certain range of *m/n* values. It is beneficial to this step, that the number of complex molecules (such as VN^{2+} etc.) formed during the evaporation of surface atoms is small and the ambiguity introduced by that effect is usually of minor importance. Although the basic principle of the atom probe is simple, special care has to be taken when choosing the operating parameters such as specimen temperature, standing voltage and pulse fraction to prevent artefacts from occurring [18].

Since the late 1960 the instruments have undergone a rapid development. Limitations have been overcome and modern instruments are able to analyze sample volumes of considerable size and with high spatial resolution. Important development steps on the way from the relatively simple time-of-flight or conventional atom probe to today's tomographic atom probe will be described in the following.

2.2.3 Important instrument components

2.2.3.1 Energy compensating systems

One important improvement was to introduce energy compensating systems to atom probe microscopes. This is necessary since not all ions exhibiting the same mass to charge ratio acquire the same amount of energy during one evaporation pulse. For the duration of the voltage pulse, the electrical field and, therefore, the field evaporation rate is constant. If an atom is field ionized after half of the pulse duration, it has an energy deficit compared to an atom that is field ionized right at the beginning of the voltage pulse. This is because the second ion is subjected to the high electric field of the voltage pulse for a significantly shorter time span. Therefore, it fails to acquire as much energy as the atom that is evaporated first. In addition to that, there are inherent energy losses, termed ion appearance potentials, which are negligible in comparison [22].

Two different approaches were used to realize an energy compensating system. The Poschenreider lens consists of two electrodes that form a 163° sector of a toroid, in which the inner electrode is charged negatively while the outer electrode is positively charged (Fig. 5).

Ions that have lower energy are deflected through the lens close to the inner wall, which entails a shorter flight path and therefore compensates for the longer period of time it takes the ion to fly through the drift tube. In order to obtain both, time and spatial focusing of the ions, the parameters of this energy compensating lens have to be chosen with special care. The Poschenreider lens improves the mass resolution at full width of half maximum (FWHM) from $m/\Delta m=250$ to $m/\Delta m=2000$ [22]. The second energy compensating lens is referred to as reflectron. This is an electrostatic lens which consists of a series of circular electrodes with linearly increasing potential and produces a uniform electric field that is penetrated deeper by ions with higher energy, which in turn have a longer flight path (Fig. 6). Unlike the Poschenreider lens, the reflectron does not reduce the background noise but allows conserving the information about the lateral position on the specimen the ion emerged from. With higher order reflectrons it is possible to obtain mass resolutions of up to

35000 FWHM [23] at the expense of ion transmission. Frequently, first order reflectrons are used that allow mass resolutions of roughly 1200 FWHM [22].

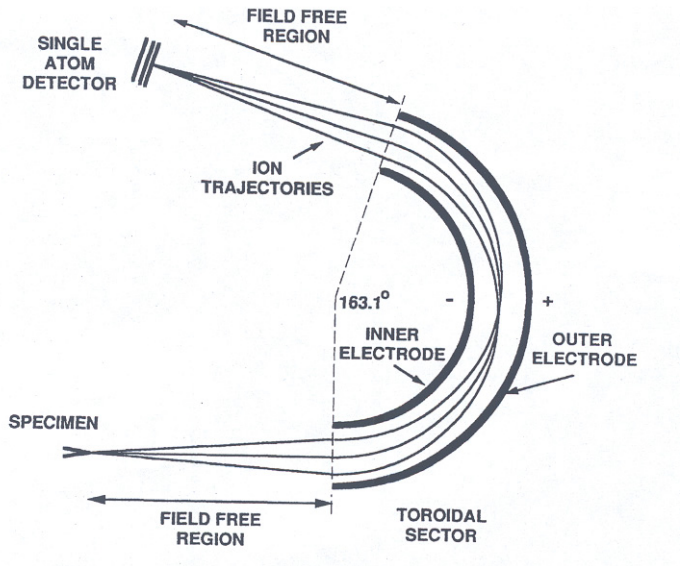

Fig. 5: The Poschenreider energy compensating lens [24].

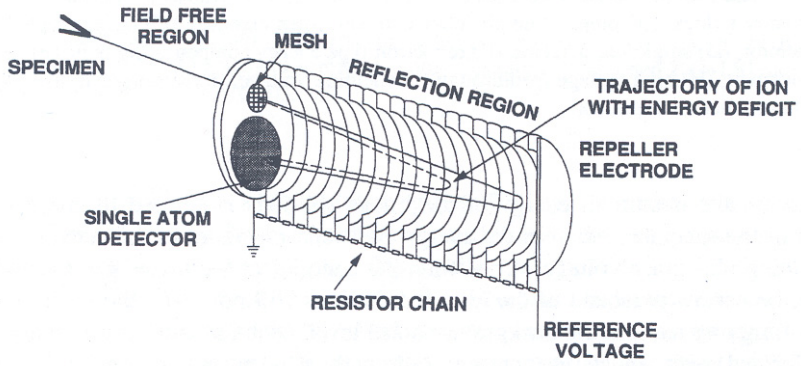

Fig. 6: The reflectron-type energy compensating lens. [24]

2.2.3.2 Atom detectors

In the conventional atom probe design, spatial resolution and analyzed volume are contradicting objectives. To overcome this limitation, position sensitive ion detectors were introduced to the design of atom probes in 1988 [25, 26]. This allows to determine the flight time and the position at which the ion hit the detector and, therefore, to reconstruct the analyzed specimen volume in three dimensions. The first instruments only allowed detecting one ion per pulse correctly, while modern multianode array detectors are able to analyze multiple hits. With this improvement made, it was possible to operate at higher evaporation rates and thereby higher data acquisition rates. Early versions of the tomographic atom probe also had a very limited mass resolution of $m/\Delta m$=50-250 at FWHM [27]. Commercially

available systems nowadays are equipped with energy compensating lenses and allow mass resolutions of up to m/Δm=1200 at FWHM [28].

2.2.3.3 Laser pulsing

Another development that enlarged the application field for the atom probe technique was the pulsed laser atom probe first realized by Kellog and Tsong in 1980 [29]. Before the introduction of this method, only materials exhibiting low electrical resistance could be analyzed in the atom probe. With the pulsed laser atom probe, also semiconductors and a wider range of surface chemical phenomena can be investigated. In this method, instead of applying a high voltage pulse, a laser pulse with durations in the pico-seconds range is directed to the apex of the specimen. The incident laser beam causes ions to field evaporate at the standing voltage without causing the energy spread that ions which are evaporated by a voltage pulse are subjected to [30]. Using laser pulses to field evaporate atoms has one additional advantage over using voltage pulses. If high-voltage pulses are applied, the specimen is exposed to high mechanical loads and prevalently fractures, thereby destroying the specimen tip and terminating the experiment. The fracture of a tip is often referred to as "flashing" of the specimen. Especially if poly-phase materials with large differences in the evaporation fields of the incorporated phases are investigated and high pulse to standing voltage ratios have to be used, specimens fracture frequently and complicate the acquisition of a sufficiently large amount of data. If using laser pulses for inducing field evaporation, the specimen tips are less prone to flashing.

One drawback of the laser pulsing technique is that due to the lower field and the higher temperatures more molecular ions are formed which affect the analysis of the mass spectrum.

2.2.4 Data reconstruction

The raw data that are obtained during an experiment with a tomographic atom probe are a sequence of numbers that indicate the time of flight and the coordinates at which the screen was hit for every single detected ion. For converting the raw data into a dataset that contains information on the element type and position of each detected ion, software packages that lead through the reconstruction process and perform all calculations necessary are used. Nonetheless, the operator has to make several choices regarding the reconstruction process.

First, the operator has to choose which ions are to be used for the reconstruction. This is done by plotting the applied standing voltage over the number of detected ions and selecting the first and last ion to be considered (Fig. 7). The ideal case would be a steadily increasing voltage curve with no incontinuities. Especially at the beginning of the atom probe run, oxide layers or other contaminating species may be present at the surface of the specimen that can be abruptly removed from the surface, thus creating a sharp drop or rise in the voltage curve. In general, the first part of an atom probe experiment should be removed if the focus lies on analyzing the bulk material. Fractures of the needle tip can also occur during a run. As long

as the increase in standing voltage is not big enough to terminate the run, it is possible to resume the AP experiment. In this case, only the ions collected before or after the flash are to be considered for reconstructing the sample volume [31] (Fig. 7).

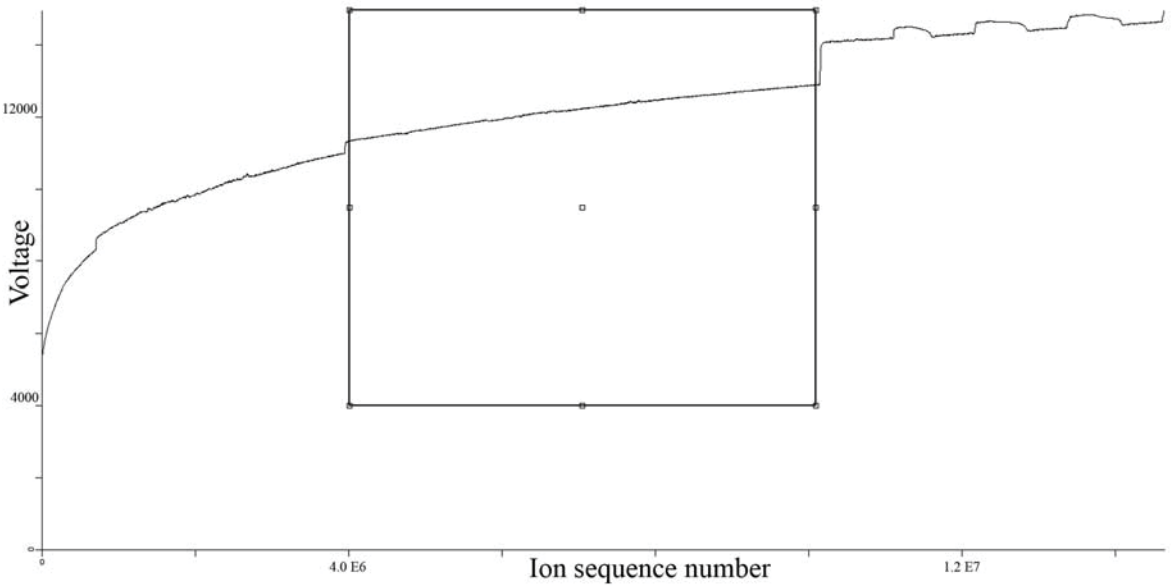

Fig. 7: The diagram shows a voltage evolution curve obtained from an AP experiment on the Fe-25 m% Co-15 m% Mo. Only the ions collected in the range designated by the black window are used for reconstruction. Before and afterwards incontinuities can be observed in the voltage evolution that indicate flashes.

In Figure 7 a voltage evolution curve is shown in which several sharp increases in evaporation voltage are visible that indicate the occurrence of flashes. Only ions collected in the range that is indicated by the black window were used for reconstruction.

Converting the time-of-flight data into a mass-to-charge ratio spectrum is the next step, which is almost entirely performed by the software. The only input necessary is to select at least two (recommended are four) peaks of the mass to charge spectrum that are used for calibrating the mass-to-charge ratio scale. This is usually done simply by choosing two prominent peaks and assigning the right elements with the correct charge states to them [31].

An important step in reconstructing the analyzed specimen volume is to assign certain mass-to-charge ratio windows (referred to as “ranges” in the following) to the appropriate elements. From field evaporation, ions with different charge states may be obtained from one elemental species. In addition to that, for every charge state one element can be represented by several peaks, each peak corresponding to one of the elements isotopes. For assigning the right element type to each peak, it is helpful to have information about the possible charge states an element might attain. It is also useful to know the chemical composition of the analyzed material in order to use it as a benchmark. For some materials, a significant amount of molecular ions may be formed. Frequently, these compounds are carbides, nitrides and hydrides as well as carbo-nitrides. If precipitates are present in the analyzed volume, and

information about the composition of these precipitates is available, it may help to check if the unidentified species is segregating to the precipitates.

Dependent on the mode in which the atom probe experiment was conducted, the width of the ranges used for the analysis of the spectrum should be chosen in different ways. For runs performed in the voltage mode, the mass spectrum consists of peaks that are fairly symmetrical. In cases where laser pulses were used to field evaporate atoms, the peaks have a very well defined onset, but exhibit a pronounced tail towards higher m/n ratios (Fig.8). This peak shape can be attributed to the fact, that the laser pulse is very short (in the range of femto- to pico-seconds), and most atoms evaporate immediately. However due to the finite cooling rates there is a small fraction of atoms that field evaporates a considerable time span after the pulse heated the material. These ions cause the element peaks to acquire a tail towards higher m/n rations. In the case of this investigation the ambiguity introduced by this effect is negligible.

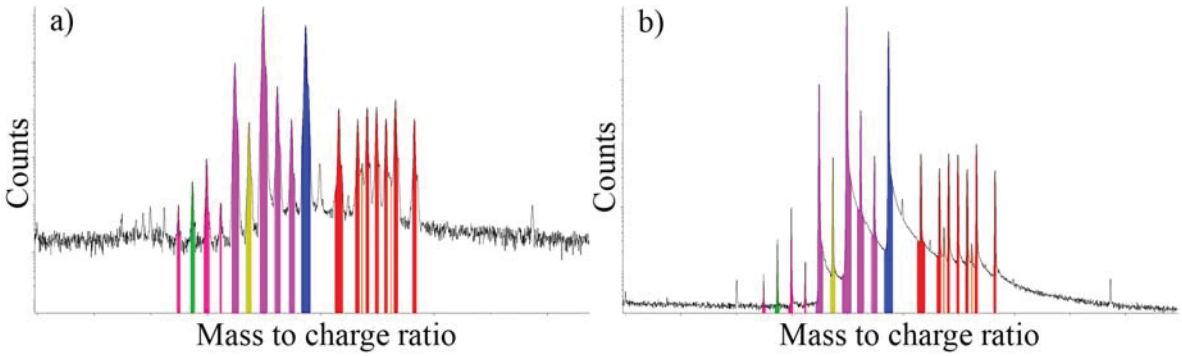

Fig. 8: Excerpts from mass-to-charge spectra obtained in AP-experiments on a Fe-25 m% Co-15 m% Mo alloy. The spectrum shown in a) was obtained in the voltage mode, while that in b) was produced by conducting the experiment in the laser pulsing mode.

It is therefore common to define rather narrow ranges in a range file used on datasets obtained in the laser pulsing mode.

If peak overlaps occur in the mass spectrum, special care has to be taken to deconvolute these peaks properly. In the case of peak overlaps between one species that is much more abundant than the other species, the entire peak may be assigned to the more abundant species. However the composition determined in the atom probe experiment then no longer reflects the exact composition of the specimen. Another possibility to deconvolute the overlapping peaks would be to use information about the abundance of isotopes of one element. This is done by calculating the fraction of one species that contributes to the peak by assuming that the ratio in which isotopes of one element occur corresponds to the peak heights of different isotopes with the same charge state. The major drawback of this technique is that the spatial information on the species, which are represented by the overlapping peaks, can not be obtained [32].

The last step in reconstructing the analyzed volume is to convert the data acquired during the experiment into a three dimensional dataset. First, the volume of the sample is calculated by multiplying the total number of ranged ions by the individual ion volumes. The volumes that are assigned to the ranged ions are bulk molar volumes, crystallographic structure or the presence of chemical compounds are not taken into account. After that, the specimen tip radius r_0 is calculated by assuming that the evaporation field strength of the specimen equals the evaporation field strength of the main specimen constituent (Eq. 3) [31].

$$r_0 = \frac{V_0}{(k_f \cdot F_0)}, \qquad \text{[Eq. 3]}$$

where V_0 represents the applied voltage, F_0 the evaporation field of the main alloy constituent and k_f is a numerical constant that depends on the taper angle of the specimen. k_f is also called the field factor and typically attains values around 5. Accurate values for the field factor k_f can be determined by producing a hemispherical tip in the FIM at a certain applied voltage V_0 and determining the obtained tip radius r_0 by TEM.
The magnification of the atom probe depends on the radius of the apex r and therefore changes during the course of an experiment. It can be estimated by

$$M \approx \frac{d}{r \cdot ICF}, \qquad \text{[Eq. 4]}$$

where d represents the distance between specimen and detector and ICF is the Image Compression Factor that attains typically values around 1.3 [31]. For reconstructing the shape of the analyzed sample volume, different models can be utilized. One possibility is to assume a conical shape, with a spherical cap on top. In this case, the initial and final apex radii are calculated by the voltage applied at the beginning and at the end of the experiment. Another course of action would be to use the so-called voltage evolution model. In this case, the shape of the analyzed volume is derived from the variation of the applied standing voltage with the number of field evaporated ions. Usually the voltage evolution mode is the method of choice unless e. g. layered structures in which different layers exhibit different evaporation fields are analyzed [31].
The next step is to transform the x,y coordinates at which an ion hit the detector into the x,y coordinates at which the ion was located in the specimen by using a transfer function (x,y being the coordinates that are perpendicular to the analysis direction). The z coordinate of an ion is derived from the evaporation sequence. Further information on the reconstruction process can be found in [33].
The result of the data reconstruction is a file in which every ranged ion is assigned a set of coordinates and an elemental (or molecular) identity. Frequently, the reconstruction is shown

as dot map in three dimensions in which different colours are assigned to different element types (Fig. 9).

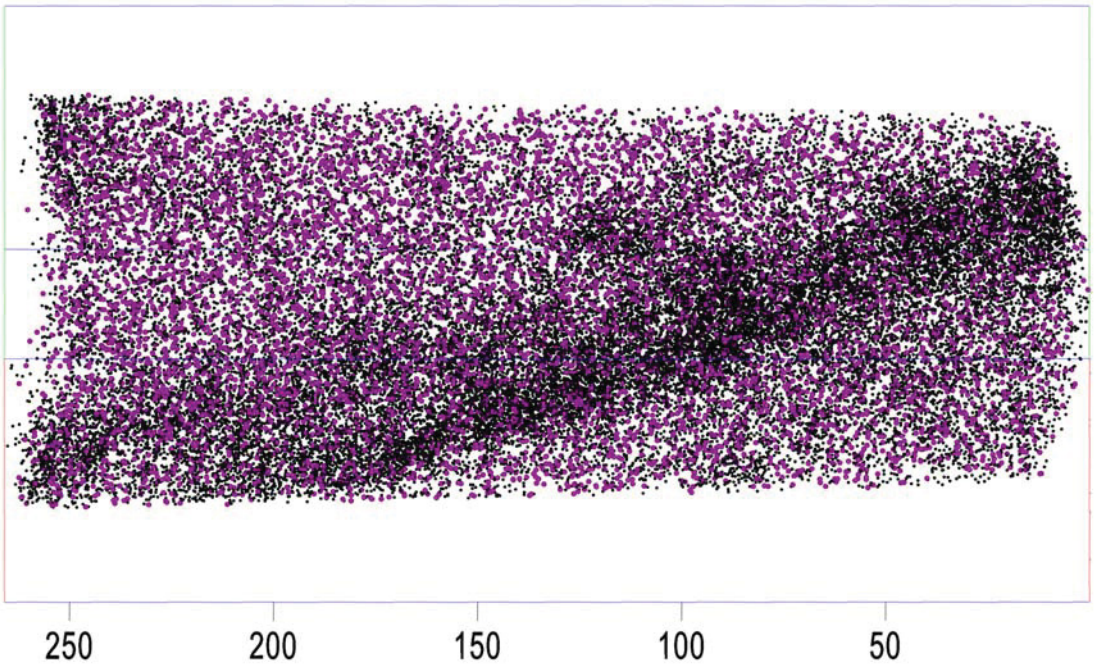

Fig. 9: Dot map image of a reconstructed specimen tip of a Fe-25 m% Co-15 m% Mo alloy. Each dot represents a ranged ion, violet dots indicate P, black ones C ions, the dimensions are indicated in nm. Regions of high C concentration indicate the presence of an interface. The shape of the tip was determined by using the voltage evolution mode.

Sometimes, characteristic microstructural features of the investigated material are visible by just looking at the dot map (Fig. 9). However, as the amount of data increases, it gets harder to comprehend the information contained in the image. To assist the user in analyzing the data obtained with the atom probe, different routines performed by the computers have been developed. These methods will be discussed in the following section.

2.2.5 Data analysis

As mentioned before, the early versions of atom probes suffered from relatively small sample volumes and were not able to retrieve the x,y position of the detected ion in the specimen. Although modern instruments allow collecting a much larger data volume, tools that were developed to process data obtained by conventional atom probe experiments are still in use.

2.2.5.1 Composition profile

Probably the analysis method most frequently used for conventional atom probe data is to calculate a composition profile. For this purpose, the data are divided into blocks (so-called bins) that are of fixed volume or contain a fixed number of atoms. If determining concentrations on a length scale in the range of nanometres, the presence of two

contradicting objectives becomes effective. The larger the number of atoms in one bin is, the lower is the statistical sampling noise and the lower is the spatial resolution. Choosing a bin size that exceeds the size of the feature present in the analyzed volume will result in aliasing the data. Typical values for bin sizes are between 25 and 100 atoms per bin. For the conventional atom probe, the bin size is determined by the diameter of the mass spectrum aperture and the bin's extension in z direction. These two parameters are not to be chosen independently, they should be adjusted in such a way, that the bins are about as wide as long. In a three dimensional atom probe (3DAP) experiment, no choices concerning the bin size have to be made while conducting the experiment, all necessary parameters can be adjusted while analyzing the data. It is also possible to calculate two dimensional concentration profiles out of 3DAP data.

2.2.5.2 Composition in 3-D

If compositions are to be evaluated in three dimensions, this is usually performed by using a concept that's different from that utilized for calculating one- or two-dimensional concentration profiles. The analyzed volume is subdivided into voxels which can have different sizes in x,y,z direction and whose edges form a grid. A typical voxel would be a cube with an edge length of 0.1 nm. Then, a delocalization function is superimposed on every detected ion, which is centred at the position where the ion was detected. Concentrations are calculated for all grid points by adding up all values of the delocalization functions of all ions at every single grid node (Fig. 10).

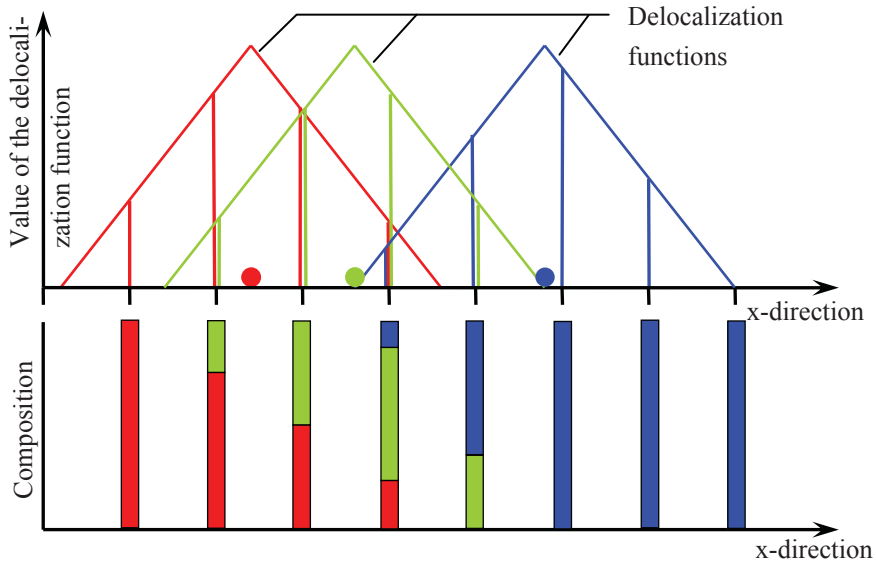

Fig. 10: Illustration of the delocalization function concept.

In Figure 10, the filled circles represent ions that hit the detector at a certain point along the x-axis. Every colour corresponds to a different elemental species. On these ions, delocalization functions of the saw-tooth type are imposed, which are centred on the ion

position. The coloured vertical lines show the values of the delocalization functions at the grid points, which are represented by short black lines. In the bottom part of Figure 10, the composition at the grid nodes is indicated.

Different delocalization functions are available, although center-weigthed delocalization functions are used most frequently. Typical center-weighted delocalization functions are the saw-tooth or the Gauss function. If a Gauss function is chosen, it is convenient to use a spline function to approximate it, since the Gauss function has the major drawback that it decreases to small values relatively fast, but attains zero only at infinity. Replacing it with a spline allows to attain zero at finite values, which gives the advantage, that only delocalization functions of ions within a certain range of the grid node at which the concentration is calculated have to be taken into account. In the case that a spline is used, the amount of delocalization is determined by setting the distance that corresponds to six times the standard deviation of the delocalization function. The larger the delocalization distance is chosen, the lower is the statistical sampling noise and the lower is the spatial resolution [34].

The calculation of a 3D concentration grid is the basis for numerous methods used for analyzing 3DAP data. Some of these methods and the algorithms used are introduced in the following.

2.2.5.3 Fourier transformation

An elegant method to analyze an AP dataset with respect to microstructural features such as a dominating wavelength of composition fluctuations is to apply a Fourier-transformation to atom probe data. For transforming AP-data it is necessary to use the discrete Fourier-transformation since the composition values are only available at the grid nodes. The discrete Fourier-transformation $F(\omega)$ of a composition profile is defined as

$$F(\omega) = \sum_{i=0}^{n_b-1} c_i \cdot \exp\left[2 \cdot \pi \cdot \sqrt{-1} \cdot i \cdot \omega\right], \qquad \text{[Eq. 5]}$$

where c_i is the composition of the i^{th} block and n_b is the number of composition blocks. $F(\omega)$ is the amplitude of the spatial frequency ω in the composition profile [35]. For better visualization, the Fourier transform is usually multiplied by its complex conjugate to obtain the power spectrum. Peaks observed in the power spectrum are an indication of a periodic composition fluctuation, whose wavelength λ can be calculated from the frequency at which the peak is located by the following relation.

$$\lambda = \frac{N \cdot l}{2q\pi} \qquad \text{[Eq. 6]}$$

Where N is the number of bins, l is the length of one bin and q is the position of the peak in reciprocal space.
The Fourier transformation is the representation of the 3DAP data in reciprocal space and performing a Fourier transformation is therefore the mathematical pendant to the physical process of conducting a scattering experiment (see Chapter 2.3).

2.2.5.4 Autocorrelation function
Calibrating the autocorrelation function is a procedure that enables to obtain information similar to that extracted from the power spectrum, but is used more frequently than the Fourier transformation to analyze atom probe data [35]. The autocorrelation coefficient R_k can be calculated as follows

$$R_k = \frac{1}{\sigma^2} \cdot \sum_{i=1}^{n_b-k} (c_i - c_0) \cdot (c_{i+k} - c_0), \qquad \text{[Eq. 7]}$$

where c_i and c_{i+k} are the compositions of the i^{th} and the $i+k^{th}$ blocks, c_0 is the mean composition, n_b represents the total number of blocks and σ is the variance given by

$$\sigma^2 = \sum_{i=1}^{n_b} (c_i - c_0)^2 \,. \qquad \text{[Eq. 8]}$$

Often, the autocorrelation function is written with an additional term in order to compensate for the different number of terms in the summation ranges [35]:

$$R_k = \left[\frac{n_b}{n_b - k} \right] \cdot \frac{\sum_{i=1}^{n_b-k} (c_i - c_0)(c_{i+k} - c_0)}{\sum_{i=1}^{n_b} (c_i - c_0)} \,. \qquad \text{[Eq. 9]}$$

If the compositions c_i and c_{i+k} are either larger or smaller than the mean value, the autocorrelation coefficient is strongly positive, while the autocorrelation coefficient is negative if they attain values that are on different sides of the mean value (Fig. 11). The autocorrelation function is the average of the autocorrelation coefficient for the composition profile plotted for different lags k between the blocks compared, divided by the variance of the composition profile [35].

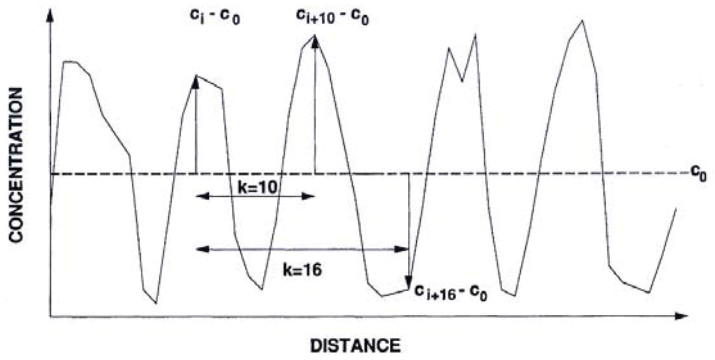

Fig. 11: The composition values that are k=10 units apart will generate a positive autocorrelation coefficient because both of them have values larger than c_0. The composition values that are 16 units apart will have an autocorrelation coefficient that is negative. The autocorrelation function is the average of the autocorrelation coefficients of one composition profile for different lags k, divided by the variance [35].

By definition the autocorrelation coefficient lies between -1 and 1 and the autocorrelation coefficient R_0 is always 1. In alloys containing a particle size distribution, the first minimum (i.e. the minimum value between the two first zero crossings) corresponds to the average particle diameter, while the first maximum (i.e. the largest value after the second zero crossing) gives the average particle spacing. Figure 12 shows a composition profile and the autocorrelation function calculated for this composition profile.

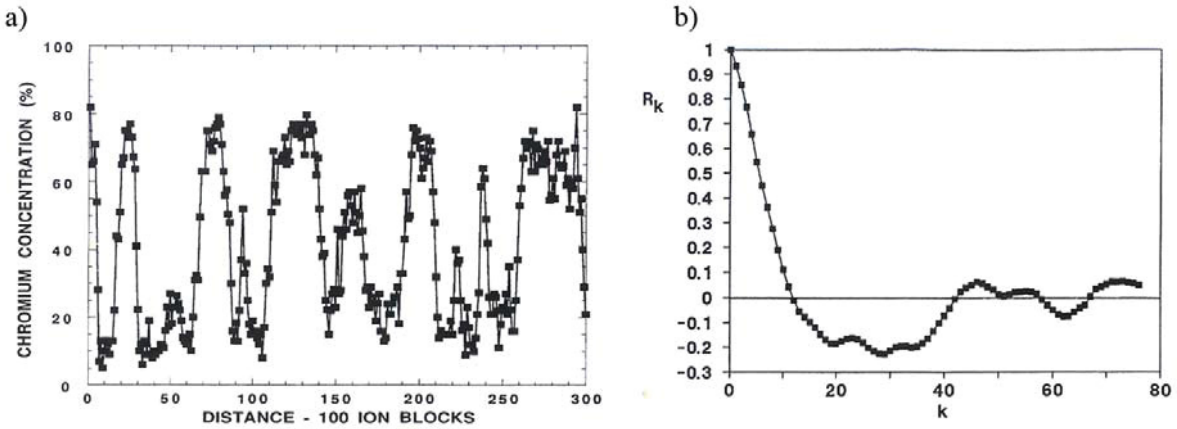

Fig. 12: a) shows a composition profile of a Fe-45% Cr alloy aged for 485 h at 525°C. A phase separation is clearly evident. In b) the autocorrelation function calculated from the composition profile is shown. The first minimum lies at k=29, while the first maximum can be found at k=47 [36].

The autocorrelation exhibits one advantage compared to many other analyses methods because its shape is rather insensitive to variations of the bin size. This is true as long as the bin size is small enough not to average over regions that are larger than the size of the microstructural features present. An extension to this analysis method would be to perform a computer simulation with different particle size distributions rather that a single particle size and to compare the curves obtained with the experimental data [35].

2.2.5.5 Frequency distribution

A method to quickly evaluate if decomposition has occurred in a volume analyzed by 3DAP is to calculate a frequency distribution. For that, the analyzed volume is divided into blocks of constant volume or constant number of contained ions. One or more elemental species are selected for which the frequency distribution is calculated. Then the number of blocks that lies within a composition range of the selected species is evaluated and plotted versus the composition of that species [36].

If no decomposition has occurred, the frequency distribution is a binomial distribution. For specimens that exhibit a strongly pronounced phase separation, the frequency distribution has two peaks, one peak corresponding to the matrix composition and the other to the precipitate composition. Frequently decomposition is only indicated by the frequency distribution deviating from a binomial distribution (Fig. 13).

However, this behaviour will only be observed as long as the bin size chosen is smaller than or in the range of the size of the composition fluctuations [36].

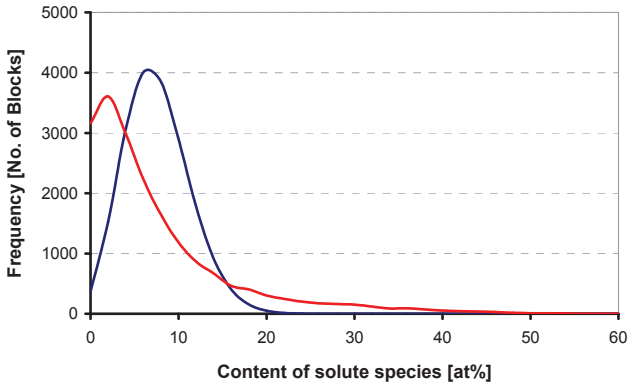

Fig. 13: Exemplarily, this diagram shows the result of a frequency distribution analysis. The red line indicates the observed frequency distribution, while the blue curve represents a binomial distribution for the same average composition. It is clearly evident, that decomposition has occurred.

2.2.5.6 Isoconcentration surfaces and proxigrams

One of the most common ways to interpret and present 3DAP data is the use of isoconcentration surfaces. The user of the computer program employed is able to choose one elemental species and to set the concentration threshold at which the isosurface is to be constructed. Some programs (e.g. IVAS from Imago scientific instruments) allow the operator to construct an isosurface for a combination of elemental species as well as constructing an isodensity surface. The position of isoconcentration surfaces is determined as follows: First a three-dimensional grid is calculated in which composition values are assigned to the grid nodes. The way in which this is conducted is described in Section 2.2.5.2. The smallest elements of an isosurface are polygons whose corner positions are computed by linear interpolation between the concentration values of two neighbouring grid nodes, one exhibiting a higher and the other one a lower concentration than indicated by the

concentration threshold. All polygons combined form a surface that confines regions with concentrations higher than the threshold concentration from the rest of the analyzed volume (Fig. 14) [37].

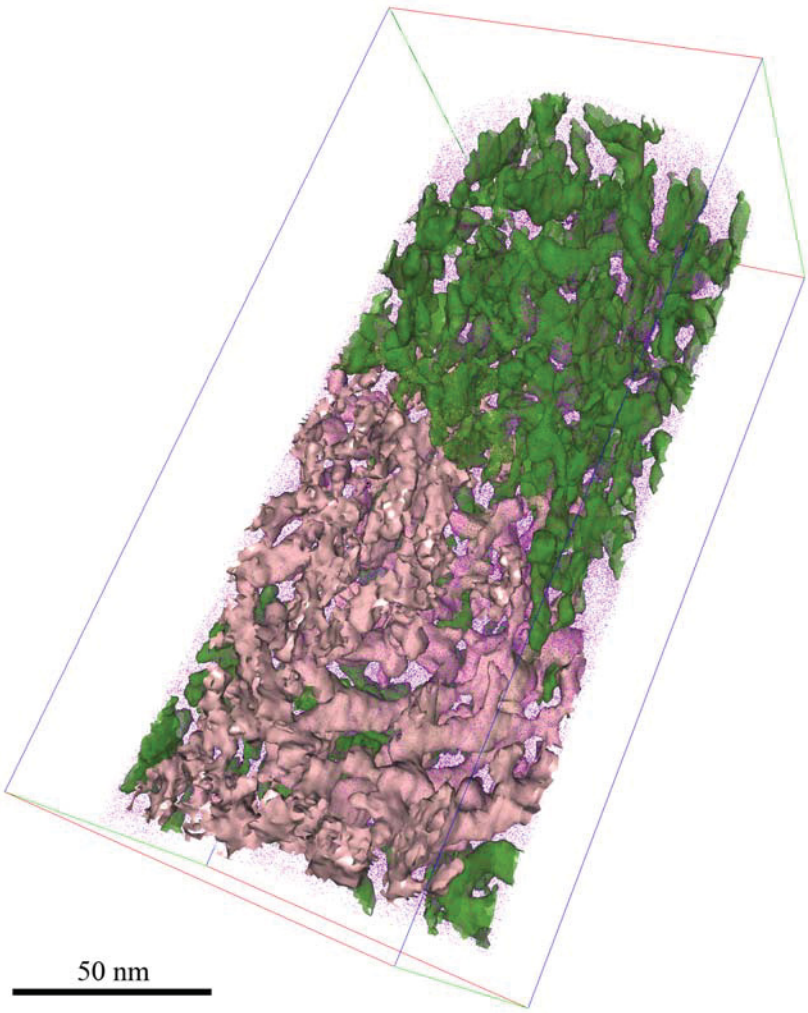

Fig. 14: Isosurfaces calculated for a concentration threshold of 20 at% Mo in a Fe-25 m% Co-15 m% Mo alloy after ageing for 10000 min at 500 °C. The pink structure is a single isosurface which emphasizes the highly interconnected structure of the precipitates present. The volume of the cube shown is 62·62·185 nm^3.

This method is used to identify interfaces such as phase boundaries, grain boundaries or interfaces between precipitates and the surrounding matrix. Special care has to be taken if the sizes of the microstructural features that are investigated are in the range of the width of the delocalization function used for calculating the composition at the grid nodes. In that case, the use of isoconcentration surfaces for determining the size or volume of the features may lead to erroneous results.

The chemical composition in the vicinity of the isoconcentration surface can be characterized by calculating a proxygram. For every polygon of the isosurface, a composition profile

perpendicular to the triangle is calculated. The average of all these composition profiles constitutes the proxygram (Fig. 15).

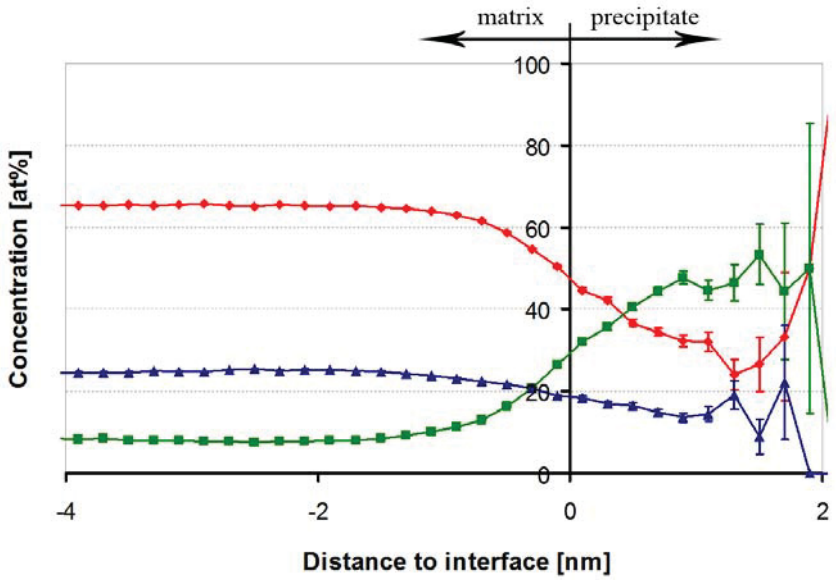

Fig. 15: Proxygram of isosurfaces that confine precipitates in a Fe-25 m% Co-15 m% Mo alloy aged at 500 °C for 300 min. The Fe concentration is represented by the red curve, Co and Mo concentrations are indicated by the blue and green curve, respectively.

To understand the limitations of this method, it is useful to have a look at the way it is implemented in the commercial software packages used for analyzing AP data. On the abscissa of the proxygram, negative values indicate distances from the isosurface in the direction of the negative gradient of the concentration, while positive values indicate distances from the isosurface towards higher concentrations. When calculating a proxygram, the user has to choose a bin size that determines both, the amount of statistical noise and the spatial resolution. Then the distance from one atom to the closest polygon of the isosurfaces for which the proxygram is calculated is evaluated. The atom is then assigned to the bin that corresponds to this distance. This sequence is repeated for every atom in the dataset and the composition of every bin is computed [37]. Since in some bins the number of atoms is low, the error-bars may be rather large (see Fig. 15). Errors caused by the statistical sampling noise can be estimated by

$$\sigma = \sqrt{\frac{C_i \cdot (1 - C_i)}{N}}, \qquad \text{[Eq. 10]}$$

where C_i is the calculated atomic fraction of each species i and N is the total number of atoms in each bin [37].

It is necessary to note that the proxygram feature was developed to enable the user to investigate the chemical composition only in the immediate vicinity of an interface and that

special care has to be taken if used for other purposes in order to avoid misinterpretations [37].

2.2.5.7 Cluster search algorithms

Since the isosurface method suffers from limited spatial resolution and is therefore not able to provide information about the very early stages of precipitation and clustering, a different approach is used by so-called cluster search algorithms.

The basic idea behind those is that in a cluster the separation distance between the atoms of the species, which forms these clusters, is lower than that in the matrix. This corresponds to a higher concentration value of the species, but eliminates the need for applying some kind of delocalization function to the dataset and thereby increases the spatial resolution. In addition to the separation distance, all cluster search algorithms allow the operator to choose values for the minimum number of atoms in one cluster and the so called surround distance. The minimum number of atoms per cluster sets a lower threshold for the cluster size, while the surround distance determines to which extend atoms of other elemental species are considered to belong to the cluster [38, 39]. A step by step illustration of the basic cluster search algorithm is given in the following.

First, an arbitrary atom with the elemental identity chosen by the operator is picked. Then the distances to the nearest neighbours that are of the same elemental species are computed and compared with the separation distance as shown in Figure 16. If all distances are larger than this parameter, the atom does not belong to a cluster. For the case that one or more atoms of the species considered are closer than the specified maximum, these atoms are added to the cluster. Now again the distances between the newly added atoms of the cluster and their closest neighbours are being compared with the separation distance. This is repeated until no atoms of the selected species that are closer to one atom in the cluster than specified by the separation distance can be found. The next step is to compare the number of atoms in this cluster with the minimum number of atoms. If the cluster contains more atoms, the algorithm considers it as valid cluster; otherwise the atoms are assigned to the matrix. If a cluster was sufficiently large to fulfil the last requirement, it still consists solely of atoms that are of one species. In order to add other constituents to the cluster, the surround distance is used. As a last step, all atoms that are closer to one atom of the selected species assigned to a cluster than specified by the surround distance are added to the cluster (Fig 16) [38].

Several extensions to the basic cluster algorithm have been conceived and implemented into standard software packages. The software PoSAP distributed by Imago Scientific Instruments (originally Oxford nanoScience Ltd.) uses an additional parameter in its cluster search algorithm, the so called erosion distance. Here, one more step is added to the basic cluster search algorithm. In this step an interface between the cluster and the surrounding matrix is generated. All atoms that are part of the cluster and occupy positions that are closer to this interface than specified by the erosion distance are removed from the cluster and

reassigned to the matrix. To put it simple, the algorithm removes an outer shell from the cluster with its thickness being equal to the erosion distance [38].

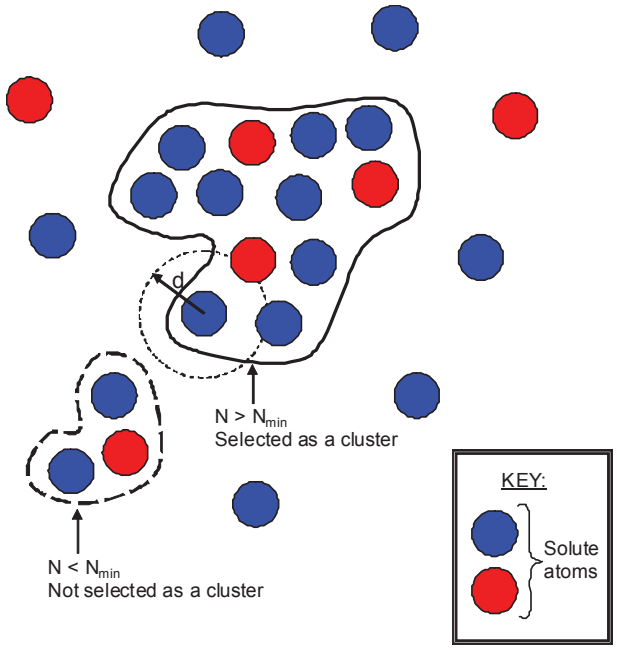

Fig. 16: Illustration of the Cluster Search Algorithm. d is the separation distance, N_{min} the minimum number of atoms for one cluster. The blue dots indicate atoms of the species subjected to the algorithm, while the red dots indicate atoms of another species. [39]

The crucial step in applying the cluster search algorithm successfully to a dataset is the choice of appropriate parameters. Choosing the species for which the algorithm is performed is straight forward, the only requirement being, that the species has to segregate to the clusters. It is advantageous if the concentration of the species in the precipitate is reasonably high since this enhances the spatial resolution of the method.

In several cases determining the right separation distance has proven to be much more difficult. If there is a steep concentration gradient at the precipitate-matrix interface, the separation distance that yields the best results can be evaluated by trial and error or by taking the concentration at which the concentration gradient between precipitate and matrix has its maximum and converting that concentration into a mean separation distance. Another method to evaluate a concentration threshold for the cluster detection is to use the frequency distribution diagram. If two distinct peaks can be identified, one corresponding to the composition of the precipitates and the other corresponding to the matrix, the separation distance that corresponds to the concentration of the species in between these two peaks should yield satisfying results. For materials that exhibit low concentration gradients at the interface between precipitates and matrix, the separation distance has a strong influence on particle size and particle composition, independently of how careful the parameters are chosen. It is useful to test the adequacy of the chosen separation distance on a simulated random distribution of solute atoms or on a dataset that was obtained from a solution treated

sample to evaluate the extent to which statistical fluctuations are considered to be precipitates by the algorithm [38].

In most cases the value of the surround distance has a smaller influence on the results of the algorithm. Usually the surround distance is assigned a value that is larger than the separation distance to take atoms present in the precipitate's core into account. Increasing the surround distance to large values may cause the precipitates to coalesce, which decreases the number density. For the erosion distance values between the surround distance and zero are usually chosen [39, 40].

The software packages used for analyzing the data in the course of this thesis are able to visualize precipitates that have been found by the search algorithm by showing all atoms that belong to these precipitates (Fig. 17).

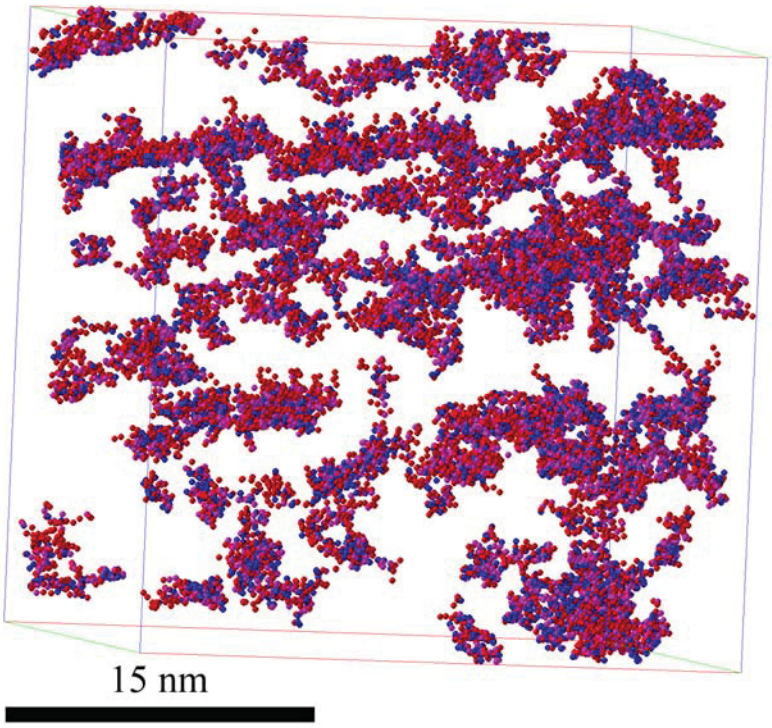

Fig. 17: Precipitates found by the cluster search algorithm in a Fe-25 m% Co-15 m% Mo alloy after ageing for 1000 min at 500 °C. The separation distance was set to 0.49 nm; The surround distance was assigned a value of 0.7 nm, the erosion distance was 0.6 nm. Fe atoms are represented by pink dots, Mo and Co atoms are red and blue, respectively.

IVAS as well as the PoSAP software allow the composition and the radii of gyration to be plotted for every single precipitate in the analyzed volume.

The cluster algorithm is a device for detecting small clusters and precipitates, but in some systems reacts very sensitive to small changes in the input parameters. Analyzing large datasets with the cluster algorithm also is rather time-consuming.

2.3 Small angle neutron scattering

Small angle neutron scattering (SANS) is a method capable of detecting nanometre sized regions with chemical or magnetic properties or densities different from that of the surrounding area. It is therefore well suited for analyzing precipitates even at very early stages of the precipitation process and allows investigating sample volumes in the range of several mm^3. The theory behind this method and its limitations will be discussed in this chapter. For further information on SANS the reader is referred to textbooks [41, 42]

2.3.1 Basics

Scattering occurs if the wavelength of the incident wave is in the range of the features that are probed in the material. Therefore, for neutron scattering experiments so-called cold neutrons with wavelengths of about 0.6 nm are used. These can be obtained by reducing the energy of neutrons that are either produced by a nuclear reactor or a spallation source in a moderator. Since neutrons have no electric charge, their interaction with matter is weak compared to that of X-rays. This is the reason for the high penetration depths (~10^{-2} m) neutrons show in most engineering materials. The brightness of neutron sources is much lower than those of synchrotron radiation facilities. Scattering experiments with neutrons therefore usually take much longer than those performed with synchrotron radiation.

2.3.2 Small angle scattering (SAS)

In general, Small Angle Scattering (SAS) provides information about chemical and density fluctuations within a sample; if neutrons are used, magnetic properties can be probed as well [43]. The term SAS may in some cases be misleading, since it does not actually refer to small scattering angles, but to small values of the scattering vector $\boldsymbol{q}$. For elastic scattering, the wave vector is defined as

$$q = \frac{4 \cdot \pi}{\lambda} \cdot \sin\left(\frac{\theta}{2}\right), \qquad \text{[Eq. 11]}$$

where θ represents the diffraction angle and λ is the wavelength of the radiation used. If the scattering vector $\boldsymbol{q}$ satisfies the following condition the experiment is considered to be a SAS experiment.

$$0 < p < \frac{\pi}{d_a}, \qquad \text{[Eq. 12]}$$

where d_a is the spacing between lattice planes in the material investigated. This condition is satisfied as long as the scattering angles are below half of that of the first Bragg Peak [44].

2.3.3 Contrast formation

The scattering behaviour of neutrons at a single nucleus can be described by the nucleus' scattering length b. Values for the scattering lengths are tabulated for all elements [45]. Another parameter that describes the interaction is the scattering cross section σ that is related to the scattering length by

$$\sigma = 4 \cdot \pi \cdot b^2 . \qquad \text{[Eq. 13]}$$

Values for b and σ are available for coherent as well as for incoherent scattering. For interference effects occurring during SAS experiments, coherent scattering is the dominant interaction effect. In contrast, incoherent scattering is isotropic and its contribution to the overall scattered intensity is relatively small. Only in cases where elements with large incoherent scattering lengths are present, incoherent scattering has to be taken into account by subtracting it from the obtained scattering curves [46]. In SANS experiments the neutrons interact with the specimen material in two different ways, one part of the scattered intensity results from the interaction between neutrons and the nuclei of the atoms of the material, while the other part is caused by the interaction between the magnetic moments of neutrons and specimen atoms.
In technologically important materials, phases that are solid solutions occur much more frequently than phases that consist of one elemental species. For a solid solution, the nuclear scattering length is calculated as follows:

$$b_i = \sum_{u=1}^{n} c_{a,u} \cdot b_u , \qquad \text{[Eq. 14]}$$

where b_i is the nuclear scattering length of phase i, $c_{a,u}$ represents the mole fraction of the element u within phase i, and b_u is the nuclear scattering length of element u [46].
Due to the fact, that the features investigated by SANS are much larger than the interatomic distances, the material can be treated as a continuum. This is done by relating the nuclear scattering lengths (b_i) of the phases present to their mean atomic volumes (v_i). The resulting parameter is called nuclear scattering length density $\eta_{nuc,i}$:

$$\eta_{nuc,i} = \frac{b_i}{v_i} . \qquad \text{[Eq. 15]}$$

The mean atomic volume can be obtained by

$$v_i = \frac{\langle A \rangle}{\rho \cdot N_A}, \qquad \text{[Eq. 16]}$$

where A is the mean atomic weight, N_A is Avogadros constant and ρ is the density of phase i [46].

In principle, magnetic scattering is treated similar to nuclear scattering, only the values for the scattering length densities are calculated in a different way. The magnetic scattering length density is defined by

$$\eta_{mag,i} = \frac{p_0 \cdot \mu_i}{v_i}, \qquad \text{[Eq. 17]}$$

where μ_i represents the relative mean magnetic moment per atom of phase i and p_0 ($2.7 \cdot 10^{13}$) is the magnetic scattering length in the order of magnitude of the classical electron radius [46]. If one element is the major constituent in one phase, the influence of the alloying elements on the magnetic properties of that phase can be calculated as follows:

$$\mu_M = \mu_i + \sum_{u=1}^{n} c_{a,u} \cdot s_u \,. \qquad \text{[Eq. 18]}$$

μ_M is the mean magnetic scattering length of the phase a, μ_i is the magnetic scattering length of the main phase constituent i, $c_{a,u}$ is the mole fraction of the alloy element u within phase a and s_u describes the influence of alloying element a on the magnetic properties of the main constituent i. For the case that the main constituent of the phase is Fe, the values of s_u for most alloying elements are tabulated in [47]. If SANS investigations on steels are performed, it is commonly assumed, that the precipitates are magnetic holes in a homogeneous, magnetically saturated matrix; i.e. the magnetic moment of these particles is assumed to be zero. Magnetizing the matrix to saturation is necessary, in order to avoid scattering from magnetic domain structures [44].

Spectra that are obtained by SANS are frequently analyzed using a relatively simple two phase model [48],

$$\frac{d\Sigma}{d\Omega}(q) = (\Delta\eta)^2 \cdot \int_0^\infty n(R) \cdot V(R)^2 \cdot F(q,R)^2 \, dR \,, \qquad \text{[Eq. 19]}$$

where $d\Sigma/d\Omega$ constitutes the macroscopic differential scattering cross section, $\boldsymbol{q}$ is the scattering vector, $\Delta\eta$ describes the difference in the scattering length densities of the phases

involved, *n(R)dR* represents the number density of particles in the matrix, *V(R)dR* is the volume of the particles that have radii between *R* and *R+dR* and ***F(q,R)*** is the form factor that depends solely on the shape of the particles present in the material [48]. For most cases it is sufficient to assume a spherical particle shape, in which case the form factor attains the following form [49]:

$$F(q,R) = 3 \cdot \frac{\sin(qR) - qR \cdot \cos(qR)}{(qR)^3} \qquad \text{[Eq. 20]}$$

If the particle sizes are not much smaller than the interparticle spacing, interparticle interference can occur. In that case an additional term has to be introduced in Equation 19 [43].
In a ferromagnetic material, nuclear and magnetic scattering of neutrons occur simultaneously. If the sample is magnetized to saturation, the scattering length density difference shows the following angular dependence.

$$(\Delta\eta)^2 = (\Delta\eta_{nuc})^2 + (\Delta\eta_{mag})^2 \cdot \sin^2\alpha \qquad \text{[Eq. 21]}$$

$\Delta\eta_{nuc}$ and $\Delta\eta_{mag}$ are the nuclear and magnetic scattering length density differences between particles and matrix while α denotes the angle between ***q*** and the direction of external magnetization. This equation is only valid if the chemical size of the precipitates is equal to their magnetic size and if unpolarized neutrons are used for the scattering experiments [44]. As a consequence of this angular dependency, it is possible to determine both, magnetic and nuclear scattering vectors with a 2d-detector simultaneously during the SANS experiment. Using these data, the so called A-factor can be calculated, which remains constant if the precipitates composition does not change and the assumptions of the precipitates nuclear and magnetic sizes being equal holds [50]:

$$A = 1 + \frac{(\Delta\eta_{mag})^2}{(\Delta\eta_{nuc})^2}. \qquad \text{[Eq. 22]}$$

By comparing the nuclear and magnetic contributions to the scattered intensity, not only structural, but also magnetic information on the investigated material can be retrieved. To be able to analyze the SANS data correctly, complementary methods have to be used to describe the development of the particles chemical and morphological properties throughout the precipitation sequence [43, 44, 50].

3 Experimental

The aim of this work was to investigate the evolution of the microstructure of a Fe-Co-Mo model alloy upon ageing by means of the tomographic atom probe method and to compare the results obtained with the data gained from small angle neutron scattering (SANS) experiments. In order to produce a supersaturated solid solution, the specimens were solution annealed and quenched. Subsequently the specimens were aged under isothermal conditions. Specimens subjected to different ageing times were analyzed with an atom probe and their microstructures compared. APT also provided data used in models for analyzing the microstructure by means of SANS. For providing additional information about the precipitation sequence, hardness tests were conducted.

3.1 Thermal treatment

All heat treatments performed in the course of this thesis were conducted with a Bähr DIL805 dilatometer. Although no dilatometric data were recorded, the dilatometer was chosen due to its accurate temperature control and the possibility to obtain high cooling rates in a very controlled and reproducible manner. Furthermore, it features the option to conduct the experiments in a low-pressure-atmosphere that prohibits undue oxidation of the specimen surface. The specimen is heated by an induction heating system with a water cooled high-frequency coil. This implies that the specimen has to have rotational symmetry to ensure a homogenous temperature distribution throughout the sample. An S-type thermocouple (Pt-PtRh) that had been spot welded to the sample surface was used for temperature control. All specimens heat treated in the dilatometer were 5 mm in diameter and 15 mm long. These dimensions were chosen to enable a simple specimen preparation for atom probe analysis.
Solution annealing was carried out at 1180 °C for 5 min. The cooling rate was set to a value of λ=0.3. The λ value is defined as follows [51]:

$$\lambda = \frac{t_{(800°C-500°C)}[s]}{100}, \qquad \text{[Eq.23]}$$

where $t_{(800°C\text{-}500°C)}$ is the time required to cool the specimen from 800 °C to 500 °C in seconds. The ageing treatment was carried out isothermally at a temperature of 500 °C with the heating rate set to 15 K/s, cooling was again conducted with a λ-value of 0.3. The different ageing times the specimens were subjected to are 0, 3, 6, 10, 20, 30, 60, 100, 300, 1000 and 10000 minutes.
Zero minutes denotes heating and immediate cooling of a sample in order to investigate the effect of the applied heating and cooling rates on the microstructural development.

3.2 Hardness testing

Since the hardness of an age hardenable material gives an indication of the extent to which a precipitation reaction has occurred, hardness tests were performed on the aged specimens. To complete the data basis, a solution annealed sample was tested as well.
The method of Vickers (HV10) was used for conducting the hardness tests on a Zwick 3212 testing device. To minimize time-dependent effects the load was applied for 15 sec. For validating the obtained values, three indentations per heat treatment state were made.

3.3 Optical microscopy

To complement the data on the heat treated material, specimens were prepared for examination in the optical microscope. The samples were cut with an ATM Brilliant 221 cutting device using SiN cutting discs. Grinding and polishing were carried out on a STRUERS TegraPol 31 equipped with a TegraForce 5 specimen manipulator.
Etching was achieved by 3 % HNO_3 in alcohol at ambient temperatures for samples aged for a sufficiently long time. Samples that were aged for times shorter than 20 min did not respond to etching with the aforementioned solution. In these cases etching was accomplished by applying a hot solution of W2 (16 g ferric chloride, 9 g ammonium persulfate, 60 ml hydrochloric acid 32 %, 60 ml distilled water) to the polished sample surface.
Examination of the samples was carried out with a Reichert-Jung Polyvar MET microscope with a ColorView Soft Imaging System CCD camera. Only qualitative examinations of the microstructure were conducted.

3.4 Atom probe microscopy

3.4.1 Specimen preparation

As a basis for the preparation of the needle-shaped atom probe specimens, rods with a cross section of 0.3x0.3 mm^2 and a length of about 10 mm were used. Four of these rods were extracted from every heat treated dilatometer sample by cutting with an ATM brilliant 221. Special precautions have to be made, to ensure that the surfaces of the rods are parallel to each other, and its cross sections are square in order to prevent obtaining tip shapes with an elliptical cross section upon subsequent etching. The aim of specimen preparation is to fabricate a smoothly tapering needle with an end-radius between 10 and 100 nm [52]. This was achieved by electropolishing the blanks in a two step process or alternatively by the so-called micropolishing technique. In the first step of the two-step process, an electrolyte of 25 % perchloric acid in glacial acetic acid is floating on an inert fluid (Galden) (Fig 18).

Fig. 18: In the two-step process the electrolyte (yellow) is floating on top of an inert fluid (transparent). The sample is moved up and down in the electrolyte to form a necked region.

A 0.3x0.3 mm^2 rod is fastened to a manipulator and a positive voltage is applied to the specimen. A gold wire is used as anode. In the corresponding literature, it is recommended to set the voltage between anode and cathode to 10 to 25 V [52]. During the course of this thesis it has proven to be convenient to apply a voltage of about 15 V. It is the goal of the first step to remove material from the specimen rapidly and to produce a tapering necked region. On this behalf, the sample is moved up and down during the polishing process to minimize preferential attack of the specimen at the electrolyte-air interface. As soon as the diameter of the sample in the necked region is sufficiently small, switching to the second preparation step is recommended. In this step an electrolyte of 2 % perchloric acid in 2-butoxyethanol is used. The necked region of the specimen is fully submerged in the electrolyte and a voltage of about 12 V is applied. As soon as the neck is unable to support the weight of the lower specimen part and fractures, the voltage is removed. By this technique two atom probe samples can be produced at the same time [53].

The tip preparation by this two-step process yielded very few samples that were suited for analysis in the atom probe. Most specimens were subjected to a micro-polishing treatment after accomplishment of the two-step process in order to obtain tips that were sharp enough for analysis. Micro-polishing is accomplished by putting a small drop of the electrolyte used in step two into a small loop made of gold wire. Again, the specimen is the cathode whereas the wire acts as anode. The amount of material removed at one spot of the sample is controlled by the amount of time this spot is close to the liquid-air interface while the voltage is being applied. A typical value for the voltage applied is 10 V. In principle, the procedure of shaping a sharp tip is similar to that in the two step process; a neck is formed and thinned until it fractures. In the last stage of thinning the neck, it is beneficial to apply the voltage only if the neck is moved outbound across the liquid-solid interface. Thereby, the adhesion of the small specimen part that is to be removed to the tip is avoided. All these preparation

techniques were monitored under an optical microscope with relatively low magnification (10x for the two step process, 20x for micro-polishing).
After electrochemical etching, the specimens were rinsed with isopropanol to remove surface contaminants. Then the specimen was carefully dried and examined by optical microscopy. If no contamination of the surface in the region close to the tip was visible, and the tip appeared to be sharp, the specimen was mounted on a specimen holder and put into the load-lock of the atom probe.

3.4.2 Atom probe setup

The atom probe employed for conducting the experiments is a LEAP 3000X Si imaging system, manufactured by Imago Scientific Instruments. LEAP is an abbreviation for Local Electrode Atom Probe. Employing a local electrode enlarges the field of view, so that a larger sample volume can be analyzed.
This instrument is equipped with a reflectron type energy compensating system and a laser pulsing unit in addition to the conventional voltage pulsing system. Cooling of the specimen is achieved by a so-called “cold finger”, which keeps the specimen at a fixed temperature of 20 K. In order to be able to control the temperature a heating device is installed, that increases the specimen temperature from the sample temperature of the cold finger to the temperature set by the operator.
To achieve single atom sensitivity, the detection system consists of a Multi Channel Plate that yields about 10^6 electrons per incident ion and a delay line detector in which less than 1 % of the ions are lost due to multiple hits. The overall detection efficiency of this detector setup is, therefore, governed primarily by the efficiency of the Multi Channel Plate.
For conducting the atom probe experiments, an ultra high vacuum (UHV) environment has to be maintained. Placing a specimen in the UHV chamber is achieved by using a system of load locks and specimen manipulators. For performing experiments with a local-electrode equipped instrument, it is important to ensure the accurate positioning of the specimen relative to the local electrode. If the specimen tip is not centred relative to the electrode aperture, a distorted image of the tip is obtained. The distance between specimen tip and the aperture plane has to be selected carefully to maximize the detectors field of view. In meeting both requirements, the user is supported by the atom probe software.
One important parameter for conducting atom probe tomography is the specimen temperature. Lower temperatures enhance lateral and depth resolution because diffusion is reduced and increase the standing voltage required for a sufficiently high evaporation rate at constant laser energy. In addition to that, fewer complex ions are formed during the experiment at low temperatures. If not indicated otherwise, the experiments for this thesis were conducted at specimen temperatures of 80 K.

3.4.3 Volume reconstruction and data processing

After conducting the experiments, the acquired data are stored in the .RRAW-file format in which all data are contained and organized as a single, variable length record per non-empty pulse. In contrast to that, the .RHIT-type files are organized as a single fixed length record per detected ion. .RHIT-files are the basis for the reconstruction of the tip geometry which is then stored in the .POS-file format. Reconstruction was carried out taking all peaks in the mass spectrum into account in order to ensure the accurate calculation of the specimen volume. The variation of field evaporation voltage with temperature was disregarded and the evaporation voltage of Fe at 77 K was used to calculate the tip radii. For an electrode setup like it is used in the LEAP the k_f-factor attains a value of 3. All reconstructions were conducted in the voltage evolution mode in which the shape of the standing voltage vs. number of evaporated ions curve is assigned to the shell of the reconstructed volume. These operations were performed with the commercially available IVAS software package. As mentioned earlier, the reconstructed dataset is stored in the .POS-file format in which every ion is represented by four fields in the following order:

- x-Position [nm]
- y-position [nm]
- z-position [nm]
- mass-to-charge ratio [u/e]

Information on the elemental identity of the peaks in the mass spectrum is stored in the range files which are identified by an .RNG or .RRNG extension. Assigning an element to the peaks in the spectrum is performed by the operator; details about this are given in Section 2.2.4. In this thesis, only elements of interest were assigned a mass-to-charge ratio in the range file. A picture of a typical mass spectrum with the elemental-ranges coloured is shown in Figure 19.

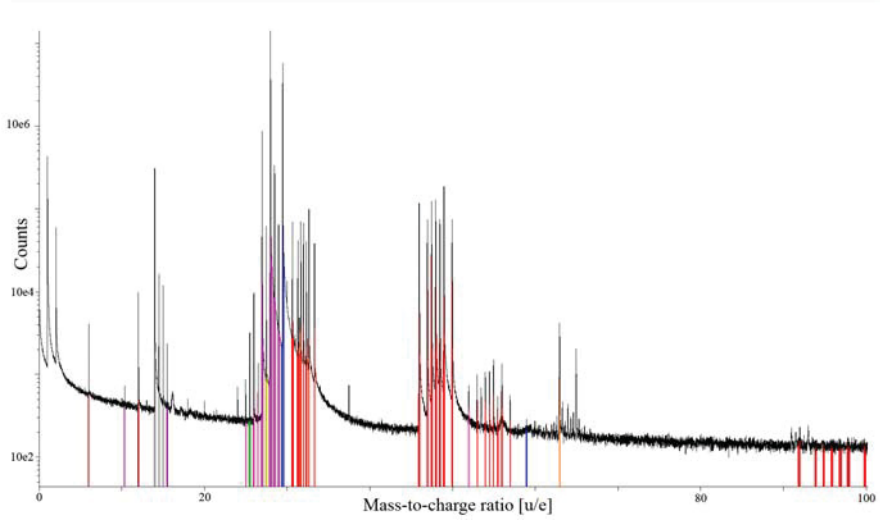

Fig. 19: Example of a mass spectrum and the ranges assigned to different elemental species. Red indicates Mo, Fe is coloured pink, Co blue.

3.4.4 Data analysis and interpretation

After finishing the reconstruction, the dataset was investigated with regard to the density distribution and the discontinuities in the distribution of C and P. In some of the datasets, strong segregations of these elements were observed which indicate the presence of an interface (Fig. 20). The regions in which these features were observed were ruled out for investigation of the precipitation sequence.

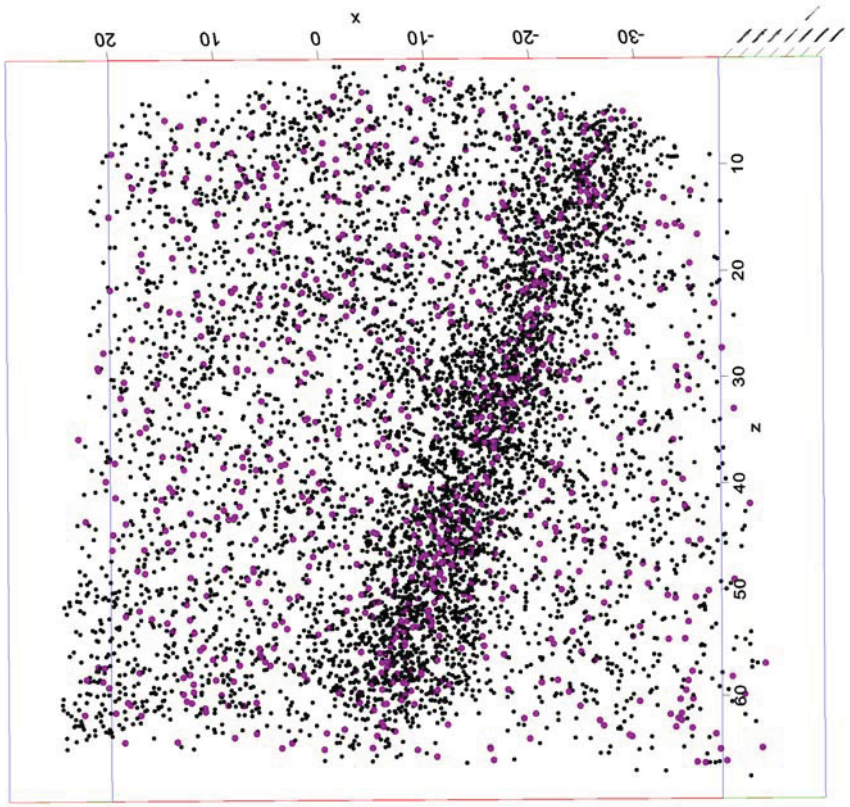

Fig. 20: Segregation of C (black) and P (violet) to an interface. The image was obtained from the Fe-25 m% Co-15 m% Mo model alloy, which was aged for 100 min at 500 °C. The dimensions are indicated in nm.

3.4.4.1 Frequency distribution

A quick way to retrieve information on the degree of phase separation in the material is to calculate a frequency distribution diagram. Since Mo clearly segregates to the precipitates, it was chosen to compute the frequency distribution for this solute element. If the obtained distribution in comparison to a binomial distribution shows a pronounced tail towards higher solute concentrations, decomposition is evident. For this type of investigations, the bin size was set to a value of 50 atoms per bin, which turned out to offer a fair compromise between a bin that is small enough not to average out small precipitates and large enough to offer statistics good enough for calculating a sufficiently accurate concentration value.

3.4.4.2 Isosurfaces

The enrichment of Mo in the precipitates allows identifying these by creating and displaying surfaces of constant Mo concentration. The parameters required for computing isosurfaces are:

- Elemental species of interest
- Threshold concentration
- Grid size
- Grid delocalization
- Minimum number of polygons

The elemental species of choice for the model alloy investigated is Mo. It segregates to clusters and is present in sufficiently high concentrations to enable small structures to be characterized. Since the measured Mo contents of the bulk material are about 7 at%, the threshold concentration has to be set to a value larger than that. In the course of this thesis, values between 15 and 20 at% yielded satisfying results.

In Section 2.2.5.2 the concept of calculating concentrations at the nodes of the grid that is established within the entire investigated volume is introduced and explained in detail. The distance between the grid nodes affects the spatial resolution that can be achieved by using isosurfaces for characterizing the nanostructure of materials. If the grid is too coarse the ability to resolve fine structures in the material is lost. For this reason, grid delocalization and grid size are two parameters that should not be chosen independently of each other. Using a large grid delocalization increases the number of atoms that contribute to the calculation of concentration values at the grid nodes and decreases the spatial resolution. In this work, a grid size of 0.5 nm and grid delocalizations of 1 to 5 nm were used.

Every isosurface consists of a number of polygons. Limiting the minimum number of polygons therefore entails neglecting isosurfaces that confine small artefacts. If this parameter was chosen too small, the computer used for conducting the investigations stalled and a java.long out of bounds exception warning appeared. Obviously, one problem of limiting the minimum number of polygons is, that smaller precipitates (or random fluctuations) are not displayed, and that it is not obvious how large the volumes of the largest precipitates that do not satisfy this condition are. In large datasets with a high volume fraction of particles, the minimum number of polygons required for avoiding a computer stall is as large as 200, thereby including clusters of considerable size.

The IVAS software package enables the user to export the volume that is enclosed by an isosurface as well as the surrounding volume as a .POS-file for further investigations. It also offers the opportunity to calculate the volume that is bounded by isosurfaces.

If isosurfaces have been constructed, a proximity histogram can be computed. The idea behind that step and the algorithm employed are introduced in Section 2.2.5.6. Only two input parameters have to be defined, namely the isosurface for which this operation should be performed and the bin size. Once again, a large bin size improves the statistical accuracy

while small bins facilitate a high spatial resolution. All proxigrams were calculated with a bin size of 0.2 nm which turned out to be a fair compromise between these two opposing demands. One thing to look out for is that considerable hardware resources are required for the computation of a proxygram if a large number of isosurfaces is chosen.

3.4.5.3 Fourier transformation and autocorrelation-function

In the corresponding literature it has been reported that precipitates in the Fe-Mo binary system form by spinodal decomposition [6]. This process usually facilitates the formation of a dominant wavelength within the microstructure. For identifying this feature Fourier-transformations of concentration profiles were performed. This was achieved with programs that were developed by the author of this thesis and written in the commercial software package Mathematica, which was chosen because it offers a routine that is able to Fourier-transform data arrays in n-dimensions. Concentration data were obtained by exporting the concentration values of one-dimensional concentration profiles as comma separated values from IVAS. These datasets were read by the Mathematica routines and transformed into a data-array suited for applying the Fourier-transformation routine to it. Visualization of the obtained power spectrum was achieved with standard graphics routines available in Mathematica. The source code of the programs written in the course of this thesis can be found in Appendix I. Concentration profiles used for these calculations were calculated from rod-shaped volume elements of the reconstructed sample volume with cross sections of 2x2 nm^2 and lengths corresponding to the datasets extension in z-direction. A bin size of 0.2 nm was used.

Another characteristic parameter that was calculated during analysis of the obtained data is the autocorrelation length. In principle, determining the autocorrelation length is similar to calculating a power spectrum in that respect, that it enables to evaluate the data for the presence of a dominant wavelength. This operation was performed with a software module enclosed in the PoSAP software. In PoSAP, values for the bin size, the maximum radius and the number of steps have to be chosen. These values were set to 0.1 nm, 5 nm and 30 respectively.

3.4.5.4 Cluster search

For determining the size, composition and volume of the precipitates present in the analyzed specimens, a cluster search algorithm was employed. The cluster search algorithm in the software package PoSAP allows selecting one additional parameter compared to the algorithm incorporated in IVAS and was therefore chosen for analyzing the datasets.

Following parameters have to be chosen:

- Elemental species
- Separation distance
- Surround distance
- Erosion distance
- Minimum number of atoms per cluster

The effect of these parameters on the result of the cluster search is described in detail in Section 2.2.5.7. As elemental species Mo was chosen for all calculations performed, since it has the largest atomic fraction of all constituents segregating to the precipitates. Choosing appropriate values for the remaining parameters is less straightforward. In the corresponding literature it is suggested that the best value for d is determined by trial and error [40]. One requirement that has to be met is that very few clusters are found in a random solid solution with its composition being identical to the investigated alloy. This is important since only clusters that were formed due to thermodynamically facilitated decomposition should be identified as precipitates and clusters formed by random Mo-enrichment have to be excluded. In this thesis, the solution treated state was assumed to be a perfectly random solid solution. During the course of the investigations it became obvious, that precipitate volume fractions of up to 0.005 had to be tolerated in the solution annealed state in order to be able to identify clusters down to a sufficiently small size. The value used for the surround distance was chosen slightly larger than the separation distance in order to avoid obtaining clusters with small holes in them. Values for the erosion distance were chosen in such a way, that they were smaller than those for the surround distance, thereby creating a thin shell of solute atoms around the Mo clusters. After many trials and almost as many errors the parameter set agreed on for performing the intended analyses was determined as:

- Elemental species: Mo
- Separation distance: 0.48 nm
- Surround distance: 0.7 nm
- Erosion distance: 0.6 nm
- Minimum number of atoms per cluster: 20

After performing the cluster search, the results can be visualized in different ways. The mean concentration of all precipitates can be displayed in a table generated by PoSAP. Data in which the element contents and the radii of gyration of every single precipitate are displayed can be plotted in the Log-file of the PoSAP analysis. By using information contained in the Log-file, the volumes of the precipitates were calculated by multiplying the atoms present in the precipitates with their mean atomic volumes:

$$V = \sum_{i=1}^{n} N_i \cdot v_i \ . \qquad \text{[Eq. 24]}$$

N_i is the number of atoms of the species *i* present in the precipitates, v_i the specific atomic volume of species *i*. n represents the number of elements ranged in the mass spectrum. The volume fraction of the precipitates was determined by relating the precipitate volume to the analyzed volume. Information contained in the Log-file was retrieved by means of a macro written for the Microsoft Excel software package.

To obtain a measure of precipitate size, that can be compared with the results of the SANS analysis, the mean radius of gyration was calculated in three different ways. The two types mean radii introduced first are calculated based on the radii of gyration retrieved from the Log-file:

$$r_{g,m} = \frac{1}{n} \cdot \sum_{i=1}^{n} \left(\frac{r_{g,x,i} + r_{g,y,i} + r_{g,z,i}}{3} \right) \qquad \text{[Eq. 25]}$$

and

$$r_{g,v} = \frac{\sum_{i=1}^{n} \left(\frac{r_{g,x,i} + r_{g,y,i} + r_{g,z,i}}{3} \cdot v_i \right)}{\sum_{i=1}^{n} v_i}, \qquad \text{[Eq. 26]}$$

where $r_{g,x}$, $r_{g,y}$, $r_{g,z}$ are the radii of gyration in x-, y- and z-direction, respectively, v_i is the volume of the i^{th} precipitate and n is the number of precipitates in the analyzed volume. The difference of the two averaging methods is, that for calculating $r_{g,v}$ the precipitate volume is used as a weighting factor. These mean radii of gyration were then – under the bold assumption that the precipitates have spherical shape – converted into a physical particle radius by the following relation:

$$r_K = \sqrt{\frac{5}{3}} \cdot r_g \ , \qquad \text{[Eq. 27]}$$

where r_g is the radius of gyration and r_k the physical radius of the precipitate for the case that spherical precipitates are assumed.

The third mean precipitate radius was calculated by using a different approach. Since it is possible to calculate the volume of every precipitate found by the cluster search algorithm, an equivalent radius can be determined by assuming, that the precipitates are of spherical shape:

$$r_{eq,i} = \sqrt[3]{\frac{3 \cdot V_i}{4 \cdot \pi}}, \qquad \text{[Eq. 28]}$$

where V_i is the volume and $r_{eq,i}$ is the equivalent particle radius of precipitate *i*. Calculating a mean equivalent radius was performed by using the following equation:

$$r_{eq,v} = \frac{\sum_{i=1}^{n} r_{eq,i} \cdot V_i}{\sum_{i=1}^{n} V_i}. \qquad \text{[Eq. 29]}$$

For calculating $r_{eq,v}$ the particle volume is used as a weighting factor again.
Since the radius of gyration about all axes for every particle detected is contained in the Log-file, it was possible to investigate if there is a preferential direction in which the precipitates attain their largest extension. In addition to that, it was possible to calculate the chemical composition of every single precipitate detected.
The indication of the radii of gyration of all precipitates found in the dataset in the Log-file makes it possible to extract information on the precipitate shape that can be used in the SANS models. One parameter that has to be set for SANS analysis is the aspect ration of the ellipsoids used for describing the particle shape. To estimate the aspect ratio of the precipitates present in the material, the following relation was conceived:

$$\Delta r_g = \frac{1}{n} \sum_{i=1}^{n} \frac{\left| r_{M,i} - r_{x,i} \right| + \left| r_{M,i} - r_{y,i} \right| + \left| r_{M,i} - r_{z,i} \right|}{3}, \qquad \text{[Eq. 30]}$$

where $r_{x,i}$, $r_{y,i,}$ and $r_{z,i}$ are the radii of gyration in x-, y- and z-direction, correspondingly, while r_M is the mean radius of gyration of precipitate *i*:

$$r_{M,i} = \frac{r_{x,i} + r_{y,i} + r_{z,i}}{3}. \qquad \text{[Eq. 31]}$$

The aspect ratio of the ellipsoids is then given by

$$R = \frac{\left(1 + \frac{\Delta r_g}{r_M}\right)}{\left(1 - \frac{\Delta r_g}{r_M}\right)}, \qquad \text{[Eq. 32]}$$

where

$$\Delta r_M = \frac{1}{n} \cdot \sum_{i=1}^{n} \Delta r_{g,i} \ . \qquad \text{[Eq. 33]}$$

By these operations, the aspect ratio for an ellipsoid with rotational symmetry (i.e. with two axes that exhibit the same length) is determined. This calculation is by no means a very accurate procedure, but it was carried out nonetheless to find out if it is possible to improve the SANS data analysis by using the simple geometrical model available in SansFit to the highest extend possible.

3.5 Small angle neutron scattering (SANS)

The neutron scattering data used in this thesis have all been generated at the neutron source of the GKSS in Geesthacht, Germany. For creating the neutron flux, a research reactor with a thermal power of 5 MW is being used. SANS experiments were performed with cold neutrons at the SANS-2 beamline of GKSS by E. Eidenberger.

3.5.1 Sample preparation

Specimens were solution annealed and aged under the conditions mentioned in Section 3.1. After the thermal treatment, they were cut with an ATM brilliant 221 in discs of 5 mm in diameter and between 0.5 and 1 mm thickness. Cutting at low speed resulted in a surface roughness sufficiently low for performing neutron scattering experiments.

3.5.2 Beamline setup

Since a monochromatic beam is needed for performing the experiments, a velocity-selector type monochromator is used. With this monochromator, a neutron spectrum with a mean wavelength of 0.58 nm and a width of 10 % FWHM was obtained. After the monochromator, a vacuum tube that contains the collimation line is installed. In the collimation line, the divergency of the beam is adjusted by the insertion of cadmium apertures or so-called neutron guides. Proper collimation is necessary to reduce smearing of the scattering patterns. Increasing the collimation length improves the quality of the scattering patterns, but simultaneously decreases the neutron flux. Beam divergences down to 0.1° can be obtained at the SANS-2 beamline. For the experiments conducted, the collimation length was adjusted to the detector-sample distance to ensure a high neutron flux at an acceptable level of smearing.

The sample holder is located between the collimation line and the detector tube. At SANS-2 it is possible to install various apparatus such as furnaces or cryostats for providing different sample environments. For conducting the experiments a magnet that provides a magnetic field of up to 2 T and a sample stage that enables automatic changing of the specimens were installed. In front of the sample, a Cadmium aperture with a diameter of 3 mm was positioned, to ensure its proper illumination.
After penetrating the sample, the neutron beam enters the scattering tube. Like the collimation line, the scattering tube is evacuated to avoid air scattering. In the scattering tube, a 2D detector with a matrix of 256x256 pixels can be moved to attain sample-detector distances between 970 and 21690 mm in order to be able to cover a large q-range. In the center of the detector, a 50x50 mm^2 large beam-stop is used to absorb the primary beam. Sample-detector distances of 970 and 2970 mm were used to ensure a sufficient overlap of the q-ranges covered at each position.
Because the neutron flux of the reactor can vary considerable with time, a primary beam intensity monitor is installed at SANS-2. The information obtained by this instrument allows correcting variations in the scattered intensities due to variations in primary beam intensity.

3.5.3 Detector calibration

To be able to interpret the intensities observed at each detector position correctly, it is necessary to calibrate the detector. This is done by using materials that show very well defined incoherent scattering behaviour. The calibration factor is then determined by relating the measured to the calculated differential scattering cross section. For the calibration, Vanadium and PTFE samples were used. Vanadium shows relatively weak scattering behaviour and is known to have a differential scattering cross section of $2.92 \cdot 10^{-2}$ cm^{-1} [54]. It was employed for calibrating the detector for collimations used at sample detector distances of 970 mm. For collimations needed at large sample-detector distances, a PTFE sample was used, since it features large scattering cross sections. PTFE, however, does not provide an absolute measure like V, therefore, it had to be calibrated against the Vanadium-standard first. All calibrations were made at the same detector position to be able to compare the absolute intensities, only the collimation lengths were adjusted corresponding to the different sample-detector distances.
The background-correction of the data is performed by measuring the intensity of the scattered neutrons with an empty sample holder. Intensities detected in this configuration are the background for which the intensities obtained during the experiment have to be corrected. Furthermore, the intensity distribution on the detector has to be corrected for artefacts. Errors origin from the fact that pixels at small scattering angles correspond to larger elements of solid angle than pixels at large scattering angles. Artefacts also arise from the detection efficiency not being identical for every pixel of the detector. To be able to take these effects into account, a calibration measurement with PE, which shows extremely strong coherent

scattering, has to be made. From these measurements, a calibration file is produced, that is based on the deviation of the measured intensities from the mean intensity throughout the whole detector. This file is used for correcting the data obtained in the experiment.

3.5.4 Data processing

Calibration and merging of the scattered intensity curves recorded at different sample-detector positions is conducted with the aid of software tools developed by GKSS. The software SANDRA allows taking all calibration and sample parameters into account and calculates the differential scattering cross section $d\Sigma/d\Omega$ according to the following relation:

$$\frac{d\Sigma}{d\Omega}(q_i) = \frac{I_i}{M \cdot C \cdot d\Omega_i \cdot t \cdot T}, \qquad \text{[Eq. 34]}$$

where I_i is the intensity counted per pixel i, M is the primary beam monitor count rate, C is the calibration factor, t is the sample thickness, T is the sample transmission, and $d\Omega_i$ is the element of the solid angle assigned to pixel i. The next step to obtain a $d\Sigma/d\Omega$ scattering curve is to decide whether the scattered intensities are to be radially averaged over all azimuthal angles or if the intensities are to be averaged over certain sectors independently. Averaging over certain sectors is necessary if magnetic scattering by a sample that has been magnetized by an external field causes an asymmetric scattering pattern. An asymmetric scattering pattern of a magnetized ferromagnetic sample is shown in Figure 21.
In the direction parallel to the applied field, only nuclear scattering contributes to the size of the scattering vector while the size of the scattering vector perpendicular to the field vector is determined by the sum of nuclear and magnetic scattering. The data used in this thesis were obtained from sectors of 20° parallel and perpendicular to the magnetic field vector.
Fitting of the scattering curves is performed with the software tool SansFit which was written and provided by Peter Staron (GKSS).
For evaluating the precipitate population present in the investigated sample by SANS, a number of assumptions have to be made. In the case of this thesis, these assumptions were largely based on results obtained by atom probe microscopy. In the following, every single parameter and the value chosen for it will be discussed in detail in the order of appearance in the SansFit software (Fig. 22).

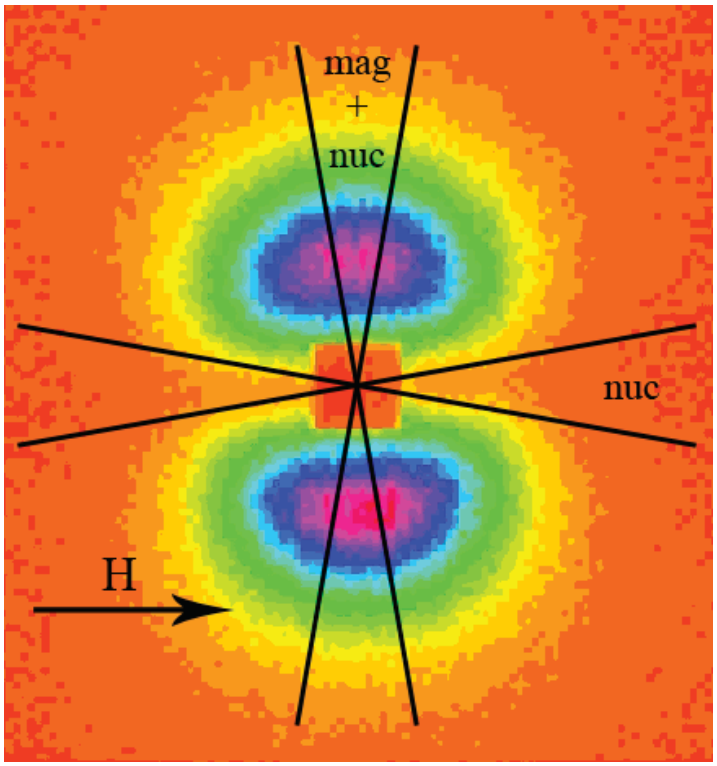

Fig. 21: SANS pattern for a magnetized ferromagnetic sample. The sample detector distance was 970 mm; the magnetic field vector H was oriented horizontally. (Courtesy of E. Eidenberger)

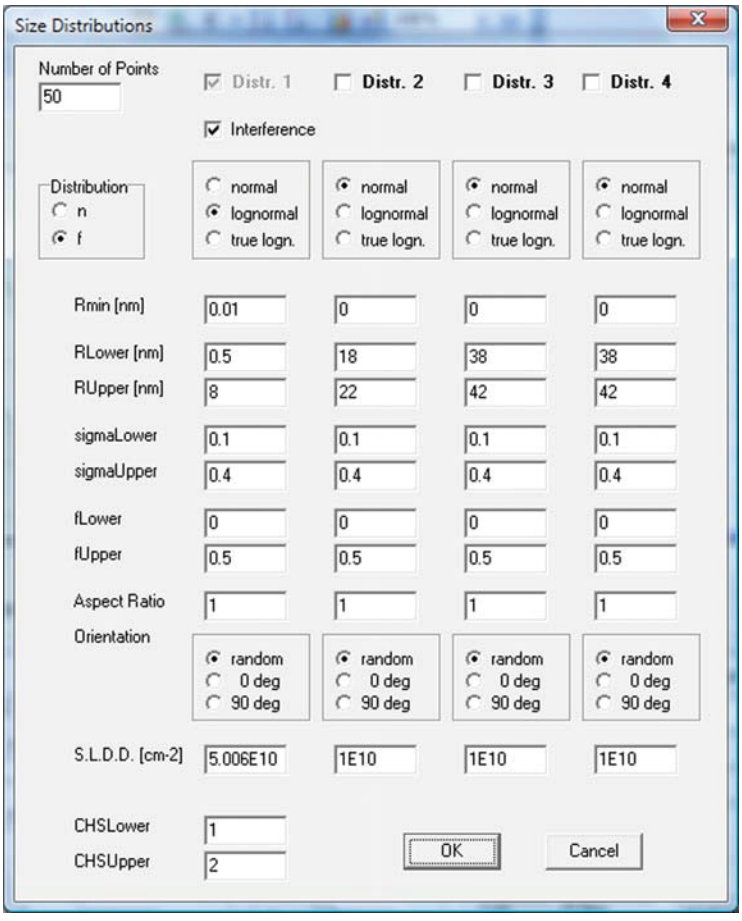

Fig. 22: Input window of the SansFit software. In this window all specifications concerning the size distribution are displayed.

Interference

This parameter is used to whether allow interparticle interference or not. If a relatively high volume fraction of particles is present, and the precipitate spacing is not much larger than the particle size, interparticle interference can occur. The decision if particle interference has to be considered was made dependent on the results of the AP analysis.

Size distribution type

Here, the mathematical distribution for describing the actual precipitate size distribution has to be selected. Particle size distributions frequently attain the shape of a lognormal distribution, nonetheless the decision which distribution to choose was based on results of the AP-analysis.

Fit parameters

The following parameters are used to ensure that the values of the fit parameters remain within certain boundaries. In the following, these parameters and typical values for them are given.

RLower/RUpper	Range in which the mean radius of the particle size distribution has to remain. (0.5/15)
sigmaLower/sigmaUpper	Range of the standard deviation of the particle distribution function. (0.1/0.4)
fLower/fUpper	Range of the particle volume fraction. (0/0.5)

Aspect ratio

Since the software assumes the particles to have elliptical shape, an aspect ratio has to be set. For quickly estimating the size and volume fraction of the precipitates, a spherical particle shape was assumed. In an attempt to improve the results, the atom probe data were evaluated with respect to precipitate shape.

Orientation

In SansFit a preferential orientation of the precipitates can be taken into account. Since no information was available on this micro-structural parameter, AP-analysis was used to determine if the precipitates exhibit a preferred orientation.

Scattering length density difference (SLDD)

The contrast in SANS-experiments results from the differences in scattering length density (SLD) between particles and matrix. This parameter is therefore crucial in analysing SANS data. Since the SANS pattern contains, in the case of a magnetic sample, a magnetic as well as a nuclear component, the scattering length density has to be determined for both cases. If magnetic scattering is used for analysis, the precipitates are assumed to have a magnetic SLD of zero, so the magnetic SLDD is identical to the magnetic SLD of the matrix. Calculating

this value is performed by using the scattering length density of the main constituent and taking all the influences of the alloying elements on its magnetic moment into account (Fig. 23).

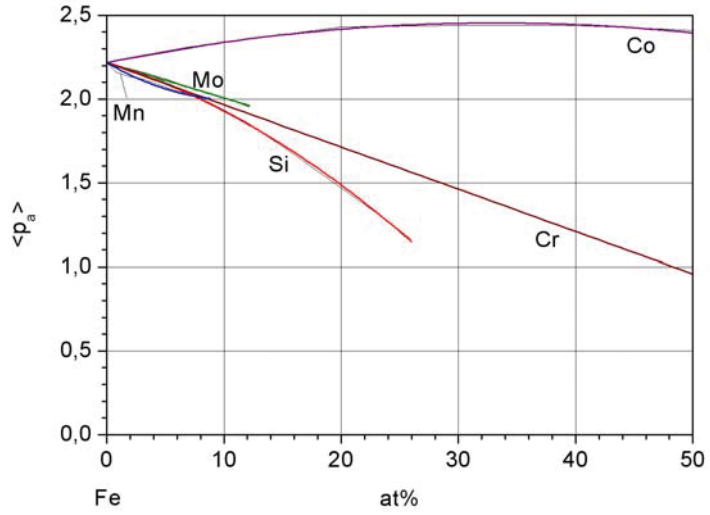

Fig. 23: Influence of alloying element concentration [at%] on the magnetic moment (p_a) of Fe [55, 56].

The magnetic scattering length density of the matrix is calculated from the chemical composition obtained by AP-analysis and the structural parameters of the matrix.
If the nuclear scattering pattern is analyzed, the precipitates contribute to the scattered intensity, which means that their scattering length density no longer equals zero. In this case the scattering length density of both, the matrix and the precipitates have to be calculated from the respective chemical composition.

4 Results and Discussion

4.1 Material

The material investigated was produced by powder-metallurgical processing and provided by Bohler Special Steel. Its chemical composition in the supplied condition was determined to the values shown in Table 2.

Tab. 2: Nominal composition of the investigated Fe-25 m% Co-15 m% Mo alloy [57].

	Fe	Co	Mo	Si	C
m%	Bal.	25.3	15.2	0.2	0.02
at%	Bal.	25.1	9.3	0.4	0.1

4.2 Hardness-tests

Hardness tests were conducted to relate the development of the mechanical properties to the observed micro-structural changes. The obtained hardness curve after ageing at 500 °C is shown in Figure 24. In Table 3 the hardness values are printed as numbers.

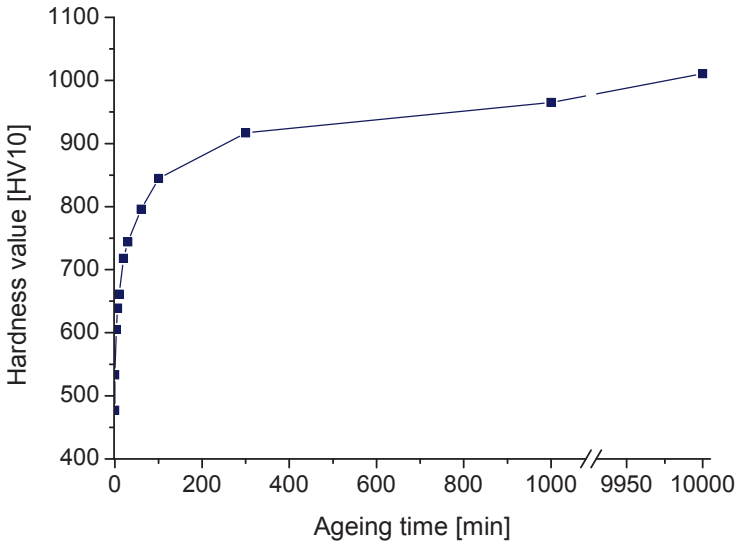

Fig. 24: Hardness vs. ageing time for the Fe-25 m% Co-15 m% Mo alloy. The lower value at t=0 min represents the solution annealed state, while the higher value represents the hardness after ageing for 0 min i.e. heating to the ageing temperature (500 °C) and immediate cooling.

Tab. 3: Hardness values for different ageing times at 500 °C.

Ageing Time [min]	Hardness value [HV10]
Solution annealed	477
0	533
3	605
6	639
10	661
20	718
30	744
60	796
100	845
300	918
1000	965
10000	1011

It is obvious, that the hardness increases continuously upon aging. While the hardness rises very fast at the beginning, it slows down during the course of the ageing treatment. However, there is no indication that the hardness maximum is reached at aging times of up to 10000 min. The reason for the hardness value at an ageing time of 0 min being larger than that of the solution annealed state lies in the finite heating and cooling rates of the ageing treatment performed. The 0 min sample was heated to the ageing temperature of 500 °C and immediately quenched. Despite the fact that the high heating and cooling rates were chosen, the hardness increase between the solution annealed specimen and the specimen aged for 0 min was determined to 66 HV10. This behaviour can be explained by the precipitation process being rather fast at the beginning and starting at temperatures below 500 °C [58].
In order to ensure that the hardness maximum does not lie between 1000 and 10000 min, additional heat treatments and hardness tests would be required.

4.3 Optical microscopy

After the heat treatments the microstructure of all specimens was examined by optical microscopy. All samples exhibited a martensitic matrix in which coarse secondary μ-phase particles were embedded. The distribution of this secondary intermetallic phase suggests that it is formed preferentially at austenite grain boundaries. An example of a representative microstructure is shown in Figure 25.
The martensite is recognizable by its characteristic lath structure, while the secondary precipitates image as bright spots. All specimens exhibited the same microstructure on a size scale accessible by optical microscopy.

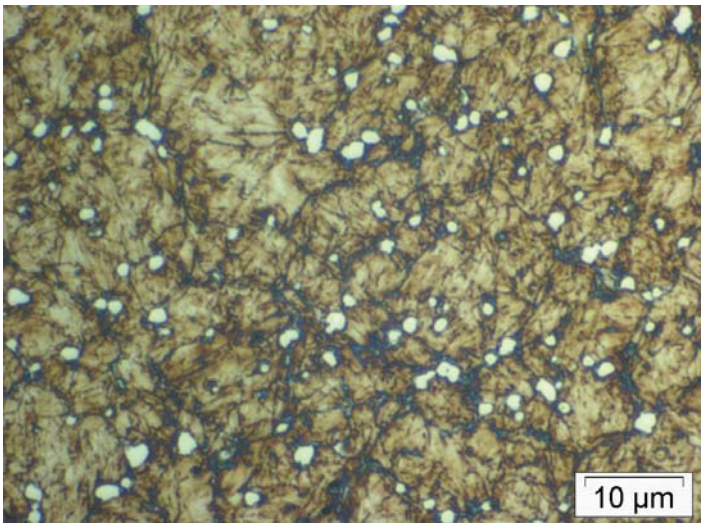

Fig. 25: Microstructure of the Fe-25 m% Co-15 m% Mo model alloy after solution annealing and ageing at 500 °C for 30 min. The coarse secondary µ-phase images brightly and is located primarily at the former austenite grain boundaries. The matrix is martensitic.

4.4 Atom probe tomography

Various analysis methods were applied to the data obtained by atom probe tomography. In the following, the results of each of these methods will be presented and the consequences of the results are discussed.

4.4.1 Homogeneity of the sample volumes

After reconstruction of the sample volumes, the first step was to evaluate the homogeneity of the element distribution within the reconstructed volume. In some cases, enrichment of elemental species such as C and P was observed, which points toward the presence of two-dimensional lattice defects. In Figure 26 such a defect is indicated by the presence of a planar zone to which C and P segregated and which was depleted in Co. Due to its two-dimensional character, it is speculated, that this defect is a martensite lath boundary.
The images in Figure 26 show the extent to which C and P have segregated to the defect as well as the depletion of Co. It is interesting to note, that the P atoms lie closer to the defect than the C atoms (Fig. 26a). If such microstructural features were present in the reconstructed volume, precipitate analysis in the regions affected by it is avoided, since the considerable differences between the density of the interface region and that of the surrounding matrix affect the results.

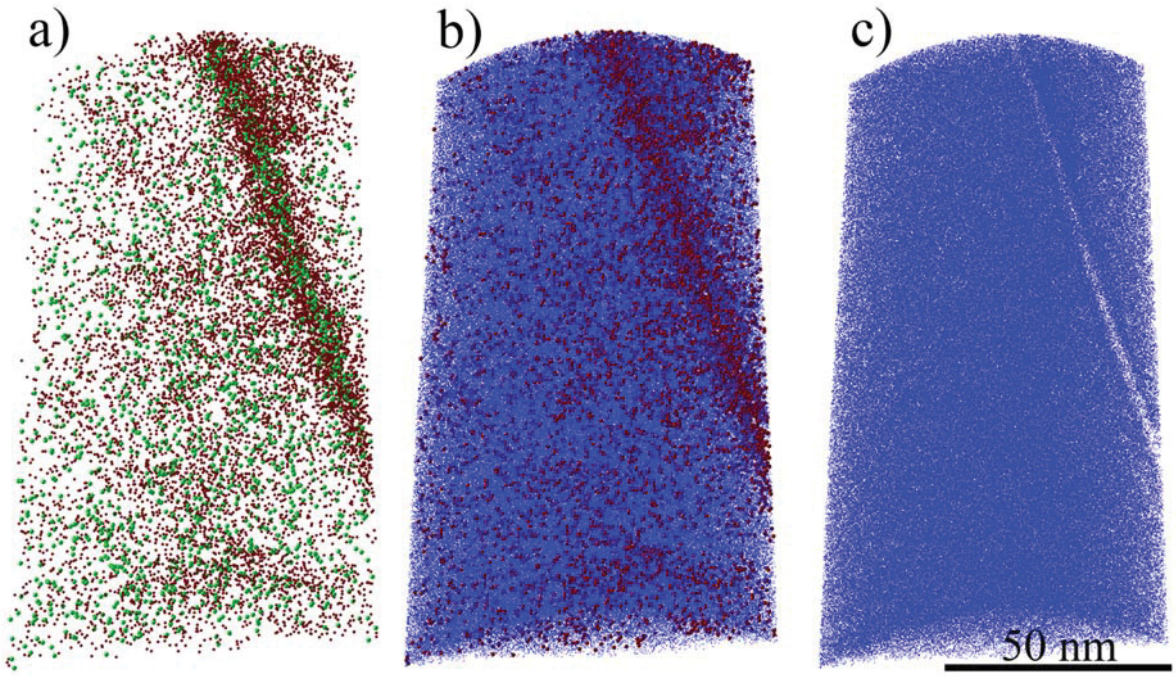

Fig. 26: Two-dimensional lattice defect in a reconstructed sample volume obtained from a Fe-25 m% Co-15 m% Mo specimen aged for 100 min at 500 °C. C atoms are indicated in brown, P is represented by green spheres and Co atoms are depicted in blue. .

4.4.2 Frequency distribution

All frequency distribution diagrams were calculated for Mo at a bin size of 50 atoms since this value is a fair compromise between being large enough for determining the composition on a sufficiently fine scale (2 %), but small enough for detecting extremely fine precipitates. If only random concentration fluctuations occur in the material, the frequency distribution curve coincides with a binomial distribution. Distributions that develop a pronounced tail towards higher concentration values indicate a local enrichment of the elemental species under consideration and denote decomposition of the matrix material (Fig. 27). While the binomial and the measured distribution coincide perfectly well for the solution annealed state (Fig. 27a), the sample that was held at 500°C for 0 min already shows a small deviation from the curve expected for a perfect random solid solution (Fig. 27b). With increasing ageing times, this deviation becomes more and more pronounced. The position of the maximum in the distribution curve is shifting towards lower solute concentrations while blocks with high solute concentrations occur more frequently (Fig. 27c-h).

From the data presented, it is concluded that decomposition continuously progresses during ageing. Furthermore, a very rapid decomposition process is indicated by the fact, that the frequency distributions of the solution annealed and 0 min sample deviate significantly.

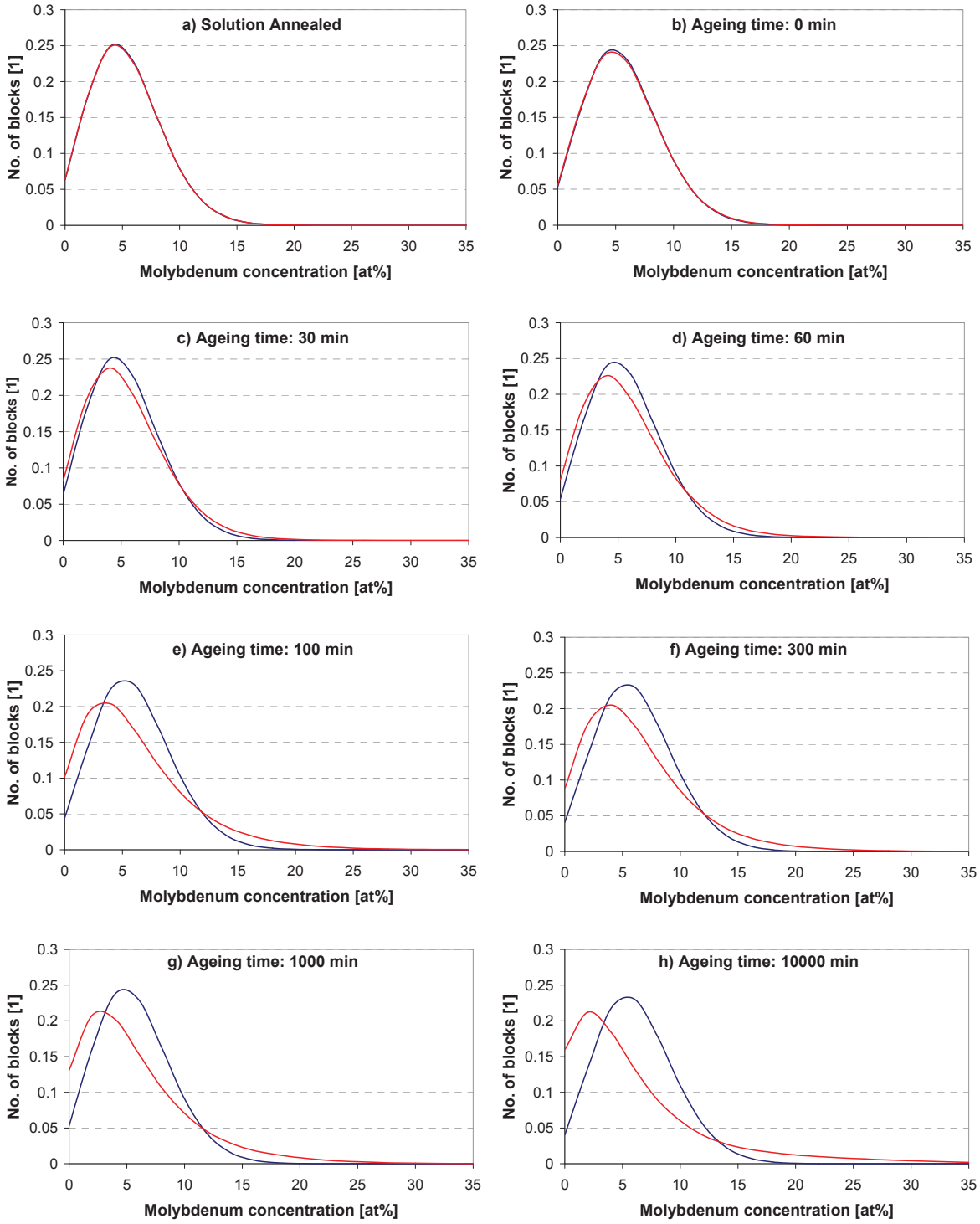

Fig. 27: Frequency distributions determined for specimens aged for different times at 500 °C. a) represents the frequency distributions for the solution annealed state and b)-h) those for specimens aged for 0, 30, 60, 100, 300, 1000 and 10000 min, respectively The frequency distribution of the sample is indicated in red while the blue curve represents a binomial distribution. With increasing ageing time an increasing degree of decomposition is evident by the development of a pronounced tail towards higher solute concentrations.

4.4.3 Isosurfaces and Proxigrams

For visualizing precipitates in the investigated volume, surfaces of constant molybdenum concentration have been used. The process of calculating a grid from which in turn the isosurface positions can be computed is described in Sections 2.2.5.2 and 2.2.5.6. Small grid delocalizations cause the isosurfaces to become rough and increase the statistical sampling noise, whereas large grid delocalizations average out small fluctuations in composition. Determining an appropriate grid delocalization was achieved by trial and error. Figure 28 shows Mo isosurfaces constructed for different grid delocalization values. It turned out, that for most investigations a grid delocalization of 3 nm offered a good compromise between high spatial resolution and low statistical sampling noise.

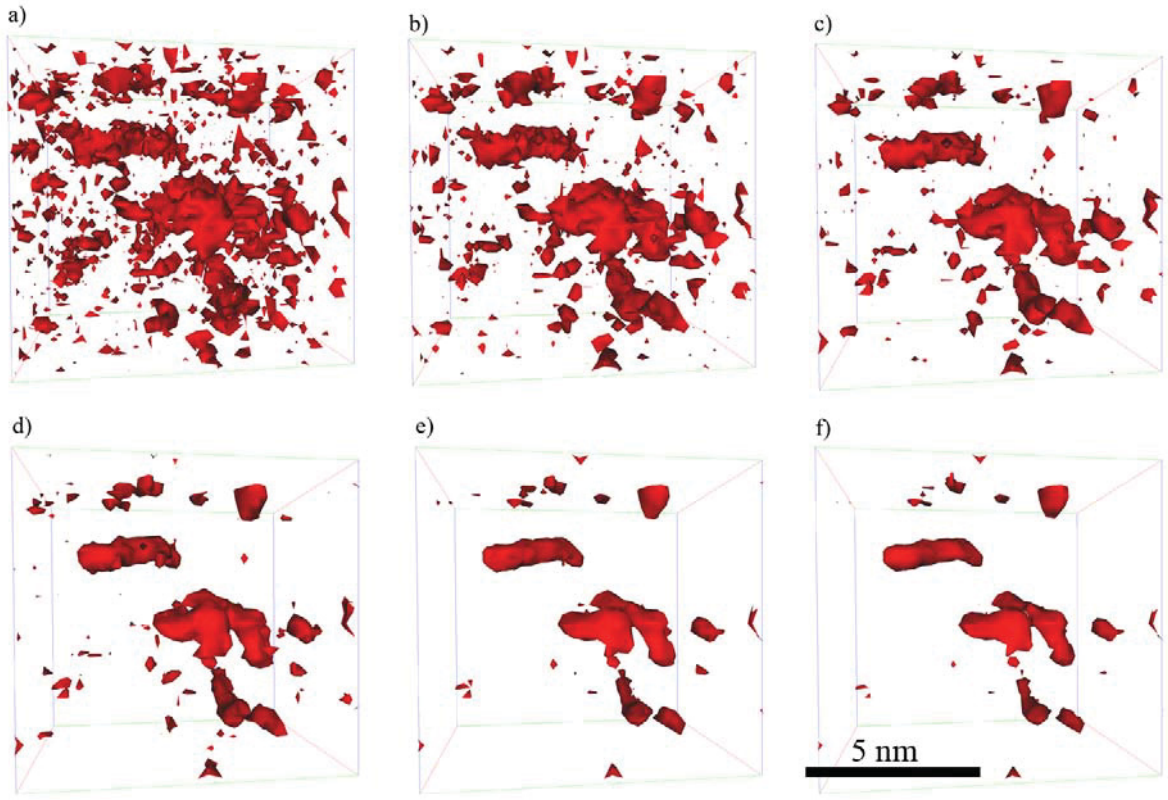

Fig. 28: Mo isosurfaces calculated for different grid delocalizations. Grid delocalizations of 1, 2, 2.5, 3, 3.5, and 4 nm were used for calculating the isosurfaces shown in a), b), c), d), e) and f) respectively. The isosurfaces become smoother with increasing delocalization and details are averaged out to an increasing extent. All isosurfaces were calculated for 20 % Mo content in a Fe-25 m% Co-15 m% Mo specimen aged at 500 °C for 300 min.

Attempts were made to characterize the morphology and size of the precipitates formed upon ageing by the use of isoconcentration surfaces. All atoms within an isosurface shell where exported into a new .POS-file, which enabled determining the overall composition and volume of these areas. Unfortunately, the IVAS software requires setting the parameter "minimum number of polygons" to a value that is high enough to prevent the computer from

stalling as already mentioned in Section 2.2.5.6. This is not only time consuming because this value has to be determined by trial and error, but also inconvenient since for some datasets it was required to set it to considerably large values. In some cases it was necessary to exclude isosurfaces that had less than 200 polygons, thereby neglecting precipitates of considerable size. Furthermore, it is not possible to determine the size of individual precipitates by using isosurfaces, only the volume of all precipitates together can be determined which would only allow calculating the mean precipitate size by making assumptions about their shape.
Another difficulty that has to be faced if isosurfaces are used for the characterization of precipitates is that the threshold concentration at which the surfaces are to be constructed has to be defined. For precipitates that exhibit a steep concentration gradient at the interface, this value influences the volume fraction of precipitates only slightly, however, for the investigated alloy, the dependence of precipitate volume fraction determined on a chosen threshold concentration is strongly pronounced. Figure 29 gives an impression of the dependence of precipitate volume fraction on the isosurface threshold value.

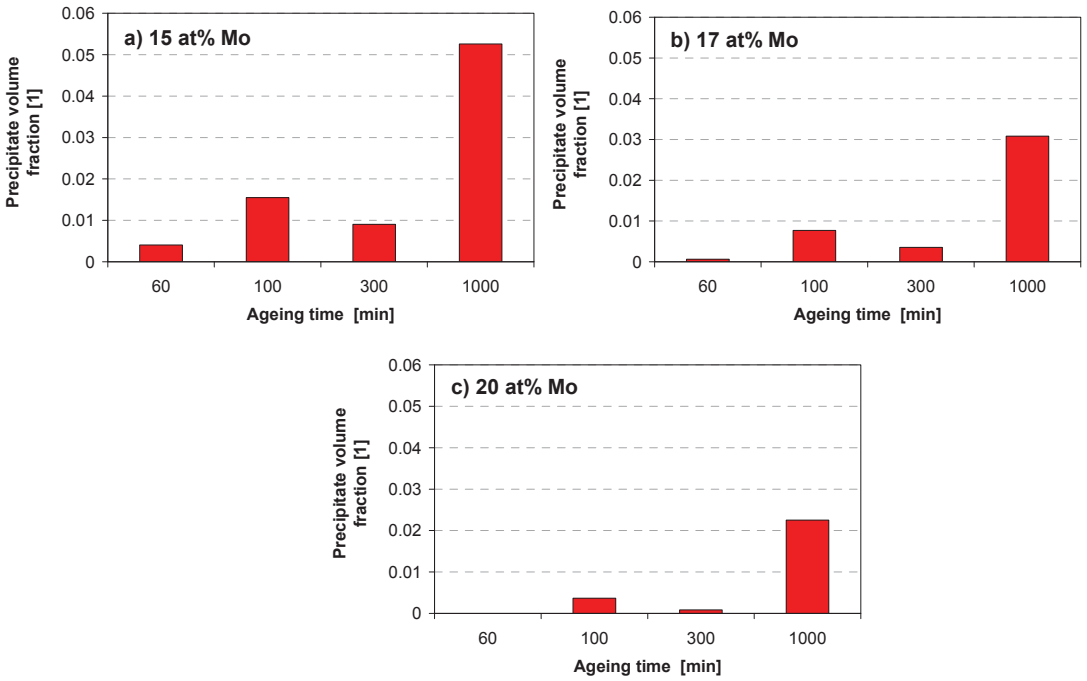

Fig. 29: Variation of the precipitate volume content using different threshold values for the construction of isosurfaces. The threshold value was set to (a) 15, (b) 17 and (c) 20 at% Mo.

The diagrams show that changing the isosurface threshold value affects not only the volume fraction of precipitates found in the analyzed volume, but also the ratios of precipitate volumes obtained for different ageing times. While for a threshold value of 17 at% the 1000 min sample exhibits a precipitate volume three times that of the 100 min sample (Fig. 29b), this ratio shifts to about seven if a threshold value of 15 at% is used (Fig. 29a). Although these facts preclude isosurfaces from the use as a tool for quantitative characterizations of the investigated materials nanostructure, isosurfaces were utilized for

getting a quick visual impression of the structures that were formed during ageing (Fig. 30). In addition, isodensity surfaces were used for monitoring the density gradients present in the datasets (Fig. 31). The density that is referred to in this work is the number of ranged atoms per unit volume.

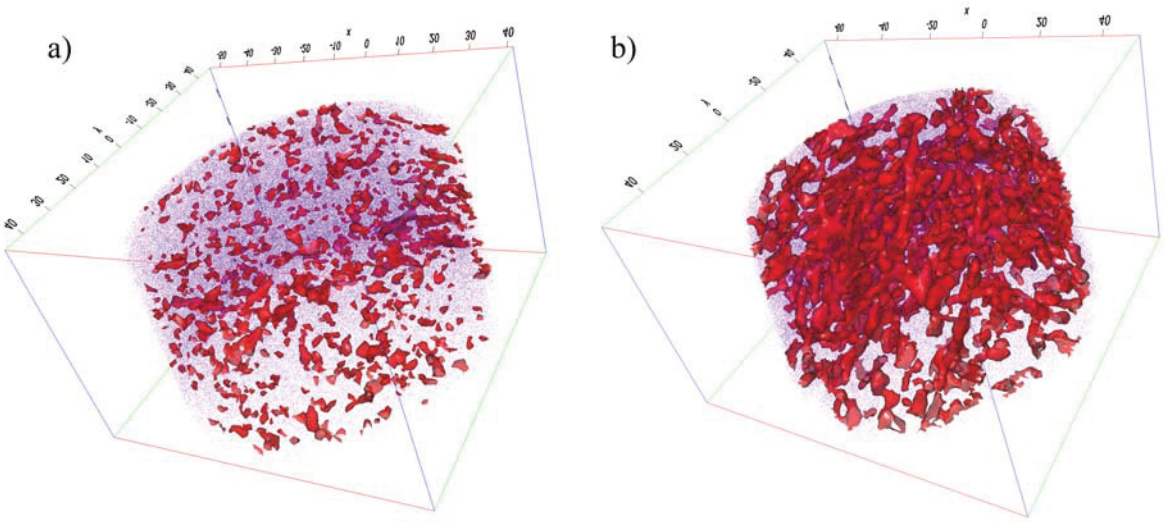

Fig. 30: Isosurfaces for different ageing times. a) was aged for 60 min b) was aged for 1000 min at 500 °C. Isosurfaces were calculated for 15 at% Molybdenum at a grid delocalization of 3 nm. It is obvious that both, the volume fraction and the size of the precipitates increase during ageing. The investigations were conducted on a Fe-25 m% Co-15 m% Mo alloy.

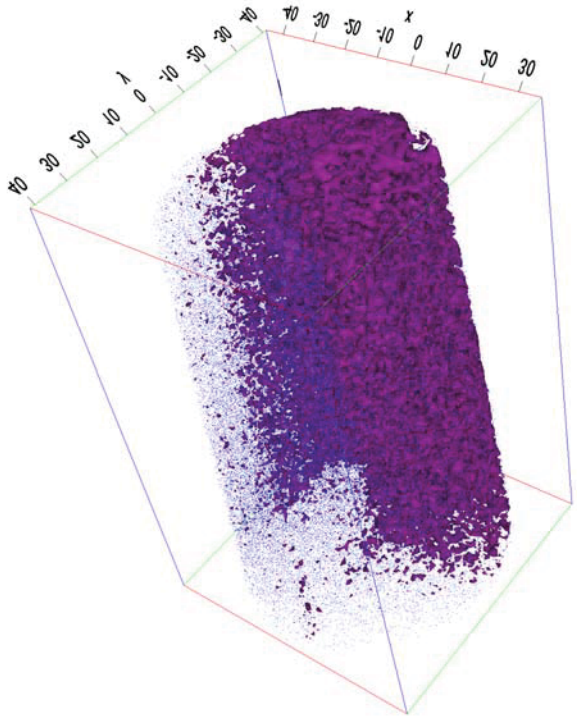

Fig. 31: Isodensity surfaces in a Fe-25 m% Co-15 m% Mo sample aged for 100 min at 500 °C.

Furthermore, proximity diagrams were calculated for isosurfaces of different threshold values. This was performed for investigating the characteristics of the interface of the precipitates present in the analyzed volume. Since the proxigrams calculated for 15 at%, 17 at% and 20 at% Mo isosurfaces are quite similar in shape, and due to the fact that the lowest threshold value offers superior statistics, it was decided to rely only on the proxigrams computed for the 15 at% isosurface. Figure 32 shows the development of the solute contents versus the distance to the isosurface.

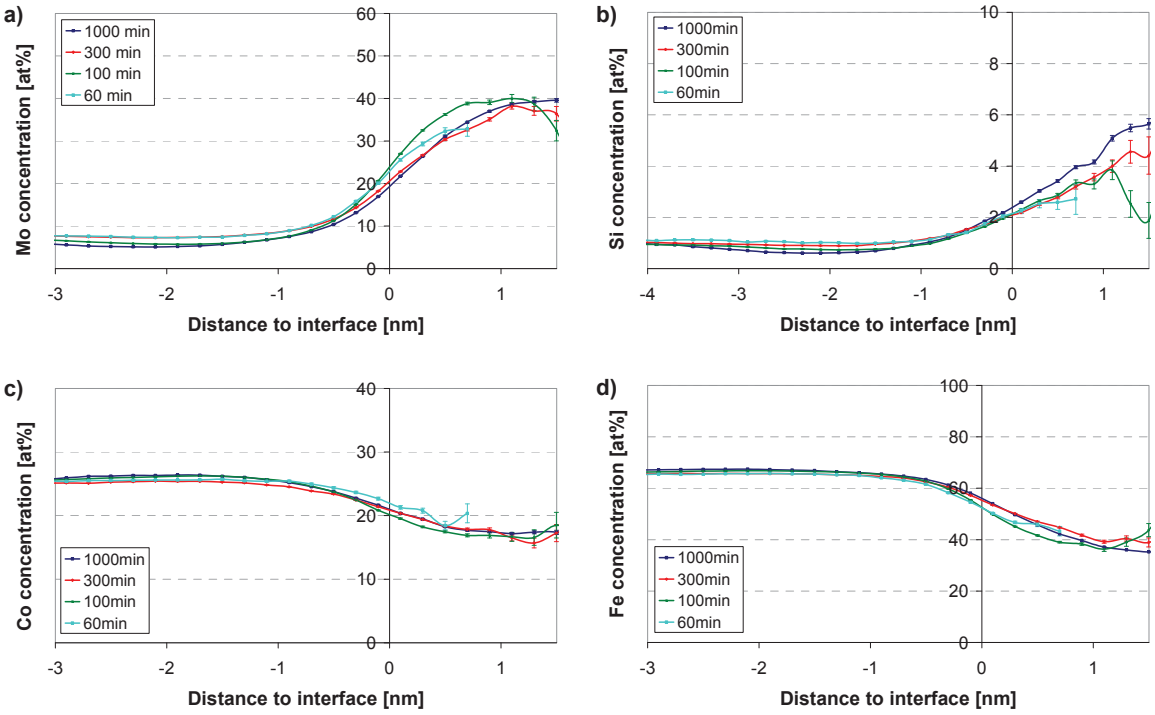

Fig. 32: Proximity diagrams for 15 % Mo isoconcentration surfaces. The bin size was set to 0.2 nm. Atoms at positive distances are part of the precipitates, those at negative distances belong to the matrix. It can clearly be seen, that the precipitates are enriched in (a) Mo and (b) Si and depleted in (c) Co and (d) Fe. The presence of an interface with relatively small concentration gradients is evident.

The proxigrams in Figures 32a-d show that the elements Mo and Si segregate to the precipitates which consequently show lower concentrations of Fe and Co than the matrix. Around the precipitates, a diffusion-zone is recognisable that is depleted of Mo and Si and enriched in Co and Fe. In Figure 33 it is shown, that Fe and Co are both replaced by Mo in the precipitates and that the ratio of Co to Fe remains fairly constant. With increasing ageing time, the diffusion zone becomes larger and more strongly pronounced. The concentration gradients at the precipitate interfaces seem not to be affected by ageing at 500 °C in the range between 60 and 1000 min. Proximity diagrams were not used to determine the composition at the core of the precipitates. Since a proxigram is computed for many isosurfaces enclosing precipitates of various sizes aliasing may occur for values that are not in the immediate vicinity of the isosurfaces.

The reason for the error bars to increase with increasing distances to the isosurface lies in the decreasing number of atoms that are present at such distances. A brief description of the algorithm for calculating proxigrams is given in Section 2.2.5.6, for details the reader is referred to [37].

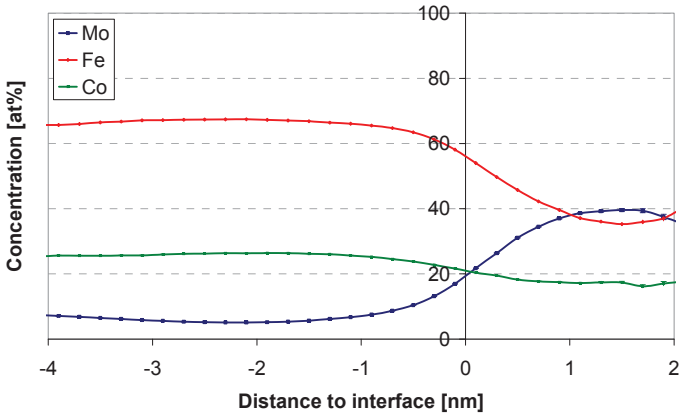

Fig. 33: Proximity diagram for 15 at% isosurfaces in a Fe-25 m% Co-15 m% Mo sample aged for 1000 min at 500 °C. The contents of Mo, Fe and Co are plotted versus the distance to the isosurface. Positive distances indicate a direction towards the core of the precipitate.

In some datasets, the proxigrams showed a Mo concentration profile that decreased, after reaching a maximum, to less than 15 at% Molybdenum (Fig. 34). Considering the structure of the algorithm, this should not be possible. A detailed investigation showed, that in some cases, polygons are missing in the isosurfaces that confine regions of high Mo concentration, explaining the peculiar shape of the proxigrams (Fig. 35). Atoms closest to the missing polygons are wrongly assigned to others and cause the proxigram to attain this erroneous form.

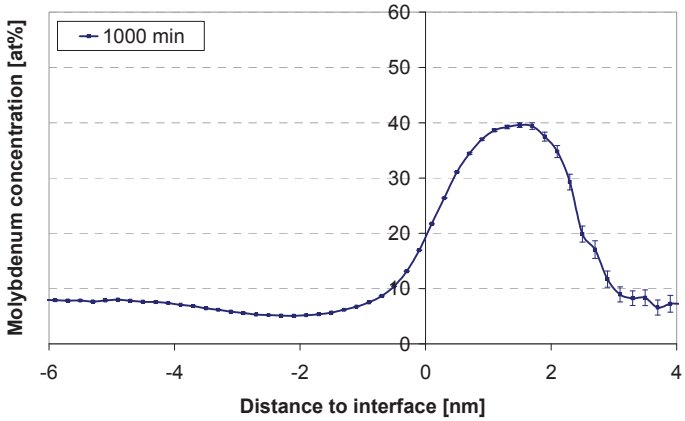

Fig. 34: Molybdenum concentrations in the vicinity of 15% Mo isosurfaces after ageing for 1000 min at 500 °C. The proxigram shows a pronounced maximum and decreases with increasing distance to the interface to values lower than the threshold concentration used for constructing the isosurfaces. At a positive distance of 2.5 nm to the interface the Molybdenum concentration falls below 15 at%. Since positive distances indicate directions from the interface towards the precipitates core this behaviour is highly unexpected.

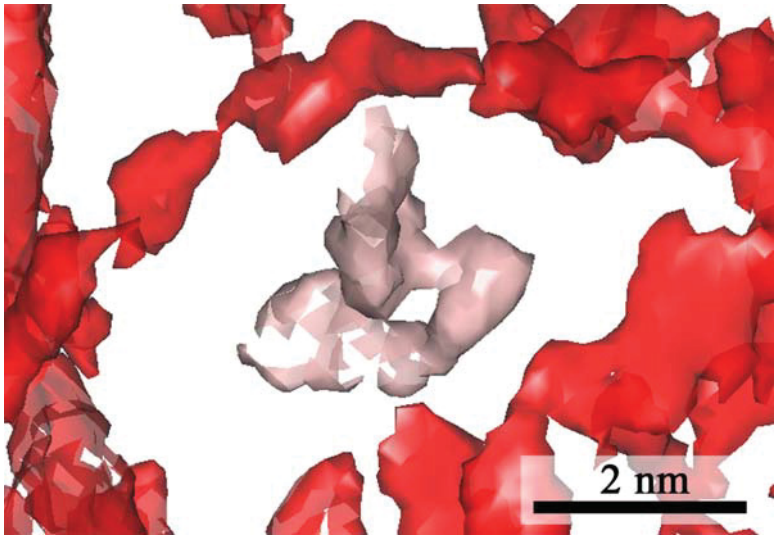

Fig. 35: Here an example for missing polygons in an isosurface is given. The pink isosurface does not properly confine the precipitate and causes the proxigram algorithm to wrongly assign atoms to other polygons.

4.4.4 Fourier transformation and autocorrelation function

To analyze the atom probe data with respect to a dominating wavelength in the concentration distribution, a Mathematica routine was written that calculates the power spectrum of one-dimensional concentration profiles. The power spectrum of a matrix is the product of the Fourier transformed with the inverse Fourier transformed of the matrix. Mathematica supplies a function that allows calculating the power spectrum of a matrix by using the so called discrete Fourier transformation. In order to be able to use the discrete Fourier transformation scheme, the spacing of the matrix elements has to be constant. If one- or two-dimensional concentration profiles are calculated in IVAS, this distance between neighbouring matrix elements corresponds to the chosen bin size. In the Mathematica routine written by the author of this thesis, the concentration profile is read in and brought to such a form, that Mathematica can calculate the power spectrum of these data. If a dominating wavelength is present, a pronounced peak should occur in the power spectrum, whose position in inverse space corresponds to the dominating wavelength in real space. The relation between the peak position in inverse space (q) and the corresponding wavelength (λ) is given in Section 2.2.5.3, Equation 6. In Figure 36a-e the power spectra of concentration profiles after 0, 100, 300, 1000 and 10000 min are shown.

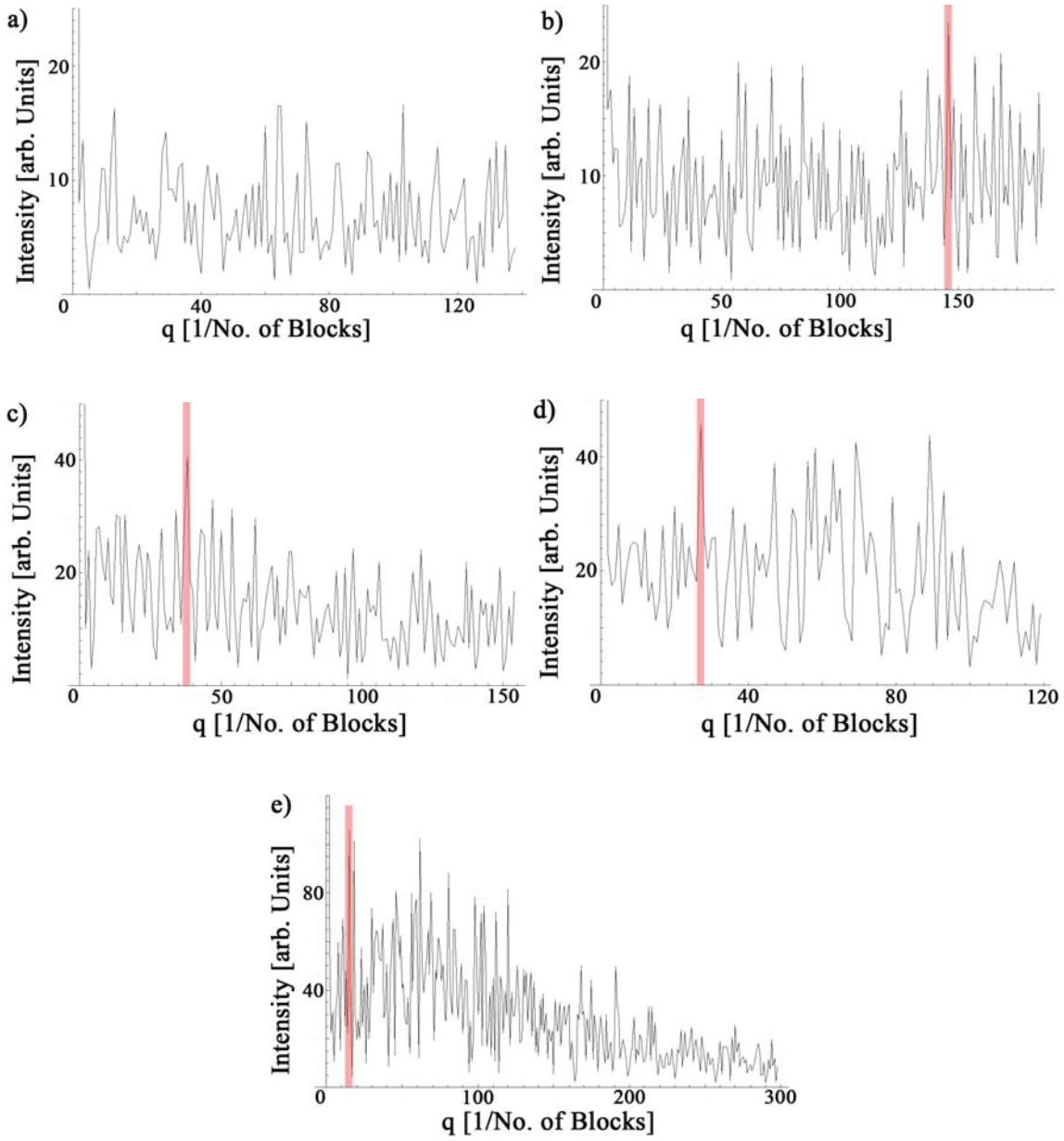

Fig. 36: The power spectra after ageing for 0, 100, 300, 1000, and 10000 min are referred to as (a), (b), (c), (d), and (e), respectively. In the dataset shown in (a), no dominant wavelength could be determined. After 100 min (b) a wavelength of 1.02 nm can be evaluated. Ageing for 300 min (c), 1000 min (d) and 10000 min (e) gives corresponding wavelengths of 3.26, 4.32, and 15.89 nm.

The identification of a dominant peak is not straightforward. Nonetheless, an attempt was made by assuming that the concentration fluctuations have wavelengths larger than 0.8 nm, which corresponds to the largest q value shown on the abscissa of the diagrams.

It can be seen that in none of the spectra one peak is by orders of magnitude larger than the others, but in all spectra, except in that obtained after 0 min ageing time, one dominant peak can be determined (Fig. 36). Furthermore, it can be seen that the position of the largest peak is shifting towards smaller q values with increasing ageing time, indicating an increase in wavelength of the concentration fluctuations. In addition to that, the intensities the peaks

attain are increasing upon ageing. The power spectra might give a hint concerning the scale on which decomposition occurs, yet the data are not reliable enough to allow drawing sound conclusions.

Applying the autocorrelation algorithm implemented in PoSAP to the datasets yielded the results shown in Figure 37.

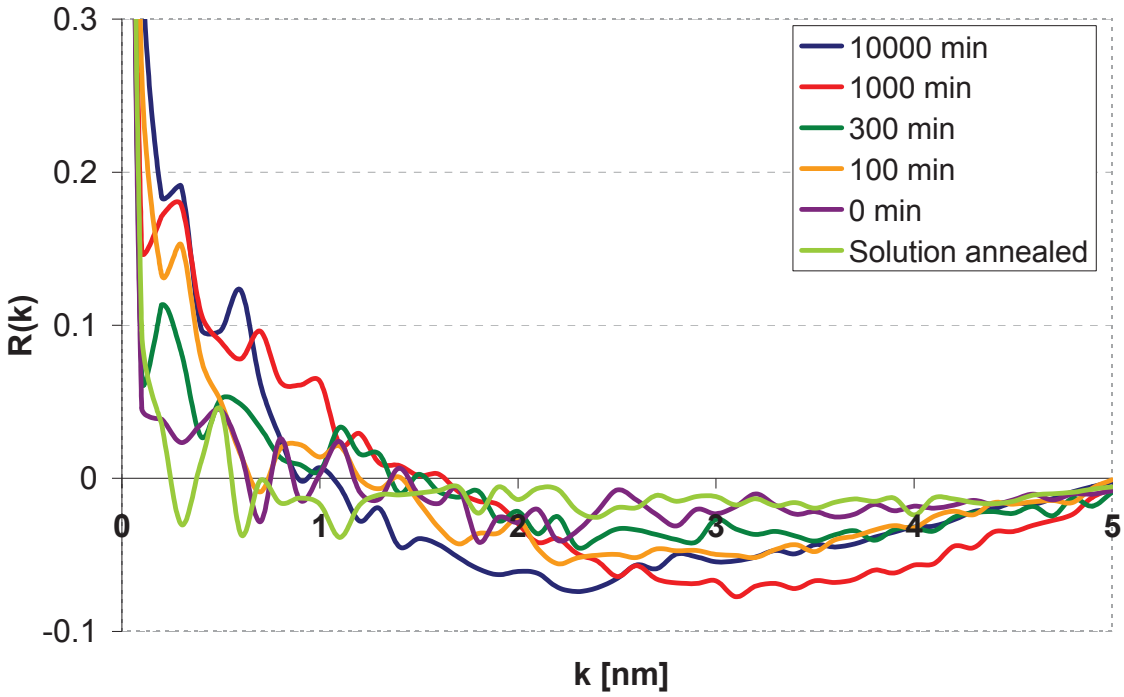

Fig. 37: Autocorrelation functions calculated by the algorithm implemented in PoSAP. In these curves, the position of the first minimum corresponds to the mean particle diameter R(k) is the autocorrelation coefficient and k is referred to as lag and has the dimension of a length (see 2.2.5.4).

The position of the first minimum in the autocorrelation curve indicates the particles size. Particle sizes derived from the curves shown in Figure 37 do not follow a recognizable trend. It is, therefore, concluded, that no information on the precipitation behaviour of the model alloy can be retrieved from the autocorrelation curves shown.

4.4.5 Cluster search algorithm

4.4.5.1 Parameter determination

The cluster search algorithm implemented in PoSAP allows the user to choose a set of input parameters for carrying out the search. Determining these parameters is according to [40], usually achieved by trial and error. Validating the chosen parameters was performed by comparing the results of the cluster search to predetermined boundary conditions.

The volume fraction of precipitates found in the solution annealed state should not exceed 0.5 vol% and the morphology of the precipitates should be similar to the precipitates that can

be identified by transmission electron microscopy (TEM) and to those identified by isosurfaces. An image obtained by TEM is shown in Figure 38.

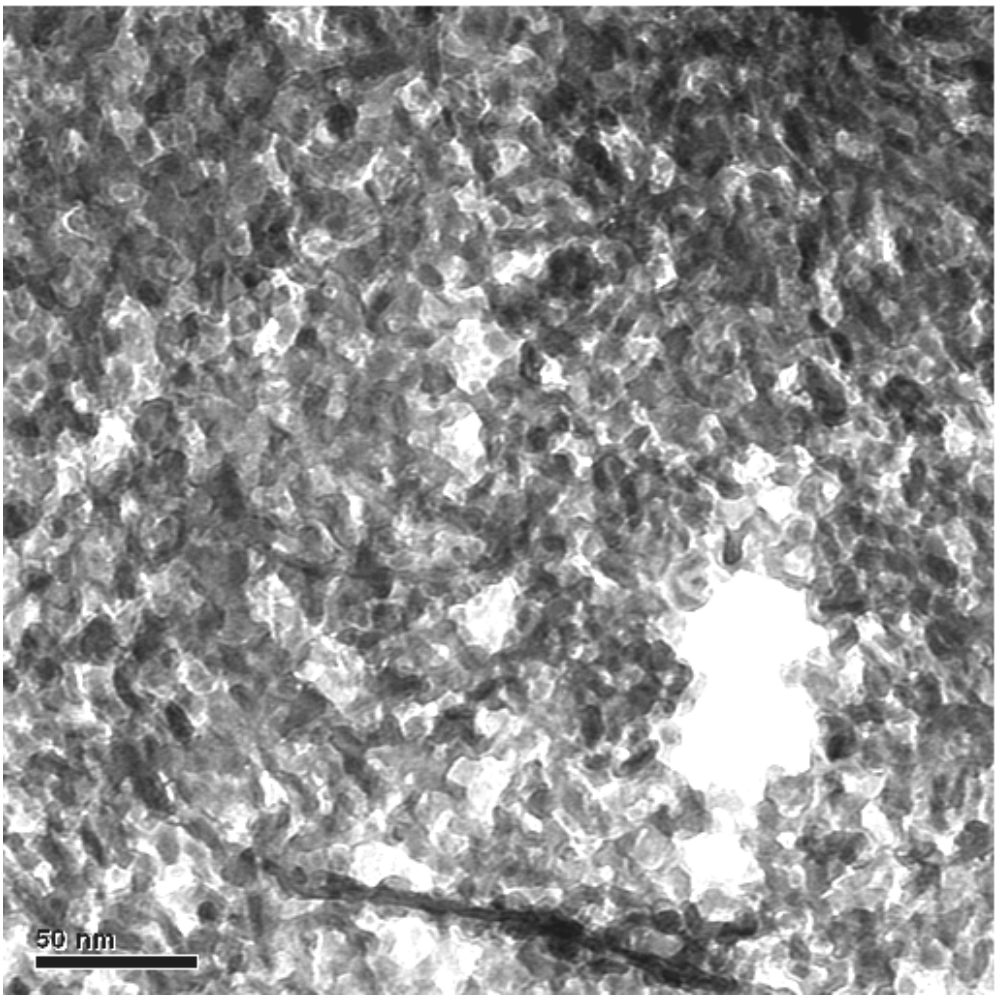

Fig. 38: TEM brightfield micrograph of a Fe-25 m% Co-15 m% Mo specimen aged for 10000 min at 500 °C. The image was obtained with a Phillips CM12 equipped with a Si (Li) ED-detector from EDAX. Mo rich precipitates image darkly and appear to form an interconnected structure (courtesy of E. Eidenberger).

Mo has a high density and a high atomic mass, therefore regions of high Mo concentration image darkly. Concentration variations on the scale of a few nanometres are visible. In addition to that the morphology of the composition variations suggests that a complex, interconnected structure is present. The following images show the same sample volume, one time analyzed by means of isosurfaces (Fig. 39), one time by using the cluster search algorithm (Fig. 40).

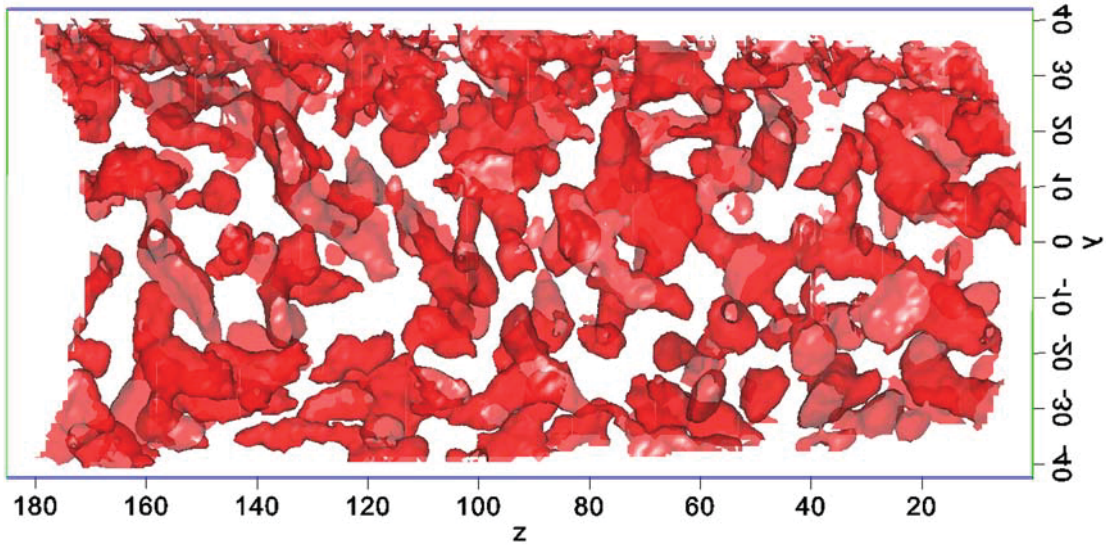

Fig. 39: 15 at% Mo isosurfaces in a Fe-25 m% Co-15 m% Mo sample after ageing for 10000 minutes at 500 °C. The slice shown is 15 nm thick, dimensions are indicated in nm.

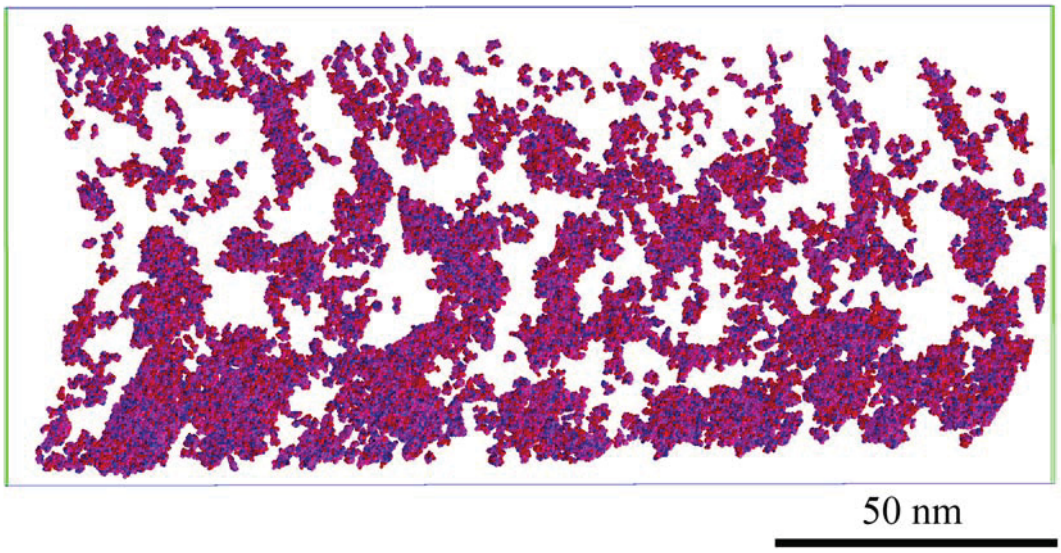

Fig. 40: Precipitates found by the cluster search algorithm for a separation distance=0.48 nm, surrounds distance=0.7 nm and erosion distance=0.6 nm. The Fe-25 m% Co-15 m% Mo specimen was aged for 10000 min at 500 °C. Fe atoms are depicted in pink, Mo atoms in red and Co atoms in blue.

In Figure 39 a 15 at% Molybdenum isosurface is shown in a 15 nm thick slice of the dataset acquired from a Fe-25 m% Co-15 m% Mo specimen aged for 10000 min at 500 °C. For the construction of the isosurfaces a grid delocalization of 3 nm was used, isosurfaces with less than 200 polygons could not be imaged in order to avoid an “out of bounds” exception. Figure 40 shows the result of the cluster search performed in the same sample volume for which the isosurfaces of Figure 39 were calculated. The parameters used for performing the cluster search are given in Section 3.4.5.4.

By comparing Figure 39 and Figure 40 it can be seen that for all major clusters in Figure 39 a corresponding cluster in Figure 40 can be found. Due to the large grid delocalization

necessary, the isosurface structures are much coarser than the structures identified as precipitates by the cluster search algorithm. In both images, the clusters have complex shapes and form an interconnected structure.

Comparing the TEM and the atom probe images is complicated because of the limited spatial resolution of the TEM image (Fig. 38). Nonetheless, in both images a complex interconnected microstructure is recognizable. With decreasing resolution, small features of the microstructure are no longer visible. The ability to image small precipitates is best if the cluster search is used and worst in the TEM, consequently, the structures observed in TEM appear to be coarser than those found with the cluster search algorithm or isosurfaces.

4.4.5.2 Density dependence of the cluster search results

The cluster search algorithm exhibits one major problem. Since the clusters are identified by neighbouring Mo atoms being closer than specified by a threshold value, the results of the algorithm are not independent of the datasets density. The higher the density of a dataset, the higher the volume fraction of precipitates found by the cluster search algorithm. This is inconvenient since datasets gained from different atom probe measurements exhibit different densities even if the experiments are performed under the same conditions. There are also considerable differences in the local densities within one single dataset. Usually, the datasets exhibit higher densities in those regions where the laser illuminated the sample, thereby increasing the number of precipitates found in this region (Fig. 41).

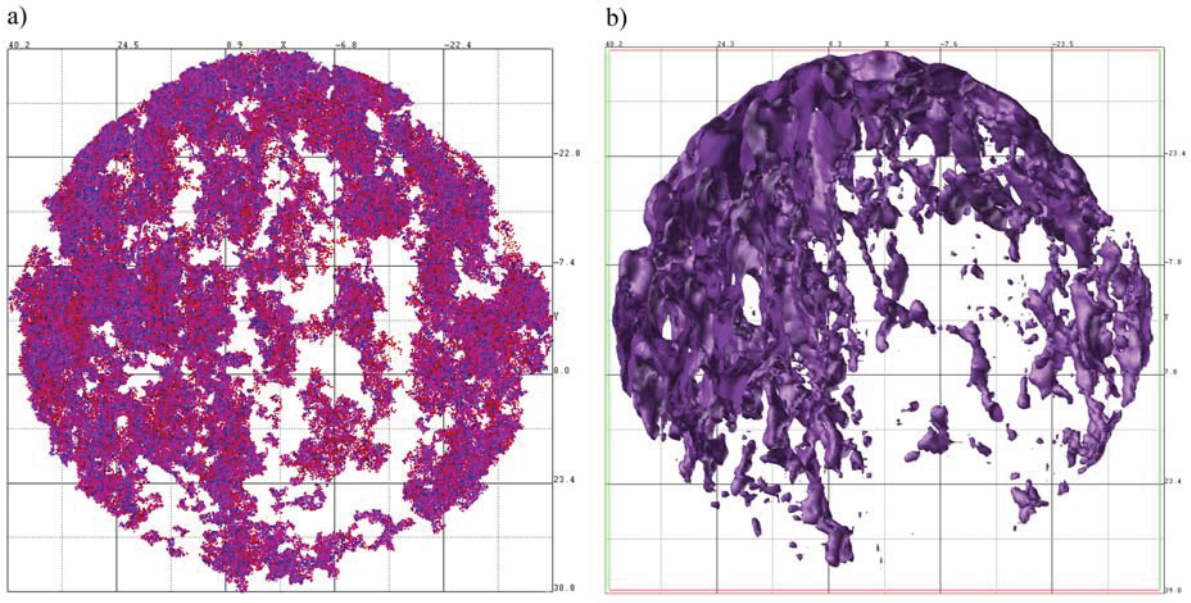

Fig. 41: Comparison between precipitates found (a) and dataset density (b). Both pictures show the same volume of a Fe-25 m% Co-15 m% Mo sample aged for 10000 min at 500 °C.

The problem had to be overcome to ensure the consistency of the results of the cluster search algorithm when applied to different datasets, or to different volume elements of one dataset. The idea behind the correction introduced is to vary the parameters of the cluster search in

such a way, that its results are similar for two datasets that are identical except for their density. Since the distance between Mo atoms is dependent on the density, the parameter "separation distance" was chosen to be adapted. The following relation was established for adapting a separation distance d for a dataset of density ρ

$$d = \sqrt[3]{\frac{\rho_0 \cdot d_0}{\rho}}, \qquad \text{[Eq. 35]}$$

where ρ_0 is the density of the dataset in which the separation distance d_0 was used for performing the cluster search.

This relationship was validated by creating two datasets that are identical except for their density. This was achieved by defining varying numbers of peaks in the mass spectrum during reconstruction, which leads to a different volume calculated for the reconstructed sample and causes the two datasets to have different densities if the same range file is used for opening the .POS-file. First a cluster search was performed on those two datasets without adapting the separation distance to the different densities. The precipitate volume fractions obtained for the datasets differed by a factor of two. After performing the cluster search with the corrected search parameters, the difference in the precipitate volume fractions decreased dramatically (Fig. 42). Small differences between the precipitate volume fractions of the high and low density dataset can be ascribed to the limited possibility of adjusting the separation distance. PoSAP allows entering the separation distance with 0.01 nm accuracy. Experiments have shown that changing of the separation distance by this value might lead to changes in precipitate volume fraction of up to 50 % of the original value. Therefore, the value of the volume fraction of precipitates was determined by linear interpolation between the two closest values that can be selected for the separation distance in PoSAP.

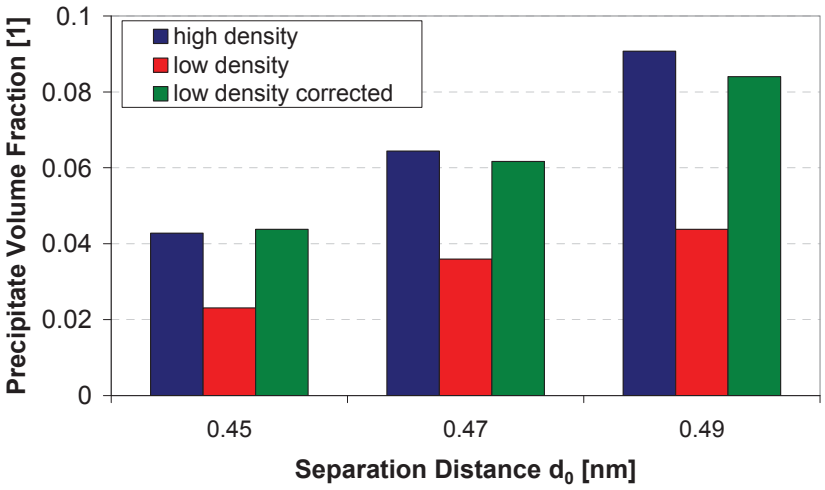

Fig. 42: Comparison of datasets that have different densities but are identical otherwise. The data for high density and low density were obtained with the search parameter d_0; low density corrected was obtained after adapting the search parameter to the lower density of the dataset.

Adapting of the separation distance to the average density of a dataset solves the problem of dealing with datasets that do not exhibit the same densities. However, the complications caused by different densities within one dataset persist.

To minimize the influence of density gradients and to ensure the comparability of the data, cuboids were cut out of the reconstructed dataset, their density was calculated and correspondingly adapted. By performing the cluster search only for a limited part of the entire dataset, density variations within the analyzed volume are kept low. In addition to that, the location of the volume to be analyzed within the dataset was determined by the aid of isodensity surfaces. The cuboids were placed in regions with low density gradients which were frequently found at the core of the reconstructed sample volumes (Fig. 43).

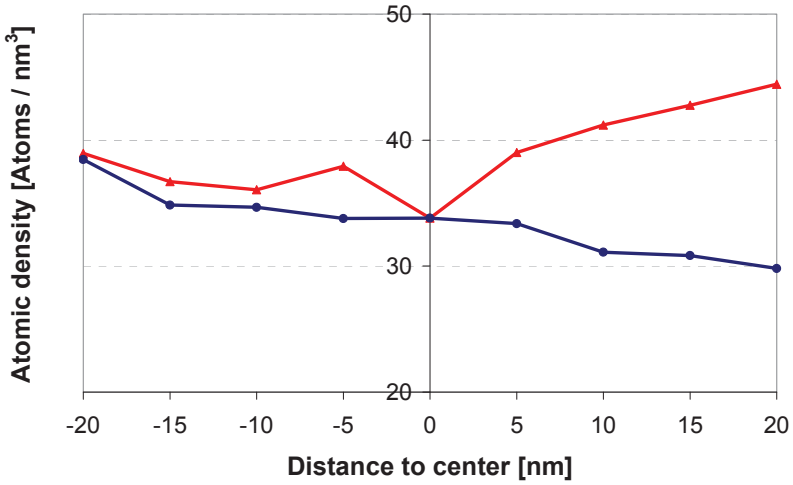

Fig. 43: Density variations in a reconstructed sample volume. The red curve represents the density distribution along the x-axis; the blue curve indicates density along the y-axis.

To determine the extend of the density variations, rods with a cross-section of 5x5 nm^2 were created at different positions in the reconstructed volume and analyzed with respect to their atomic density.

It was found that variations in density occur mainly in x and y direction but not in z-direction. Therefore, the cuboids in which cluster searches were performed usually extended over the entire length of the reconstructed specimen and were constricted in their extensions in x and y direction.

To ensure that the mean concentration is not dependent on the position within the analyzed volume, the same procedure with which the density distribution was determined was carried out with respect to the concentrations of the main constituents (Fig. 44). This uneven distribution of alloying elements within the matrix is most likely to be an artefact of the laser pulse induced field evaporation of atoms. An attempt of correcting the varying Mo content was made by using the density of Mo atoms instead of the atomic density for adapting the separation distance. Using the Mo density might lead to an overcompensation of the separation distance if a large cluster is present in the analyzed volume which would yield

erroneous results. For this reason the Mo density compensation was not used for adapting cluster search parameters.

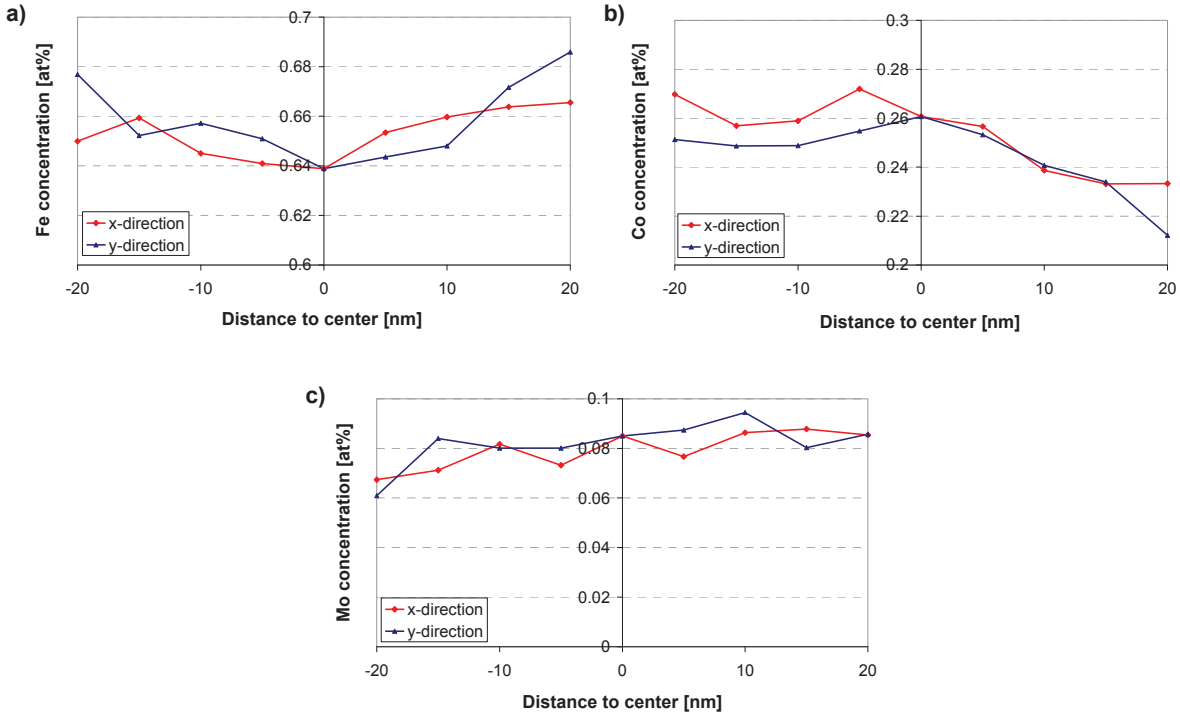

Fig. 44: (a) Fe, (b) Co and (c) Mo concentration variations within the reconstructed sample volume are shown. The data were obtained from positioning rods with a 5x5 nm^2 cross section within the reconstructed sample volume of a specimen aged for 10000 min at 500 °C.

4.4.5.3 Size characterization

Since the precipitates found by the cluster algorithm exhibit complex morphologies, choosing an appropriate measure is a crucial step in determining the precipitate size. The morphologies of the precipitates found in the model alloy evolve with ageing time from clearly distinguishable precipitates with nearly elliptical shapes into highly interconnected structures that attain morphologies that resemble organic structures such as corals for instance (Fig. 45). Both software packages for analyzing 3D-AP data that were accessible during the course of this thesis, PoSAP and IVAS, offer limited options for the analysis of precipitate sizes. PoSAP provides the radii of gyration for every precipitate found with the cluster search algorithm, IVAS allows selecting spheres, ellipsoids or cylinders for describing the precipitate shape and varies the axes lengths of the shape chosen to fit the precipitate shape. Unfortunately, even at short ageing times the attempt to describe precipitates with the shapes provided by IVAS yielded unsatisfying results. At longer ageing times, the precipitates obtain shapes that cannot be described by means of simple geometrical models (Fig. 46).

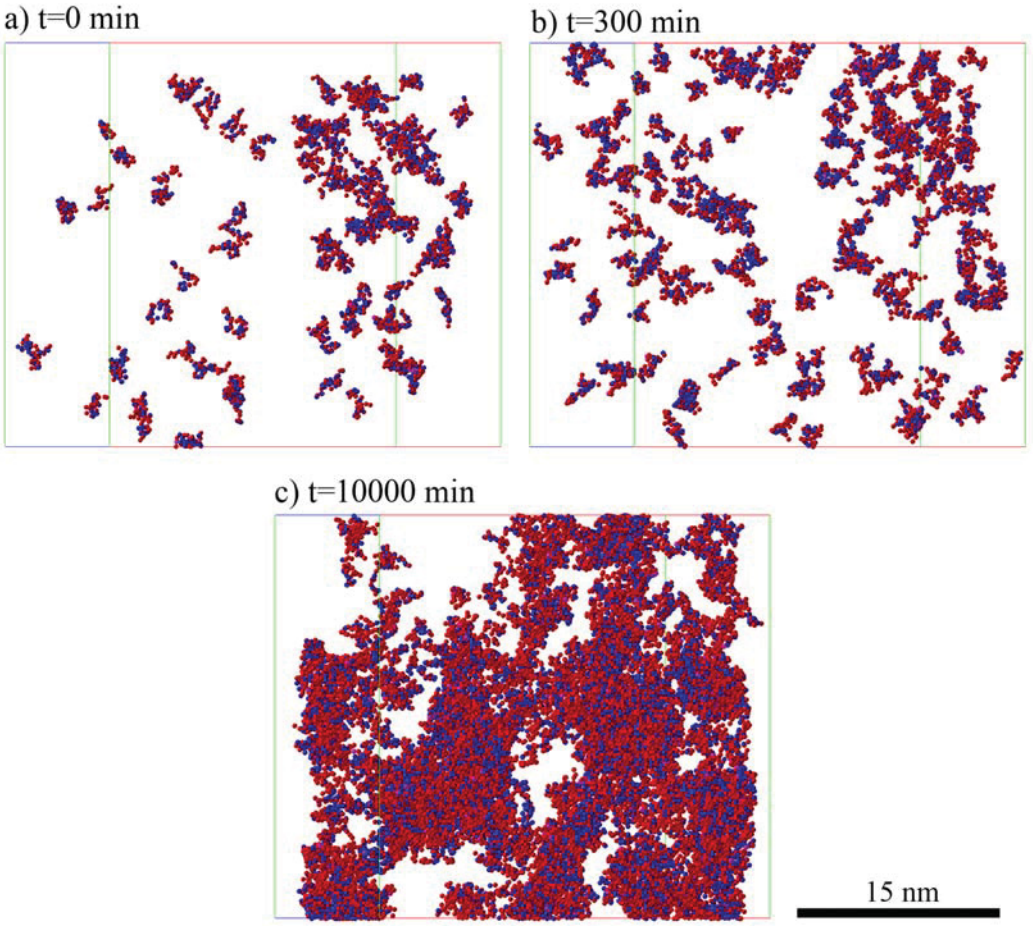

Fig. 45: Development of the precipitate morphology with increasing ageing time at a temperature of 500 °C. At short ageing times the precipitates have elliptic shapes while for long ageing times they form a highly interconnected structure. The cubes shown have edge-lengths of 30 nm. The images were obtained after ageing for 0 (a), 300 (b) and 10000 min (c), respectively.

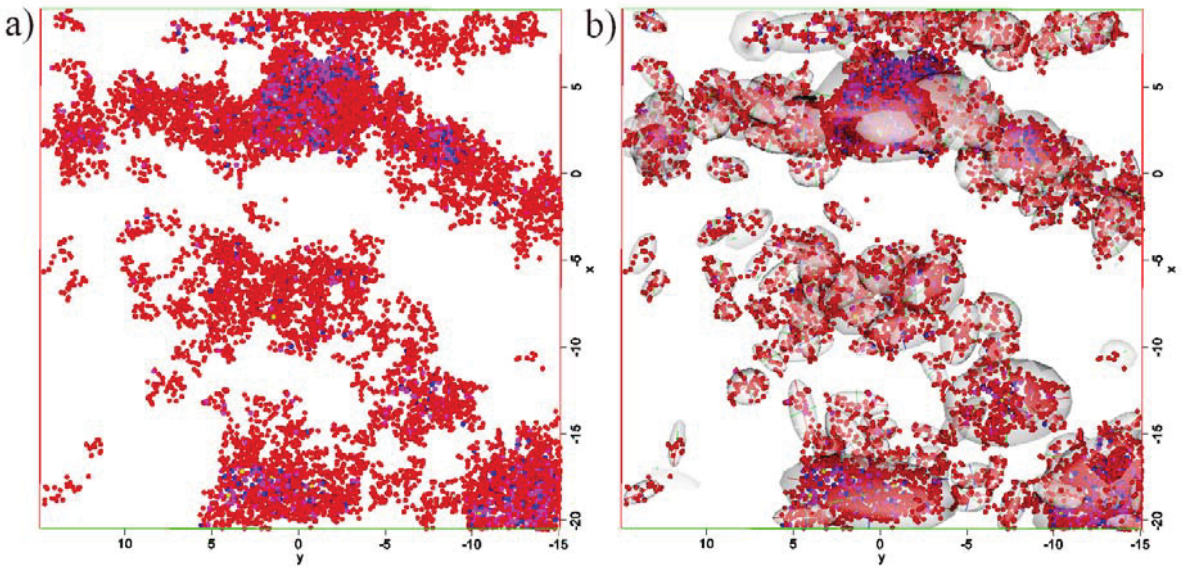

Fig. 46: In a) the precipitates are only visible through the corresponding atoms, while in b) the individual precipitates are enclosed by elliptical shells. Due to the complex shape of the precipitates, only shells in the form of ellipsoids are able to describe the precipitate morphology properly.

In Figure 46a the precipitates are represented by the atoms they consist of, while in Figure 46b the precipitates are enclosed by an elliptical shell constructed by IVAS. It is obvious that the ellipsoids do not properly reproduce the precipitate shape.

Due to the lack of a suitable method to describe the size of precipitates, it was decided to use the volume of the precipitates as an indicator for their size. Alternatively, the radius of a sphere that has the same volume as the precipitate was used. The equivalent radius has the advantage of giving a better impression of the actual size than the volume does simply because one is used to interpreting size in terms of distances instead of volumes. After the cluster search algorithm has been applied to a dataset, the results can be written to the PoSAP Log-file. In the Log-file the data are organized in such a way that for every precipitate found the number of atoms of one elemental species is recorded. An example for a typical Log-file entry is given in Figure 47.

Number of particles detected: 347

Particle	Ion	No. ions	Mean Position			Radius of Gyration		
			x	y	z	x	y	z
1	All	113	-8.3295	11.2296	-14.5590	0.5352	1.1799	0.2372
1	Fe	42	-8.1648	11.1310	-14.5419	0.5320	1.0627	0.2290
1	Mo	53	-8.4390	11.3169	-14.5651	0.5267	1.2206	0.2419
1	Co	16	-8.4400	11.2385	-14.5496	0.4669	1.2593	0.2334
1	Cu	1	-7.7770	12.4211	-14.7313	0.0000	0.0000	0.0000
1	Si	1	-8.2242	9.4150	-14.9276	0.0000	0.0000	0.0000
2	All	126	16.6579	-20.7869	-14.3825	0.4334	0.3881	0.4120
2	Fe	76	16.6820	-20.8116	-14.3892	0.4008	0.3844	0.4176
2	Mo	29	16.6294	-20.8242	-14.3188	0.5291	0.4250	0.4315
2	Co	21	16.6096	-20.6462	-14.4463	0.3915	0.3090	0.3470
3	All	72	7.2914	5.0368	-14.6142	0.5240	0.4126	0.2502
3	Fe	34	7.1739	5.0934	-14.6212	0.4910	0.4089	0.2488
3	Mo	22	7.2736	5.0569	-14.5696	0.5257	0.4620	0.2696
3	Co	16	7.5657	4.8887	-14.6605	0.4880	0.2970	0.2124
4	All	130	-28.9684	5.1250	-14.4076	0.6265	0.6560	0.3502
4	Fe	57	-29.0423	5.0277	-14.4644	0.6169	0.6435	0.3791
4	Mo	46	-28.9697	5.2664	-14.3465	0.6439	0.6223	0.3383
4	Cr	1	-29.2902	5.9534	-14.0685	0.0000	0.0000	0.0000
4	Co	20	-28.8414	4.9643	-14.4087	0.5542	0.6961	0.2840
4	Si	6	-28.6271	5.3629	-14.3886	0.6701	0.5528	0.2583

Fig. 47: Excerpt from a PoSAP Log-file in which the results of the cluster search were written. The mean positions and radii of gyration for every elemental species present in the precipitate as well as for the entire precipitate are contained.

The information contained in the Log-file allows calculating the precipitate volume by using the values for the atomic volumes utilized for reconstructing the analyzed sample volume by IVAS. Information on the morphology of the precipitates can be derived from the precipitates' radii of gyration.

Log-files are not organized in a format that allows retrieving the contained information easily. For performing analyzes with respect to volume and composition of the precipitates a macro had to be written in order to be able to access the information required. The source code can be found in Appendix I. In the files generated by the macros, the precipitates are divided into different size ranges of which the mean compositions and radii of gyration are

calculated. Figure 48 shows the development of precipitate size distribution as a function of ageing time. Diagrams in which the size distribution of every heat treatment state is shown in a single diagram can be found in Appendix II.

On the abscissa of the diagram shown in Figure 48 the equivalent radius of the precipitates is plotted, while the ordinate represents the relative frequency of the precipitates within one size range. During ageing times between 0 and 30 min at 500 °C, the height of the most prominent peak decreases and the distribution acquires a tail towards larger equivalent particle radii. It is at an ageing time of 60 min that precipitates are observed to start coalescing and forming particles larger than 3 nm.

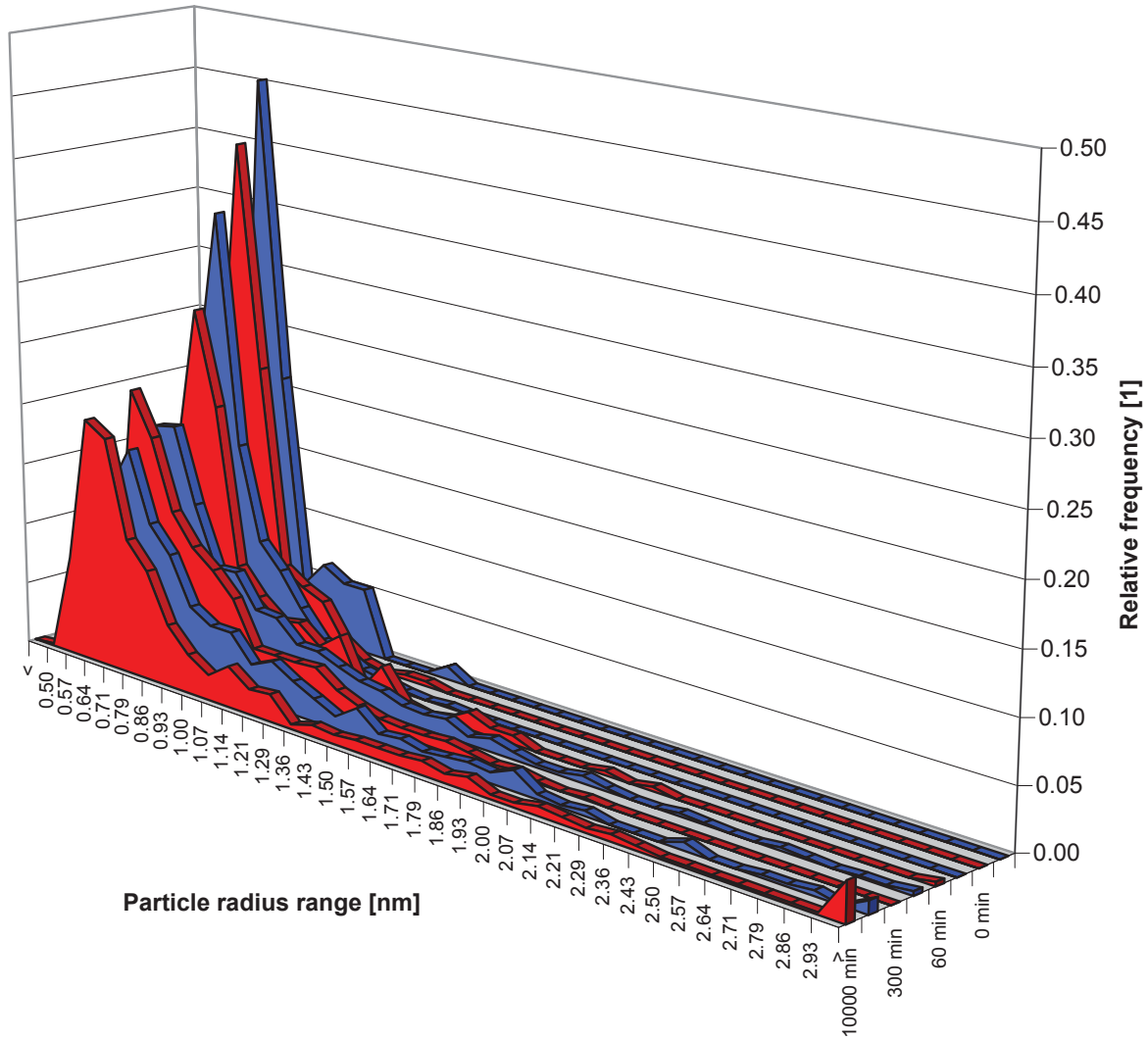

Fig. 48: Development of the precipitate size distribution Fe-25 m% Co-15 m% Mo upon ageing. With increasing ageing time at 500 °C, the size distribution shows a tail towards larger precipitates. However, a large number of precipitates with radii of about 0.7 nm are present in all datasets. For detecting the precipitates the cluster search algorithm was used. The data are also presented in the form of conventional diagrams in Appendix II.

The height of the peak at roughly 0.7 nm is decreasing until it reaches a relative frequency of roughly 0.2. At ageing times larger than 100 min this value remains constant. In the dataset obtained from a sample aged for 300 min the most interesting feature is the lack of precipitates with equivalent radii larger than 2.3 nm. After ageing for 1000 min at 500 °C, the material seems to have reached a state in which only the number of precipitates with radii larger than 2 nm increases.

The results of the cluster search algorithm show clearly that the precipitate size increases towards longer ageing times. Nevertheless, in all datasets investigated a large number of precipitates with equivalent radii around 0.7 nm are observed. As ageing progresses the relative frequency of particles of that size decreases, although the position of the most prominent peak in the frequency distribution diagram always remains at 0.7 nm. One question arising from the development of the precipitate size distribution is whether the particles with equivalent radii of around 0.7 nm are the result of an ageing process or just random Mo clusters that were identified as precipitates due to inappropriate cluster search parameters. To answer this question, the cluster search would have to be performed for a dataset that exhibits a perfectly random solid solution with a composition equal to that of the model alloy. Due to the lack of possibilities to simulate such a random solid solution this calibration step was not performed.

For ensuring a good readability it was chosen to limit the equivalent radii shown in the diagrams to 3 nm to ensure the comparability of the different graphs. The particle population with radii larger than 3 nm does not form a peak in the frequency distribution diagram, but populates a large range of size classes. This behaviour is illustrated in Figure 49 in which the size range shown includes equivalent radii of up to 10 nm. In this diagram is little more information presented compared to the size distributions shown in Figure 48 and Appendix II, yet the readability has diminished.

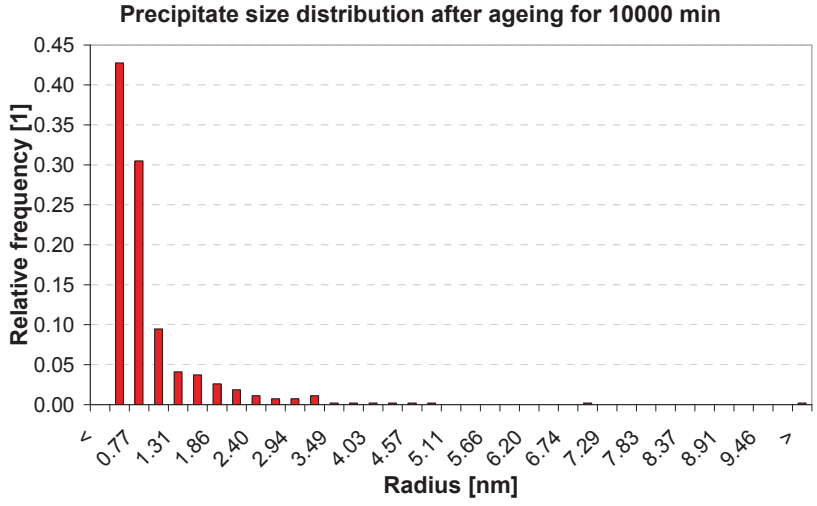

Fig. 49: Precipitate size distribution in Fe-25 m% Co-15 m% Mo for a larger range of equivalent radii.

In order to complement the information given above and to determine the contribution of the different size ranges to the precipitate volume, the fraction of precipitate volume was plotted against the precipitate size range in Figure 50.

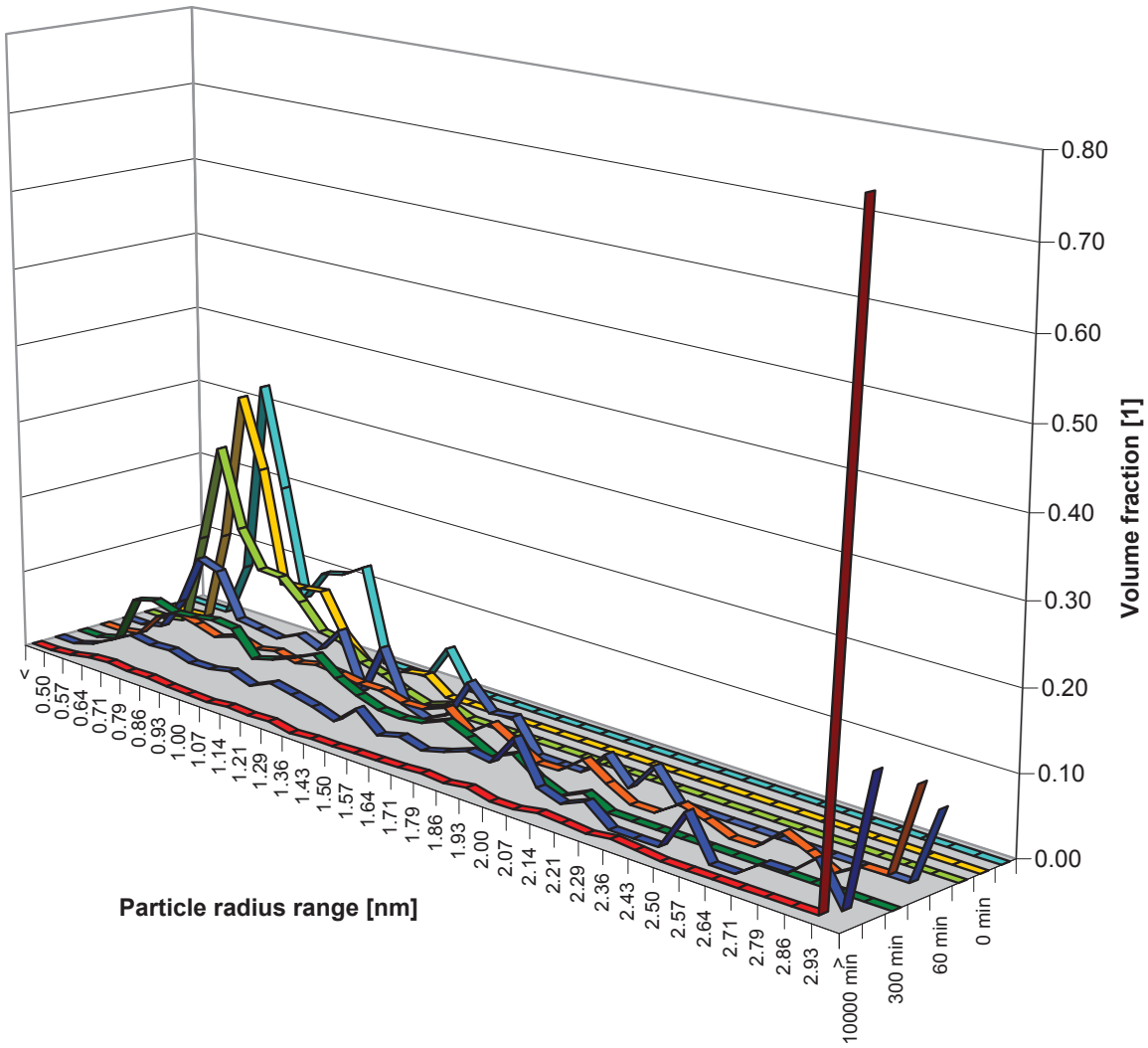

Fig. 50: The diagram shows the distribution of the relative precipitate volume versus size range. It can be seen that with increasing ageing time large precipitates account for a large fraction of the precipitate volume while at short ageing times mainly small precipitates contribute to the precipitate volume. The data are also presented in the form of conventional diagrams in Appendix II.

From this graph the trend that with increasing ageing time the majority of the precipitate volume can be accounted to the presence of large precipitates is obvious. The diagrams of specimens aged up to 30 min do not exhibit large deviations from the diagrams that show the precipitate size distribution. Between the states after 30 min and 60 min a dramatic change in the distribution of the precipitate volume has occurred. While until an ageing time of 60 min, the entire precipitated volume was constituted by precipitates with equivalent radii of less than 2 nm, at 60 min already 10 % of the precipitate volume is present in the form of clusters with equivalent radii larger than 3 nm. As stated earlier, the dataset obtained from the sample aged for 300 min does not contain precipitates larger than 2.3 nm which precludes the

possibility that these precipitates contribute to the overall precipitate volume. Disregarding the 300 min dataset, it appears that the precipitate volume fraction of precipitates with equivalent radii larger than 3 nm increases during ageing. After 1000 minutes at 500 °C 17% of the precipitate volume are attributed to this size range, whereas after 10000 minutes this value has increased to 80 %. Coarsening occurs to such an extend, that after long ageing times the volume of one single precipitate may constitute well up to 30 % of the entire precipitate volume observed in a sample volume of 30x30x30 nm^3.

In addition to the investigations concerned with the precipitate size distribution, the data obtained from atom probe experiments were analyzed with respect to the precipitate volume fraction. Although the atom probe is not very well suited for the determination of this parameter due to the fact that only small sample volumes can be investigated, the data give an idea of how large the actual precipitate volume fractions are. Figure 51 indicates a steady increase of precipitate volume fraction upon ageing, only with the exception of the samples aged for 30 and 300 min at 500 °C which do not follow the trend. In the solution annealed state and the state obtained after heating and immediate quenching, precipitate volume fractions smaller than 0.5 % are observed. After ageing for 30 min the precipitate volume fraction observed is even lower than that obtained for the solution annealed state. At 60 min at 500 °C a precipitate volume fraction of 1.3 % has been determined which increases to 1.8 % after ageing for 100 min. The dataset obtained from the specimen aged for 300 min exhibits once more a behaviour that is different from the others and manifests itself in the fact, that the precipitates constitute less than 1 % of the entire volume. After 1000 and 10000 min precipitate volume fractions of 2 and 6.6 %, respectively, were determined.

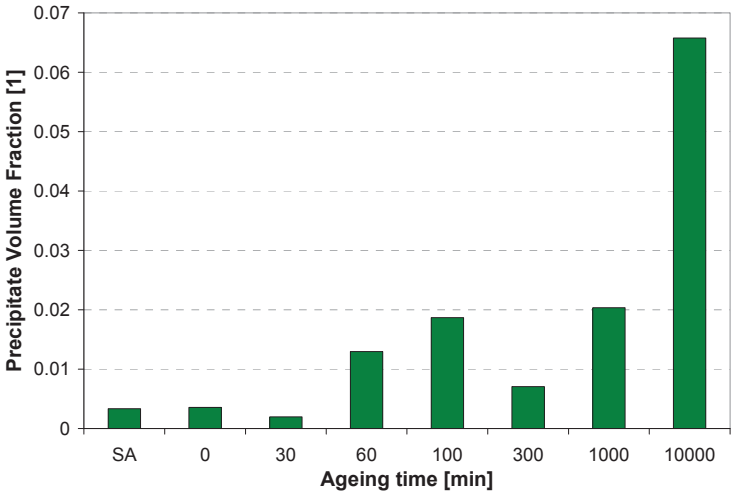

Fig. 51: Precipitate volume fractions present Fe-25 m% Co-15 m% Mo at different ageing times at 500 °C. SA indicates the solution annealed state.

Due to the small sample volume, large errors in determining the precipitate volume may arise, which is most likely the explanation for the unsteady development of precipitate volume fraction that is shown in Figure 51. Furthermore, the large influence of the cluster search parameter “separation distance” is to be acknowledged. By changing this value by

0.01 nm it is possible to double the precipitate volume fraction. An important parameter for refining the models used for analyzing SANS data is the composition of the precipitates and the matrix of the material. To determine these parameters, plots of the development of the mean composition of the precipitates upon ageing were made (Fig. 52).

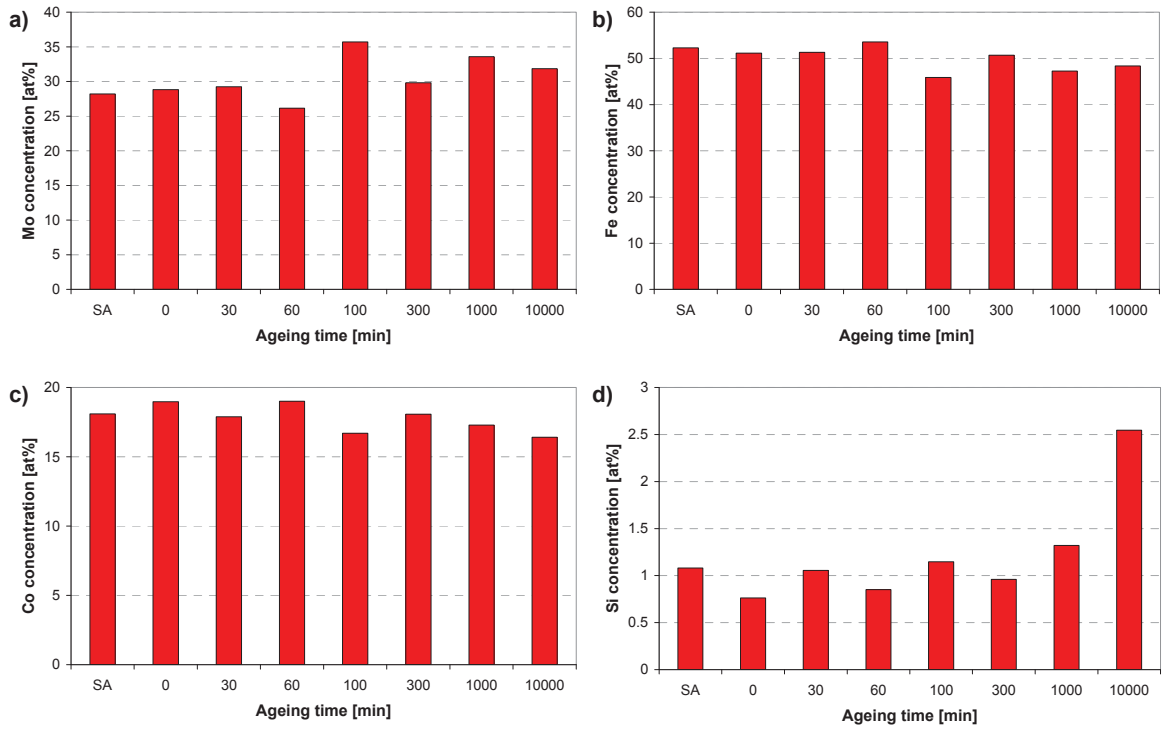

Fig. 52: Mean composition of the precipitates dependent on ageing time: (a) Mo, (b) Fe, (c) Co, and (d) Si concentration.

As ageing progresses, the Mo content increases slightly while Fe and Co contents decrease. It has to be recognized, that the data contain a considerable amount of noise and, therefore, drawing any final conclusions about the development of precipitate composition is not advisable. Some of the difficulties in determining the development in precipitate composition stem from the different bulk compositions that were determined for different specimens. The silicon concentration within the precipitates is clearly increasing upon ageing and reaches a value of 2.5 at% after ageing for 10000 min at 500 °C.

By using the macro written for extracting information from the Log-file, the mean composition of precipitates in different size ranges can be determined. An example for the dataset of the specimen aged for 100 min is given in Figure 53.

Apparently, the Mo concentration diminishes slightly with increasing particle size. The smallest particles detected have considerably higher Mo contents than larger particles. The error bars indicate the 2σ statistical error range (Eq. 10).

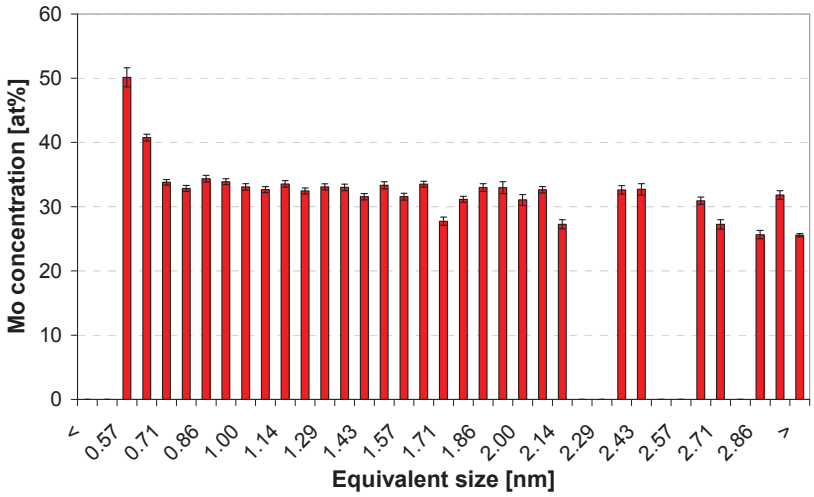

Fig. 53: Molybdenum concentration of precipitates in different size ranges after ageing for 100 min at 500 °C.

In order to be able to calculate the differences in scattering length density between particle and matrix, it is essential to have information about both, matrix and precipitate composition. The matrix composition can simply be retrieved from PoSAP and is given in Figure 54.

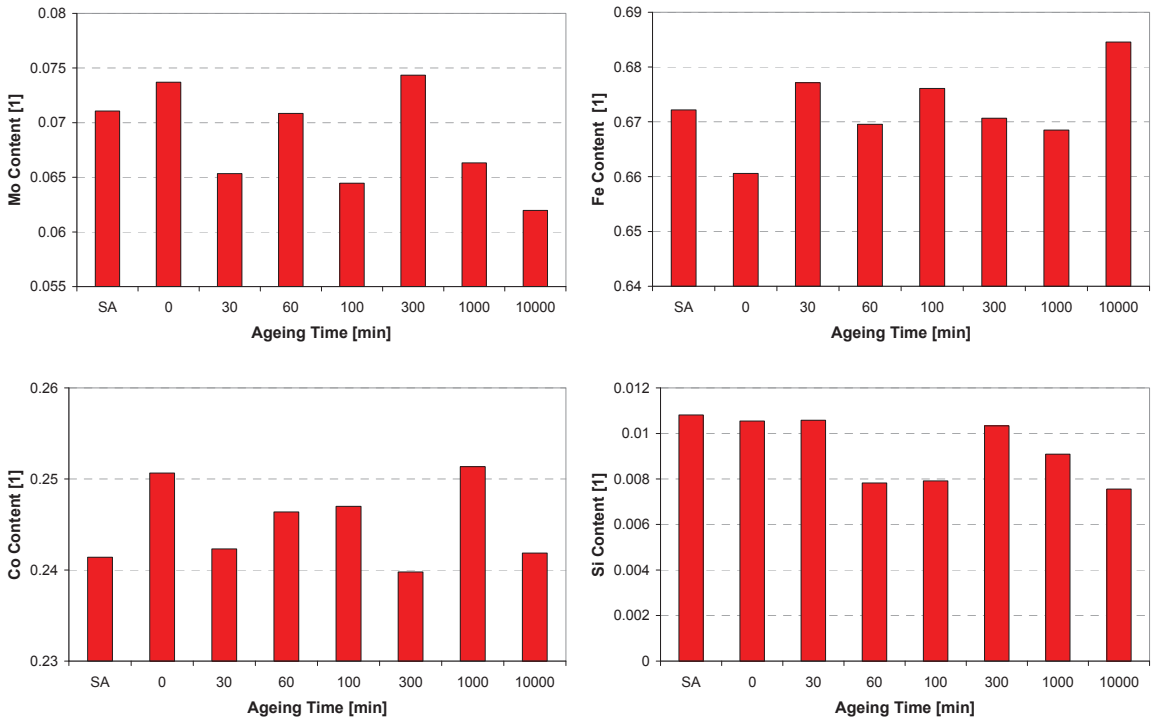

Fig. 54: Development of the matrix composition in Fe-25 m% Co-15 m% Mo with ageing time at 500 °C: (a) Mo, (b) Fe, (c) Co, and (d) Si

On the first glance, the data reveal that the variations in elemental concentrations are considerable and can mask the compositional change due to the occurring phase decomposition. Nevertheless, Si and Mo contents decrease at long ageing times while the Fe

concentration increases upon ageing. This behaviour is consistent with the results presented earlier. Due to the increase in the Mo enriched precipitate volume fraction the matrix is depleted in Mo during ageing. The chemical composition is necessary for calculating the SLDD's for nuclear and magnetic scattering. Therefore, precipitate and matrix compositions are displayed in Table 4 and Table 5, respectively.

Tab. 4: Mean precipitate composition in Fe-25 m% Co-15 m% Mo derived from atom probe analysis. SA indicates the solution annealed state.

Ageing time [min]	Precipitate composition [at%]						
	Si	Fe	Mo	Cr	Mn	Co	C
SA	0.97	52.4	27.3	0.11	0.22	19.0	0.03
0min	0.78	50.5	28.4	0.07	0.15	20.1	0.05
30min	1.07	51.9	28.3	0.07	0.29	18.2	0.02
60min	0.85	52.5	27.3	0.06	0.18	19.0	0.12
100min	1.22	48.1	31.8	0.10	0.27	18.4	0.10
300min	1.43	48.8	31.0	0.07	0.26	18.4	0.05
1000min	1.54	48.9	30.4	0.10	0.28	18.7	0.09
10000min	2.39	48.2	31.8	0.16	0.52	16.8	0.12

Tab. 5: Mean matrix composition in Fe-25 m% Co-15 m% Mo gained from atom probe experiments. SA indicates the solution annealed state.

Ageing time [min]	Matrix composition [at%]						
	Si	Fe	Mo	Cr	Mn	Co	C
SA	1.08	66.05	7.40	0.07	0.28	24.98	0.05
0min	1.06	65.19	7.69	0.07	0.27	25.58	0.05
30min	1.06	67.87	6.48	0.06	0.29	24.13	0.02
60min	0.77	66.91	7.03	0.08	0.21	24.74	0.15
100min	0.81	66.65	6.31	0.06	0.25	25.78	0.06
300min	0.99	66.94	7.04	0.06	0.26	24.60	0.03
1000min	0.94	66.28	6.77	0.07	0.27	25.53	0.06
10000min	0.78	67.80	6.61	0.07	0.27	24.26	0.06

4.4.5.4 Precipitate size characterization

Determining a size is difficult if precipitates exhibit complex shapes, like it is the case for the material investigated in this thesis. Three different ways of obtaining a mean particle radius were introduced in Section 3.4.4.5. Results obtained by these calculations are presented in Table 6.

Tab.: 6 Mean particle radii for different ageing times at 500 °C. $r_{k,m}$ is the average precipitate radius, $r_{k,v}$ is the average precipitate radius weighted with the precipitate volumes, both were obtained by using the radii of gyration in the Log-file. $r_{eq,v}$ is the mean equivalent precipitate radius which was also calculated by using the particle volume as weighting factor.

Ageing time [min]	$r_{k,m}$ [nm]	$r_{k,v}$ [nm]	$r_{eq,v}$ [nm]
SA	0.65	0.75	0.74
0	0.61	0.69	0.70
30	0.67	0.79	0.74
60	0.81	1.57	1.15
100	1.00	2.55	1.52
300	0.90	1.39	1.01
1000	1.03	2.60	1.59
10000	1.12	14.14	7.00

$r_{k,m}$ and $r_{k,v}$ are both calculated from the radii of gyration in the Log-file, the only difference being that for $r_{k,v}$ the precipitate volume was used as a weighting factor. $r_{eq,v}$ on the other hand, is the mean equivalent radius weighted by the precipitate volume. For better visualization, the mean radii obtained were plotted against ageing time (Fig. 55).

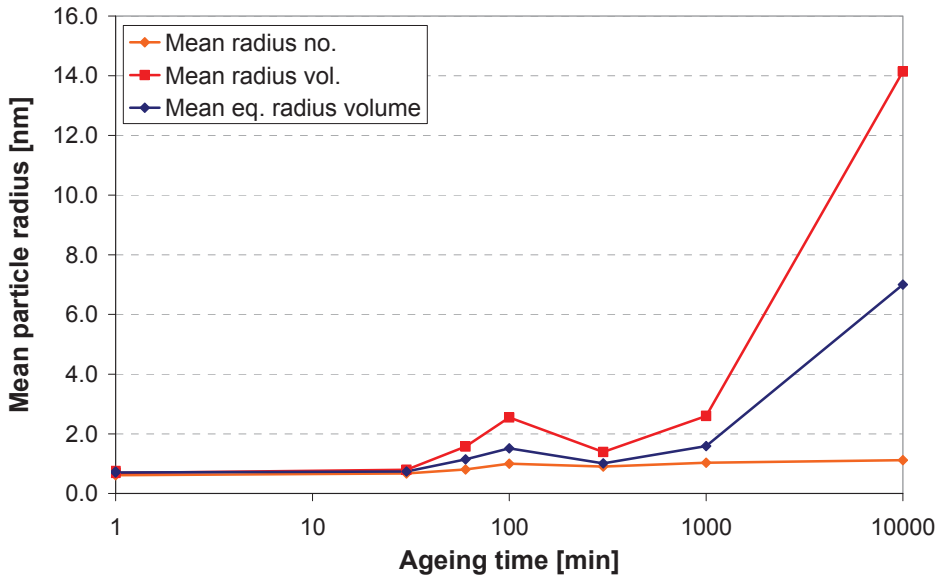

Fig. 55: Different mean precipitate radii plotted versus ageing time.

Figure 55 shows that the precipitate radius increases upon ageing. Once more, the data obtained after ageing for 300 min at 500 °C do not follow the general trend. It is obvious, that the differences in the radii obtained increases upon ageing. This behaviour can be ascribed to the formation of non-spherical, highly interconnected precipitate structures.

In the investigated Fe-25 m% Co-15 m% Mo alloy the particle shape cannot be described by means of simple geometrical models. Nonetheless does SansFit require setting an aspect ratio for the ellipsoids with rotational symmetry for describing the particle's shape. This aspect ratio was calculated facilitating the procedure introduced in Section 3.4.4.5. The results of this investigation are shown in Table 7.

Tab. 7: Mean aspect ratio of the ellipsoid axes evaluated for all ageing stages investigated by atom probe tomography. SA indicates the solution annealed state.

Ageing time [min]	Aspect ratio [1]
SA	1.67
0	1.58
30	1.57
60	1.62
100	1.57
300	1.59
1000	1.64
10000	1.58

Determining a preferential orientation of the particles out of atom probe data is treacherous because the z-coordinate of the reconstructed dataset is derived from the volume of the elemental species ranged during reconstruction and, therefore, prone to inaccuracies. If a significant number of atoms were not ranged during reconstruction, the dataset is too short. Consequently, precipitates that are of spherical shape would appear to be flattened in z-direction. In addition to that, the lateral extension of the dataset is determined by the evaporation voltage curve and the field evaporation voltage of the main constituent (Fe). This is very accurate for low alloyed materials but not for materials with large fractions of alloying elements like it is the case for the model alloy.

Nonetheless an attempt was made to evaluate the data with respect to a preferred orientation of the precipitates. To this end, the ratios of the radii of gyration in all axis direction to the mean radius of gyration were calculated. The results of this calculation are presented in Table 8 and Figure 56.

In Figure 56, the precipitates' extensions in x- and y-direction seem to be similar for most datasets, while their sizes differ significantly in z-direction. This indicates that the preferred orientation observed is an artefact of AP data reconstruction. However, it has to be noted that the ratios are all fairly close to one, which indicates that the errors introduced during reconstruction remain within an acceptable range.

Tab. 8: Ratios of the radius of gyration in one axis direction to the mean radius of gyration ($r_{g,m}$). $r_{g,x}$, $r_{g,y}$, and $r_{g,z}$ are the radii of gyration in x-, y- and z-direction, respectively. SA indicates the solution annealed state. The ageing temperature was 500 °C

Ageing time [min]	$r_{g,x}/r_{g,m}$	$r_{g,y}/r_{g,m}$	$r_{g,x}/r_{g,m}$
SA	0.974	1.014	1.012
0	1.025	0.987	0.988
30	1.019	1.031	0.950
60	1.031	1.008	0.961
100	1.100	1.140	0.760
300	1.042	1.038	0.920
1000	1.077	1.072	0.851
10000	0.982	1.036	0.982

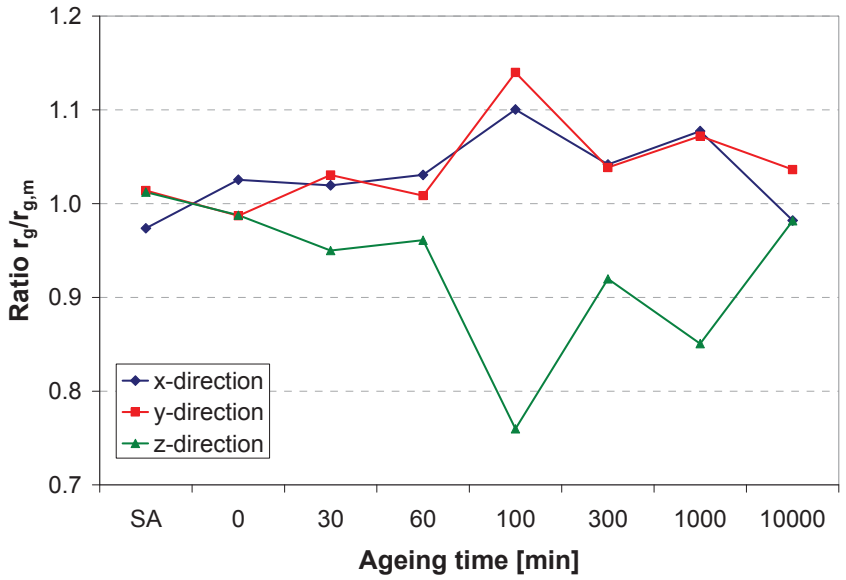

Fig. 56: Ratio of radius of gyration in one axis direction (x,y,z) to the mean radius of gyration. SA indicates the solution annealed state.

4.5 SANS experiments

The data collected in a SANS experiment are detector images like the one shown in Figure 20. After processing the images as explained in Section 3.5.4, scattering cross section versus scattering vector diagrams are obtained (Figs. 57 and 58).

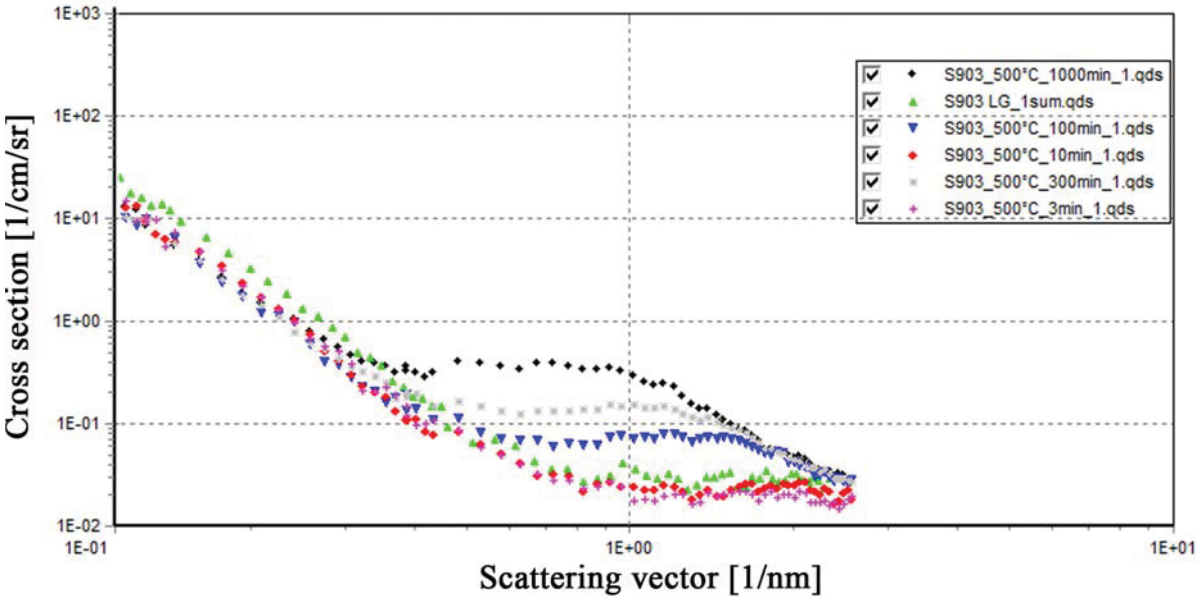

Fig. 57: Nuclear scattering patterns of Fe-25 m% Co-15 m% Mo samples aged for 3, 10, 100, 300, 1000 min at 500 °C and the solution annealed state. The intensity increases upon ageing and the maximum shifts towards smaller scattering vectors.

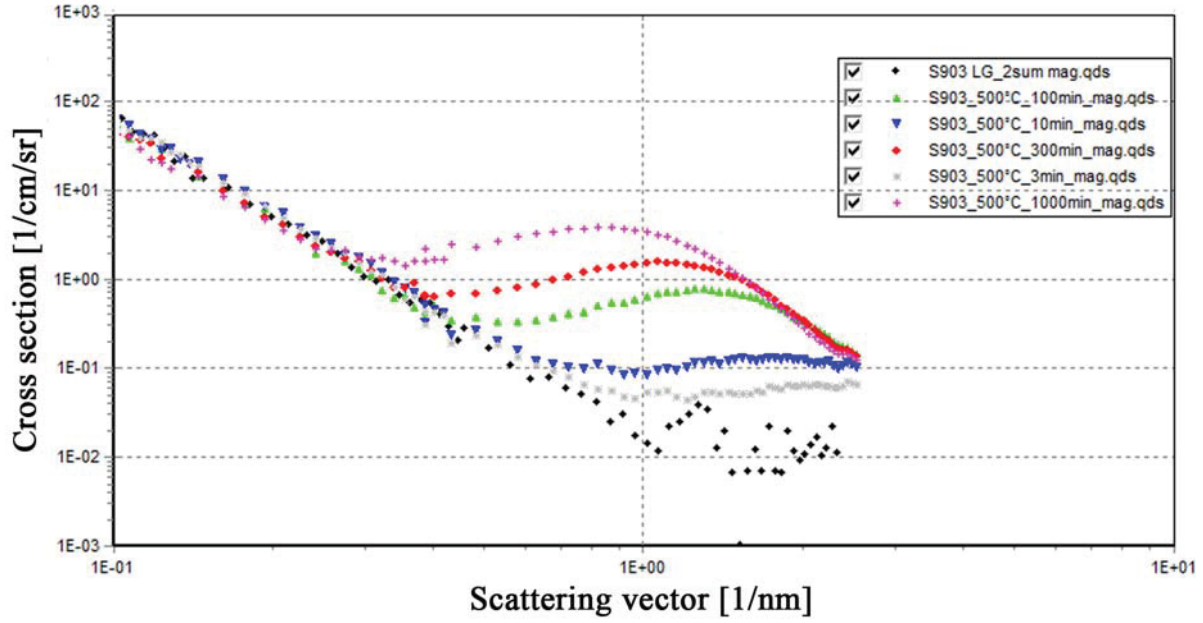

Fig. 58: Magnetic scattering patterns of Fe-25 m% Co-15 m% Mo samples aged for, 10, 100, 300, 1000 min at 500 °C and the solution annealed state.

Upon ageing the intensity of the scattering curves increases and their maximum shifts towards smaller scattering vectors. When Figures 57 and 58 are compared, it is obvious that the intensity of the magnetic scattering patterns is higher and the intensity differences between different heat treatment states are stronger pronounced. Both, the increase in intensity and the shifting of the maximum can be attributed to the formation and the growth of precipitates in the investigated volume. For quantifying the precipitate size and volume fraction the software SansFit was used. A description of the input parameters of the software is given in Section 3.5.4.

4.5.1 Parameters determined by AP-analysis

In Section 3.5.4 the parameters used for fitting the SANS pattern are introduced. In the following the parameters that were determined by AP analysis are listed.
Since the images obtained by APT reveal a highly interconnected precipitate morphology, particle interference is assumed to occur. The precipitate size distributions determined by the cluster search algorithm strongly resemble a lognormal distribution, therefore this mathematical distribution was chosen for calculating the fit.

Aspect ratio
Although the precipitates exhibit complex shapes that cannot be described by ellipsoids adequately, the precipitates were described by ellipsoids and an attempt was made to determine the aspect ratio. Details on this procedure are given in Section 3.5.4.

Orientation
Since no preferential orientation of the precipitates was recognizable in the AP analysis, a random precipitate orientation was assumed.

Scattering length density difference
The SLD's used for fitting the SANS curve were calculated from the chemical composition of matrix and precipitates. For details about how this task was performed the reader is referred to Section 3.5.4. The SLD's and SLDD's calculated are summarized in Table 9.

Tab. 9: SLD's and SLDD's for nuclear and magnetic scattering.

	Solution annealed	Ageing time [min] at 500°C				
		3	10	100	300	1000
Nuc. SLD matrix [cm^{-2}]	6.169E+10	6.134E+10	6.134E+10	6.206E+10	6.224E+10	6.187E+10
Nuc. SLD Precipitates [cm^{-2}]	5.706E+10	5.634E+10	5.634E+10	5.543E+10	5.561E+10	5.555E+10
Nuc. SLDD [cm^{-2}]	4.631E+09	5.003E+09	5.003E+09	6.637E+09	6.627E+09	6.319E+09

	Solution annealed	Ageing time [min] at 500°C				
		3	10	100	300	1000
Magn. SLD matrix [cm^{-2}]	4.963E+10	4.980E+10	4.980E+10	5.012E+10	4.989E+10	4.999E+10
Magn. SLD Precipitates [cm^{-2}]	0.000E+00	0.000E+00	0.000E+00	0.000E+00	0.000E+00	0.000E+00
Magn. SLDD [cm^{-2}]	4.963E+10	4.980E+10	4.980E+10	5.012E+10	4.989E+10	4.999E+10

As mentioned in Section 3.5.4, the magnetic SLD of the precipitates is assumed to be zero. From Table 8 it is obvious, that the magnetic SLDD's are an order of magnitude larger that the nuclear SLDD's. For this reason, only the magnetic scattering curve was used for determining precipitate size and morphology. Furthermore, the development of SLDD for nuclear and magnetic scattering is different. Whereas the nuclear SLDD varies significantly upon ageing, the magnetic SLDD remains fairly constant. This can be attributed to the fact, that the precipitates exhibit much more pronounced changes in composition than the matrix.

4.5.2 Results

If all the parameters for analyzing the pattern obtained from the SANS experiment are set, an inverse Fourier transformation is carried out to determine the particle size distribution. The mean particle radii obtained from the magnetic scattering curve are shown in Figure 59 as a function of ageing time.

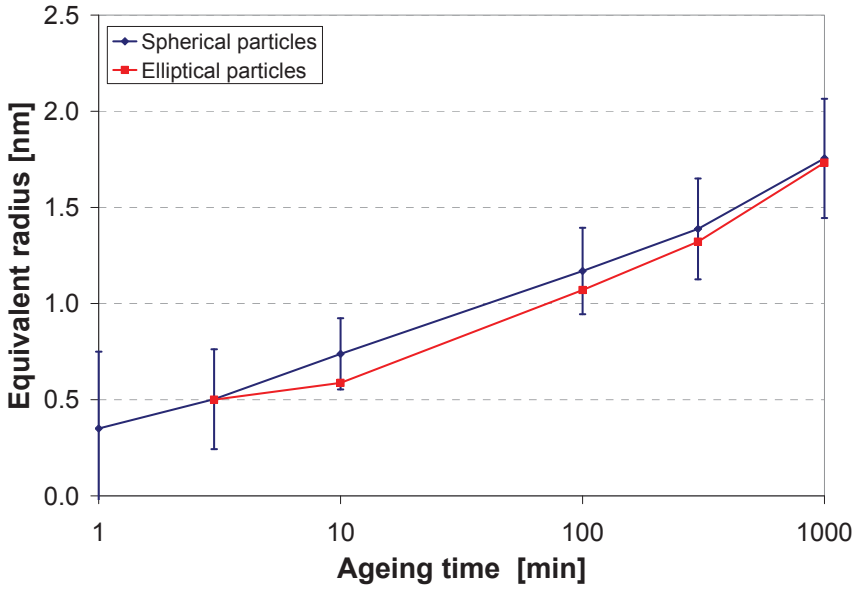

Fig. 59: Particle size development in Fe-25 m% Co-15 m% Mo upon ageing at 500 °C, obtained by analysis of the magnetic SANS curves. The red graph was calculated for the case of elliptical precipitates, while the blue graph reflects the mean radii if the particles were assumed to be spheres.

It can be seen that the mean particle radius increases steadily while ageing progresses. Furthermore, it is obvious that the differences between spherical and elliptical particles are recognizable but not overly large (Fig. 59). As a statistical indicator for the fit quality the χ^2 value is calculated by SansFit. The usage of elliptical particles does not improve the χ^2 values significantly.

The intensities from nuclear scattering are much lower than those caused by magnetic scattering which is why the analysis of magnetic scattering curves leads to lower statistical errors. On the other hand the magnetic size of the particles is a parameter which is only of significance if chemical and magnetic sizes of the particles are considered to be equal.

Additionally, the assumption that the particles are non-magnetic can only be considered a first approximation. Experiments or ab initio calculations concerning the magnetic properties of the precipitates would be necessary to improve the SANS pattern analysis. Attempts to analyze the nuclear scattering pattern were undertaken, but did not yield useful results.
The magnetic scattering patterns were investigated with respect to the precipitate volume fraction as well. Figure 60 displays the results of this investigation.
Between the solution annealed state (data point at 1 min ageing time) and the 100 min sample, the precipitate volume fraction increases steadily. After ageing for 100 min, the precipitation reaction seems to accelerate.

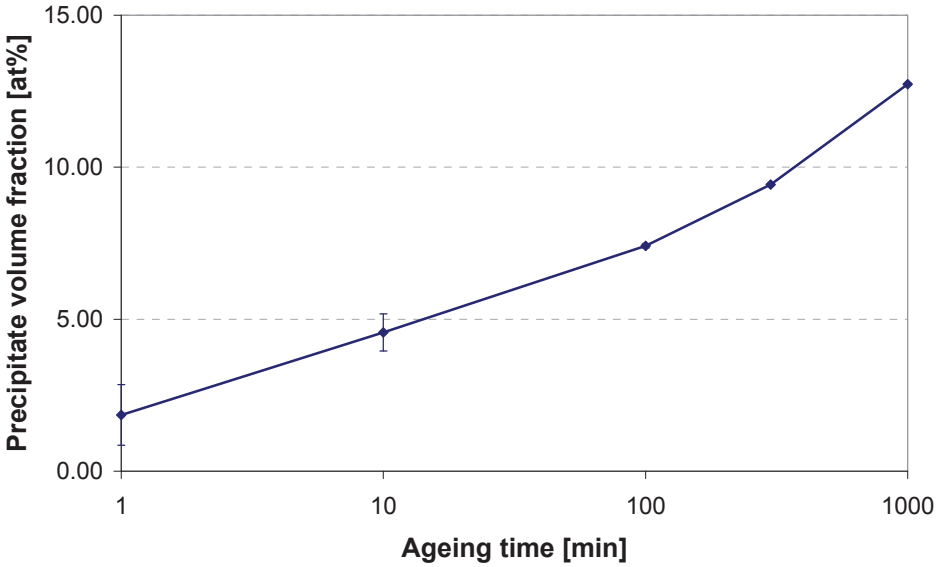

Fig. 60: Precipitate volume fraction in Fe-25 m% Co-15 m% Mo as a function of ageing time, obtained by SANS.

4.6 Comparison of AP and SANS results

The investigation of the model alloy by AP revealed that the material exhibits many characteristics that cannot be reproduced correctly by the models used for analyzing the SANS data. In the following, the results of the two complimentary methods are compared and the differences discussed.
Since the AP analysis is limited to a very small sample volume, determining precipitate number densities and volume fractions is only possible with large uncertainties. One parameter that can be determined by both methods with relatively high accuracy is the precipitate size. In the course of this diploma thesis it has been shown, that the morphology of the precipitates present is complex and, therefore, it is difficult to describe the precipitate size properly. In addition to that, after long ageing treatments the material exhibits size distributions in which a few large precipitates comprise a large fraction of the overall precipitate volume. Despite these complicating factors, the mean radius of the particles was chosen for comparing SANS and AP data (Fig. 61).

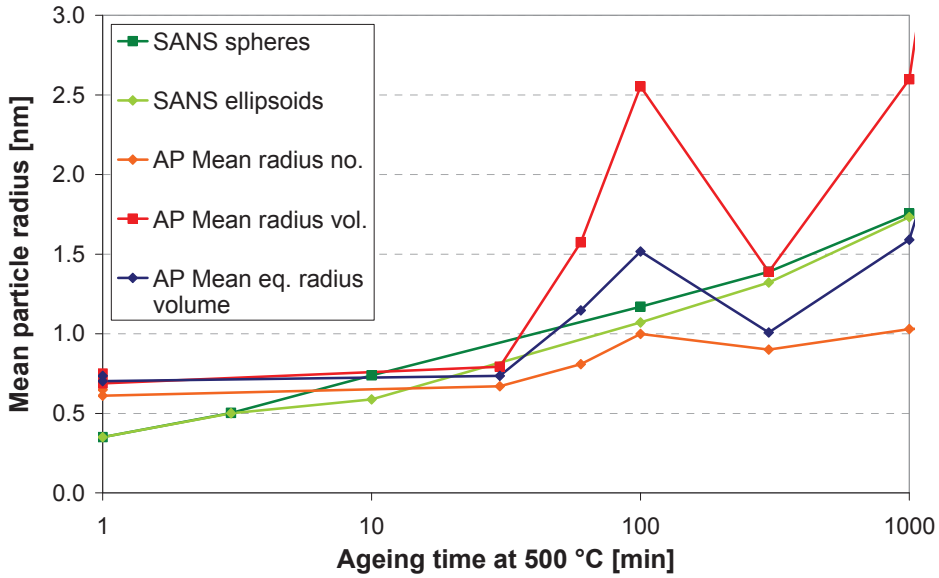

Fig. 61: Comparison between the mean particle radii obtained by SANS and AP experiments. The light green curve shows the SANS results for using elliptical particle shapes. For the dark green curve spherical shapes were assumed. Results from AP experiments are represented by the red, blue and orange curves.

Figure 61 shows that at short ageing times the radii obtained by AP are larger than those gained from SANS experiments. This can be attributed to the requirement of a cluster having to contain at least 20 Mo atoms in order to be found by the cluster search algorithm. No such requirement is imposed on the analysis of SANS data. At longer ageing times, the mean equivalent precipitate radius seems to coincide with the particle radii obtained by SANS best. In addition to the particle size, the precipitate volume fraction was chosen as a parameter for benchmarking the two analysis methods (Fig. 62).

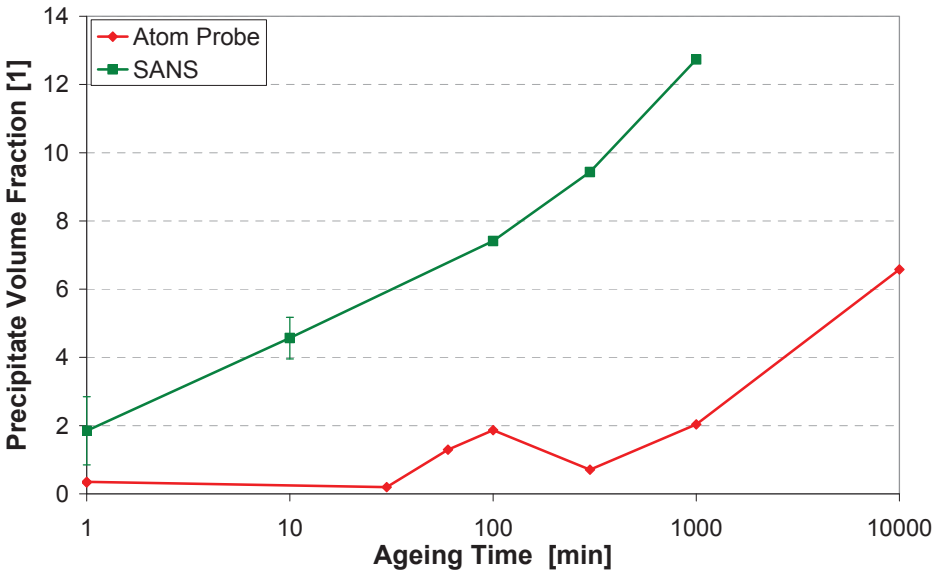

Fig. 62: Precipitate volume fractions in Fe-25 m% Co-15 m% Mo obtained by SANS and AP analysis.

Comparing the two graphs it is interesting to note that both graphs exhibit a kink at an ageing time of 100 min. While this change in precipitation rate is strongly pronounced in the AP results, it is less so in the data obtained by SANS.

It is obvious that the results of the two complementary methods AP and SANS are quite different. While the values for the mean particle diameter are at least in the same range, the precipitate volume fractions determined by SANS are up to 8 times larger than those determined by AP.

At this point, the restrictions of the methods employed and the assumptions necessary for performing the analysis shall be recapitulated:

Cluster search algorithms only find precipitates larger than a certain threshold size in the very small volume analyzed by the atom probe. For large precipitates the observable size may be limited due to the small sample volume. For this reason, size distributions of particles can only be determined for small particles.

By SANS, volumes that are 10^{13} times larger than those investigated by AP are analyzed, restrictions concerning the detection of certain particle size fractions are imposed only by the experimental facilities. In practice, large as well as small particle sizes can be detected by SANS. The restrictions of this method arise from the ability to interpret the obtained data. The particles have to be of elliptical shape, precipitates have a distinct minimal spacing in the material and if magnetic scattering curves are analyzed, it is assumed that the precipitates are not magnetic. None of these assumptions holds for the material investigated. At the early stages of precipitation, the assumption that precipitates are ellipsoids may be justified, however, at late stages it is certainly not. A particularly bold assumption is that the precipitates magnetic moment is equal to zero. Investigations on this matter are currently under progress and data for taking the magnetic moment of the precipitates into account will be available in the future.

Bearing all these restrictions and assumptions in mind, it is encouraging that the results of SANS and AP fit so well together. Some of the deviations will be discussed with respect to the restrictions mentioned.

In Figure 61 the mean particle size determined by SANS shows the tendency to be smaller than that calculated from the AP results at short ageing times. Since AP cannot detect particles below a certain threshold size, these small particles might lower the mean particle size obtained by SANS to the observed degree. An alternative explanation might be, that the cluster search algorithm interprets two spherical neighbouring Mo-rich regions connected by a narrow “string” of Mo atoms to belong to the same precipitate while during the SANS experiments these regions produce a scattering pattern that is interpreted as being caused by two particles.

One thing to bear in mind when comparing precipitate volume fractions determined by SANS and AP is that the statistics of a SANS experiment are superior to that of an AP experiment due to the larger investigated volume. At ageing times below 30 min, the SANS

results show an increase in precipitate volume fraction, while AP probe results point towards a constant precipitate volume fraction. The increase in precipitate volume fraction may be attributed to the formation of precipitates that are too small to be detected by AP, but large enough to be detected by SANS. At ageing times between 30 and 100 min the increase in precipitate volume fraction seems to be equal for AP and SANS analysis, which could be attributed to the formation of particles that can be detected by both methods employed. At 100 min a kink occurs in graph that reflects the results of the AP analysis. In the curve that represents the SANS data, a minute increase in precipitation rate is observed at an ageing time of 100 min. The reason for the AP-data curve exhibiting a discontinuity in precipitation rate at 100 min could not be revealed.

Characterizing the microstructure of the model alloy has proven to be a demanding task. In the course of this thesis, the differences in the results obtained by the two methods exploited have been revealed. It was possible to correlate the results and to explain some of the deviations qualitatively. To be able to describe the differences more quantitatively, further work would be necessary.

5. Summary and Outlook

In this diploma thesis precipitates in a Fe-25 m% Co-15 m% Mo model alloy are characterized by means of SANS and AP tomography. The aim was to compare the results of these two complimentary methods and to use the data obtained by AP experiments for the analysis of SANS patterns.

If the model alloy is subjected to a suitable solution annealing treatment, intermetallic precipitates form upon ageing at elevated temperatures. Specimens were subjected to ageing treatments at 500 °C of different length to be able to investigate the microstructural development throughout the entire ageing process. Hardness tests were conducted for every heat treatment to be able to relate the microstructural data to a macroscopic mechanical property. Experiments with the tomographic AP were conducted, which is a tool for analyzing small sample volumes with near atomic resolution. In addition to that, SANS experiments were carried out by E. Eidenberger.

The small precipitate size and the absence of a steep concentration gradient at the precipitate interface make it difficult to perform a quantitative analysis of the materials microstructure. Different methods of analyzing atom probe data were evaluated with respect to their ability to describe the nanostructure of the material properly. One method that has to be proven to be especially useful is the use of a cluster search algorithm, since it offers a high spatial resolution and allows retrieving parameters such as the radii of gyration and the volumes of single precipitates. In the course of this thesis it is shown that the results of the cluster search algorithm yield comparable results only if the atomic density of two datasets is equal. Since the atomic density depends on several experimental parameters and varies from dataset to dataset, a new method that allows taking density variations into account was developed. Determining the right parameter set for performing the cluster search was achieved by comparing the results obtained with different search parameters with the results of transmission electron microscopy. Particle size distributions and mean particle sizes as well as the precipitate volume fraction were determined by applying the cluster search to the AP datasets. The chemical composition of both precipitates and matrix was determined in order to use these data as input for the models needed to interpret the SANS patterns.

Chemical and morphological information obtained from AP analyses was used as an input for the interpretation of the SANS scattering patterns. The data interpretation was conducted with the software SansFit, which uses the principle of inverse Fourier transformation to fit the parameters of particle size distributions to the scattering patterns observed in the experiments. Since the material investigated exhibits a magnetic moment, mainly magnetic scattering was used for fitting since it provides superior statistics. Unfortunately, the analysis

of SANS data requires making assumptions about numerous material properties, including the precipitates to be of elliptical shape and having a magnetic moment equal to zero. From AP experiments it is known that the precipitates form interconnected structures and are not elliptical. To determine the magnetic properties of the precipitates simulations and/or further experiments would be necessary.

Due to those reasons it has to be assumed, that the analysis of the SANS patterns suffers from a great amount of uncertainty. Atom probe tomography suffers from the small sample volume and lacks the ability to investigate sufficiently large volumes for characterizing large precipitates.

The results in terms of particle size and particle volume fraction obtained by the two complimentary methods were compared and discussed. Although the results offer room for improvement, they coincide quite well considering the restrictions the AP method is subjected to and the assumptions that have to be made for analyzing SANS data.

Currently, research activities are in progress to determine whether the intermetallic μ-phase precipitates possess a non-zero magnetic moment. Information on the magnetic properties of the precipitates can improve the results obtained from SANS data significantly. Extending the models used currently is necessary to allow more complex shapes to be used for SANS data interpretation to be able to simulate the shapes observed in AP experiments.

The development of a cluster search algorithm that takes local density differences into account is highly desirable since this would greatly improve the reproducibility of its results.

The results of this thesis show that perfect coincidence between the results of atom probe tomography and scattering experiments cannot be achieved yet. Improvements, especially in terms of data analysis are still necessary. Considering the rapid development of software and hardware components, the goal of similar results seems to be close. It is worth to keep moving towards it.

References

[1] W. Köster, W. Tonn, Arch. Eisenhüttwes. 5, (1932), 627.

[2] W. Köster, Arch. Eisenhütwes. 6, (1932), 17.

[3] E. Houdremont, Handbuch der Sonderstahlkunde, Band 2, Stahleisen, Düsseldorf, (1956).

[4] Y.A. Geller, Instrumentalniye Staly, Metallurgia, Moscow, (1983).

[5] Y.A. Geller, Tool Steels, Mir Publishers, Moscow, (1978), 228.

[6] T. Miyazaki, S. Takagishi, H. Mori, T. Kozakai, Acta. Met. 28, (1979), 1143-1153.

[7] M. Doi, H. Tanabe, T. Miyazaki, Journal of Materials Science 22, (1987), 1328-1334.

[8] G.V. Raynor, V.G. Rivlin, International Metals Reviews Vol.29, No.5, (1984), 329.

[9] M.I. Karpov, V.I. Wuknov, N.V. Medved, H. Danninger, PM World Congress, (1998), 519.

[10] K. Izdinsky, F. Simancik, J. Ivan, M. Zemankova, TEM-Studies of Fe-Co-Mo sintered Steels, Slovac Academy of Sciences, Bratislava, (2000).

[11] A. Hirata, A. Iwai, Y. Koyama, Phys. Rev. B 74, (2006).

[12] E.W. Müller, Adv. Electron. ElectronPhys. 13, (1960), 83.

[13] E.W. Müller, Science 149, (1965), 591.

[14] M.K. Miller, Atom probe tomography: analysis at the atomic level, Kluwer Academic / Plenum Publishers, New York, (2000), 3.

[15] E.W. Müller, J. appl. Phys. 27, (1956), 474.

[16] M.K. Miller, A. Cerezo, M.G. Hetherington, G.D.W. Smith, Atom Probe Field Ion Microscopy, Oxford University Press, (1996), 6.

[17] M.K. Miller, A. Cerezo, M.G. Hetherington, G.D.W. Smith, Atom Probe Field Ion Microscopy, Oxford University Press, (1996), 2.

[18] M.K. Miller, A. Cerezo, M.G. Hetherington, G.D.W. Smith, Atom Probe Field Ion Microscopy, Oxford University Press, (1996), 3-11.

[19] E.W. Müller, T.T. Tsong, Field Ion Microscopy, Principles and Applications, Elsevier (Amsterdam), (1969).

[20] A.J. Melmed, Appl. Surf. Sci. 94/95, (1996), 17.

[21] M.K. Miller, G.D.W. Smith, Atom Probe Microanalysis, Materials Research Society, Pittsburgh, (1989), 7.

[22] M.K. Miller, A. Cerezo, M.G. Hetherington, G.D.W. Smith, Atom Probe Field Ion Microscopy, Oxford University Press, (1996), 225-267.

[23] T. Bergmann, T.P. Martin, H. Schaber, Rev. Sci. Instrum. 60, (1989), 792.

[24] M.K. Miller, A. Cerezo, M.G. Hetherington, G.D.W. Smith, Atom Probe Field Ion Microscopy, Oxford University Press, (1996), 15.

[25] A. Cerezo, T.J. Godfrey, G.D.W. Smith, Rev. Sci. Instrum. 59, (1988), 862.

[26] A. Cerezo, T.J. Godfrey C.R.M. Grovenor M.G. Hetherington, R.M. Hoyle, J.P. Jakubovics, J.A. Liddle, G.D.W. Smith, G.M. Worral, J. Microsc. 154, (1989), 215.

[27] M.K. Miller, A. Cerezo, M.G. Hetherington, G.D.W. Smith, Atom Probe Field Ion Microscopy, Oxford University Press, (1996), 19.

[28] LEAP Training class, Operations and Applications II, IMAGO Scientific Instruments, (2007).

[29] G.L. Kellog, T.T. Tsong, J. Appl. Phys. 51, (1980), 1184.

[30] M.K. Miller, A. Cerezo, M.G. Hetherington, G.D.W. Smith, Atom Probe Field Ion Microscopy, Oxford University Press, (1996), 24.

[31] LEAP Training class, Advanced Data Reconstruction and Analysis, IMAGO Scientific Instruments, (2007).

[32] M.K. Miller, A. Cerezo, M.G. Hetherington, G.D.W. Smith, Atom Probe Field Ion Microscopy, Oxford University Press, (1996), 274-277.

[33] P. Bas, A. Bostel, B. Deconihout, D. Blavette, Appl. Surf. Sci. 78/88, (1995), 298.

[34] O.C. Hellman, J. Blatz du Rivage, D.N. Seidman, ultramicroscopy 95, (2003), 199-205.

[35] M.K. Miller, A. Cerezo, M.G. Hetherington, G.D.W. Smith, Atom Probe Field Ion Microscopy, Oxford University Press, (1996), 314-323.

[36] M.K. Miller, A. Cerezo, M.G. Hetherington, G.D.W. Smith, Atom Probe Field Ion Microscopy, Oxford University Press, (1996), 310-311.

[37] O.C. Hellman, J.A. Vandenbroucke, J. Rüsing, D. Isheim, D.N. Seidman, Microsc. Microanal. 6, (2000), 437-444.

[38] D. Vaumousse, A. Cerezo, P.J. Warren, ultramicroscopy 95, (2003), 215-221.

[39] M. Zandbergen, A. Cerezo, G. Smith, Detection of early stage precipitates in Al 6xxx alloys, Presentation at APFIM Workshop in Göteborg, Sweden, June (2007).

[40] W. Reimers, A.R. Pyzalla, A. Schreyer, H. Clemens, Neutrons and Synchrotron Radiation in Engineering Materials Science, Wiley-VCH, Weinheim, (2008)

[41] Structure Analysis by Small-Angle X-Ray and Neutron Scattering, L.A. Feigin, D.I. Svergun, Plenum Press, New York, (1978)

[42] A. Cerezo, L. Davin, Surf. Interface Anal. 39, (2007), 184-188.

[43] P. Staron, Early stages of the decomposition reaction in a Ni-13at%Al alloy – polarized small-angle neutron scattering and clusterdynamic modelling, Doctoral Thesis, Geesthacht, (1997).

[44] M. Bischof, Characterization of second-phase particles in metallic high-performance materials, Doctoral Thesis, Leoben, (2006).

[45] A.J. Dianoux, G. Lander (Eds.), Neutron data booklet, Institut Laue Langevin, Grenoble, (2001).

[46] S.W. Lovesey, Theory of Neutron Scattering from Condensed Matter, Vol. 1, Clarendon Press, Oxford, (2004).

[47] A.E. Berkowitz, E. Kneller (Eds.), Magnetism and Metallury, Academic Press, New York, (1969).

[48] G. Kostorz, H. Herman, Treatise on Materials Science and Technology, Vol. 15.

[49] J.S. Pedersen, Neutrons, X-Rays and Light, Elsevier Science B.V., (2002).

[50] H. Leitner, P. Staron, H. Clemens, S. Marsoner, P. Warbichler, Materials Science and Engineering A 389, (2005), 323-331.

[51] M. Bischof, P. Staron, D. Caliskanoglu, H. Leitner, C. Scheu, H. Clemens, Materials Science and Engineering A 472, (2008), 148-152.

[52] M.K. Miller, A. Cerezo, M.G. Hetherington, G.D.W. Smith, Atom Probe Field Ion Microscopy, Oxford University Press, (1996), 476.

[53] M.K. Miller, Atom probe tomography: analysis at the atomic leve, Kluwer Academic / Plenum Publishers, New York, (2000), 25-43.

[54] H. Eckerlebe, Diploma Thesis, GKSS Forschungszentrum, Geesthacht, (1985).

[55] O. Madelung, Landolt Börnstein, Gruppe III, Crystal and Solid State Physics, Vol. 19b, Magnetic properties of Materials, (1994).

[56] R.M. Bozorth, Ferromagnetism, Wiley, (2003).

[57] E. Eidenberger, E. Stergar, H. Leitner, C. Scheu, P. Staron, H. Clemens, Precipitates in a Fe-Co-Mo Alloy Characterized by Complementary Methods, BHM 153, (2008).

[58] M. Schober, Thermische Analyse von Ausscheidungsgehärteten Stählen, Diploma Thesis, University of Leoben, (2006).

Appendix I

In the following, the source code of the Mathematica Fourier-transformation algorithm is presented. The routine generates a list with 20000 entries. These entries, if plotted with constant spacing, represent oscillations of three sine-functions. This list is then Fourier transformed and the result is plotted in a diagram.

```
ValList={};
LaufList={};
x=1;
For [i=1, i≤ 20000, i++,
  ValList=Append[ValList,N[Sin[i/20]]+N[Sin[i/100]]+N[Sin[i/10]]];
  LaufList=Append[LaufList,x];
  x++;
  ]
ListPlot[ValList]
```

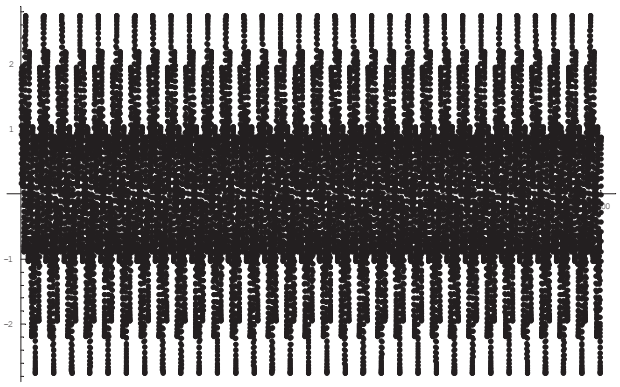

End of datalist generation.

```
OutList={};
TransList=Fourier[ValList];
For[ i=1, i≤ Length[ValList], i++,
  OutList=Append[OutList,Abs[TransList[[i]]]];
  ]
ListPlot[OutList,PlotJoined→True, PlotRange→{{0,500},All}]
```

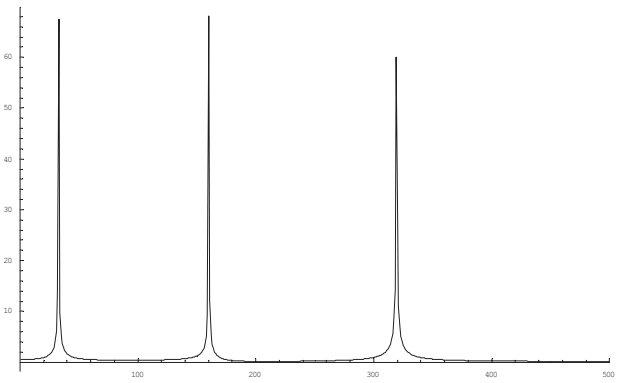

The result of the Fourier transformation is a plot with three distinct peaks whose positions represent the wavelength of the oscillations.

For the transformation of AP data the same algorithm is used. Before the data out of 1-d concentration profiles are Fourier transformed, they are brought into a form that can be read

by the Mathematica routine. Furthermore, a number of concentration profiles are assembled in order to cover a larger q-range.

```
ConcList={};

FullMat=Import["C://Users//Thomas Schmölzer//Uni//Diplomarbeit//First
Reconstruction//Mathematica//Konzentration//Konz 1000 min//Pos1
2.csv"];

For [i=2, i≤Length[FullMat]-1, i++,
    ConcList=Append[ConcList,FullMat[[i,6]]];
    ];

FullMat=Import["C://Users//Thomas Schmölzer//Uni//Diplomarbeit//First
Reconstruction//Mathematica//Konzentration//Konz 1000 min//Pos2
2.csv"];

For [i=2, i≤Length[FullMat]-1, i++,
    ConcList=Append[ConcList,FullMat[[i,6]]];
    ];

FullMat=Import["C://Users//Thomas Schmölzer//Uni//Diplomarbeit//First
Reconstruction//Mathematica//Konzentration//Konz 1000 min//Pos3
2.csv"];

For [i=2, i≤Length[FullMat]-1, i++,
    ConcList=Append[ConcList,FullMat[[i,6]]];
    ];

FullMat=Import["C://Users//Thomas Schmölzer//Uni//Diplomarbeit//First
Reconstruction//Mathematica//Konzentration//Konz 1000 min//Pos4
2.csv"];

For [i=2, i≤Length[FullMat]-1, i++,
    ConcList=Append[ConcList,FullMat[[i,6]]];
    ];

FullMat=Import["C://Users//Thomas Schmölzer//Uni//Diplomarbeit//First
Reconstruction//Mathematica//Konzentration//Konz 1000 min//Pos5
2.csv"];

For [i=2, i≤Length[FullMat]-1, i++,
    ConcList=Append[ConcList,FullMat[[i,6]]];
    ];

FullMat=Import["C://Users//Thomas Schmölzer//Uni//Diplomarbeit//First
Reconstruction//Mathematica//Konzentration//Konz 1000 min//Pos6
2.csv"];

For [i=2, i≤Length[FullMat]-1, i++,
    ConcList=Append[ConcList,FullMat[[i,6]]];
    ];

FullMat=Import["C://Users//Thomas Schmölzer//Uni//Diplomarbeit//First
Reconstruction//Mathematica//Konzentration//Konz 1000 min//Pos7
2.csv"];

For [i=2, i≤Length[FullMat]-1, i++,
    ConcList=Append[ConcList,FullMat[[i,6]]];
    ];

FullMat=Import["C://Users//Thomas Schmölzer//Uni//Diplomarbeit//First
Reconstruction//Mathematica//Konzentration//Konz 1000 min//Pos8
2.csv"];

For [i=2, i≤Length[FullMat]-1, i++,
    ConcList=Append[ConcList,FullMat[[i,6]]];
    ];
```

```
FullMat=Import["C://Users//Thomas Schmölzer//Uni//Diplomarbeit//First
Reconstruction//Mathematica//Konzentration//Konz 1000 min//Pos9
2.csv"];

For [i=2, i≤Length[FullMat]-1, i++,
    ConcList=Append[ConcList,FullMat[[i,6]]];
    ];

FullMat=Import["C://Users//Thomas Schmölzer//Uni//Diplomarbeit//First
Reconstruction//Mathematica//Konzentration//Konz 1000 min//Pos10
2.csv"];

For [i=2, i≤Length[FullMat]-1, i++,
    ConcList=Append[ConcList,FullMat[[i,6]]];
    ];

ListPlot[ConcList, PlotJoined→True];
```

The following graph reflects the composition profile read into the mathematic routine.

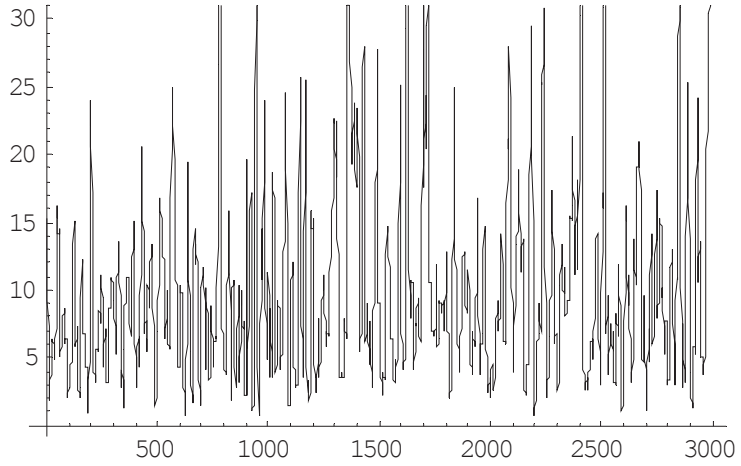


```
OutMoList={};
OutMoList=Abs[Fourier[MoList]];
ListPlot[OutMoList,PlotJoined→True, PlotRange→{0,100} ]
```

This graph reflects the power spectrum of the transformed composition profile.

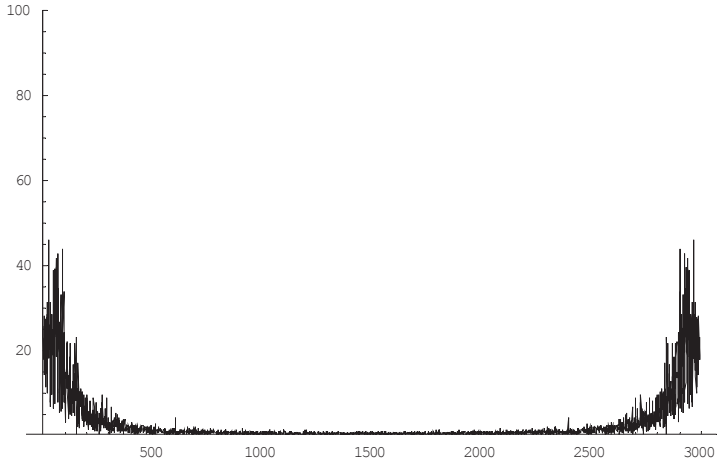


```
 FormatPlot={};
For[i=1, i≤119, i++,
  FormatPlot=Append[FormatPlot,OutMoList[[i]]];
  ]
ListPlot[FormatPlot, PlotJoined→True, PlotRange→{0,50}]
```

In the following figure, the part that contains wavelengths relevant to a decomposition process is magnified.

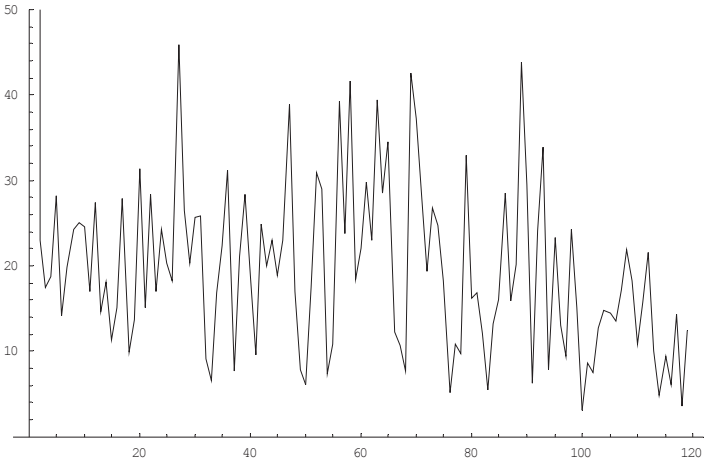

If the results of a cluster search are written to the Log-file of PoSAP, the data are stored in a format that necessitates the use of a routine to extract the information relevant for the user. A short excerpt of a Log-file that contains the results of a cluster search is shown below.

```
Number of particles detected: 347
```

Particle	Ion	No. ions	Mean Position			Radius of Gyration		
			x	y	z	x	y	z
1	All	113	-8.3295	11.2296	-14.5590	0.5352	1.1799	0.2372
1	Fe	42	-8.1648	11.1310	-14.5419	0.5320	1.0627	0.2290
1	Mo	53	-8.4390	11.3169	-14.5651	0.5267	1.2206	0.2419
1	Co	16	-8.4400	11.2385	-14.5496	0.4669	1.2593	0.2334
1	Cu	1	-7.7770	12.4211	-14.7313	0.0000	0.0000	0.0000
1	Si	1	-8.2242	9.4150	-14.9276	0.0000	0.0000	0.0000
2	All	126	16.6579	-20.7869	-14.3825	0.4334	0.3881	0.4120
2	Fe	76	16.6820	-20.8116	-14.3892	0.4008	0.3844	0.4176
2	Mo	29	16.6294	-20.8242	-14.3188	0.5291	0.4250	0.4315
2	Co	21	16.6096	-20.6462	-14.4463	0.3915	0.3090	0.3470
3	All	72	7.2914	5.0368	-14.6142	0.5240	0.4126	0.2502
3	Fe	34	7.1739	5.0934	-14.6212	0.4910	0.4089	0.2488
3	Mo	22	7.2736	5.0569	-14.5696	0.5257	0.4620	0.2696
3	Co	16	7.5657	4.8887	-14.6605	0.4880	0.2970	0.2124
4	All	130	-28.9684	5.1250	-14.4076	0.6265	0.6560	0.3502
4	Fe	57	-29.0423	5.0277	-14.4644	0.6169	0.6435	0.3791
4	Mo	46	-28.9697	5.2664	-14.3465	0.6439	0.6223	0.3383
4	Cr	1	-29.2902	5.9534	-14.0685	0.0000	0.0000	0.0000
4	Co	20	-28.8414	4.9643	-14.4087	0.5542	0.6961	0.2840
4	Si	6	-28.6271	5.3629	-14.3886	0.6701	0.5528	0.2583

For extracting the information used and writing it to an Excel-Sheet the following Visual Basic routine was conceived.

```
Sub VolVert()

Particle = 0

PcptNoPos = 1
ElementPos = 2
AtNoPos = 3
GyrXPos = 7
GyrYPos = 8
GyrZPos = 9


RowOffsetW = 7

PartPosW = 1
PartVolPosW = 2
GyrXPosW = 3
GyrYPosW = 4
GyrZPosW = 5

TotAtNoPosW = 6
FeAtNoPosW = 7
CoAtNoPosW = 8
MoAtNoPosW = 9
SiAtNoPosW = 10
CAtNoPosW = 11
MnAtNoPosW = 12
CrAtNoPosW = 13

Sheets("Tabelle2").Cells(RowOffsetW - 1, PartPosW) = "Particle No"
```

```
Sheets("Tabelle2").Cells(RowOffsetW - 1, PartVolPosW) = "Particle
Volume [nm^3]"

Sheets("Tabelle2").Cells(RowOffsetW - 1, GyrXPosW) = "Radius of
Gyration x [nm]"
Sheets("Tabelle2").Cells(RowOffsetW - 1, GyrYPosW) = "Radius of
Gyration y [nm]"
Sheets("Tabelle2").Cells(RowOffsetW - 1, GyrZPosW) = "Radius of
Gyration z [nm]"

Sheets("Tabelle2").Cells(RowOffsetW - 1, TotAtNoPosW) = "Total No of
Atoms"
Sheets("Tabelle2").Cells(RowOffsetW - 1, FeAtNoPosW) = "No of Fe
Atoms"
Sheets("Tabelle2").Cells(RowOffsetW - 1, CoAtNoPosW) = "No of Co
Atoms"
Sheets("Tabelle2").Cells(RowOffsetW - 1, MoAtNoPosW) = "No of Mo
Atoms"
Sheets("Tabelle2").Cells(RowOffsetW - 1, SiAtNoPosW) = "No of Si
Atoms"
Sheets("Tabelle2").Cells(RowOffsetW - 1, CAtNoPosW) = "No of C Atoms"
Sheets("Tabelle2").Cells(RowOffsetW - 1, MnAtNoPosW) = "No of Mn
Atoms"
Sheets("Tabelle2").Cells(RowOffsetW - 1, CrAtNoPosW) = "No of Cr
Atoms"


For Row = 1 To 10000

    Element = Sheets("Tabelle1").Cells(Row, ElementPos).Value
    ParticleVol = 0


    If Element = "All" Then
     Particle = Particle + 1
     Sheets("Tabelle2").Cells(RowOffsetW + Particle, TotAtNoPosW) =
       Sheets("Tabelle1").Cells(Row, AtNoPos).Value

     For PartRow = 1 To 14
      ParticleNo = Sheets("Tabelle1").Cells(Row + PartRow,
       PcptNoPos).Value

      If Particle = ParticleNo Then
       ParticleVol = ParticleVol + ElVol(Row + PartRow, ElementPos)
      Else
       Exit For
      End If
     Next PartRow

     Sheets("Tabelle2").Cells(RowOffsetW + Particle, PartPosW) =
       Particle
     Sheets("Tabelle2").Cells(RowOffsetW + Particle, PartVolPosW) =
       ParticleVol
     Sheets("Tabelle2").Cells(RowOffsetW + Particle, GyrXPosW) =
       Sheets("Tabelle1").Cells(Row, GyrXPos).Value
     Sheets("Tabelle2").Cells(RowOffsetW + Particle, GyrYPosW) =
       Sheets("Tabelle1").Cells(Row, GyrYPos).Value
     Sheets("Tabelle2").Cells(RowOffsetW + Particle, GyrZPosW) =
       Sheets("Tabelle1").Cells(Row, GyrZPos).Value

    End If

    If Element = "Fe" Then
```

```
        Sheets("Tabelle2").Cells(RowOffsetW + Particle, FeAtNoPosW) =
           Sheets("Tabelle1").Cells(Row, AtNoPos).Value
       End If

       If Element = "Co" Then
        Sheets("Tabelle2").Cells(RowOffsetW + Particle, CoAtNoPosW) =
           Sheets("Tabelle1").Cells(Row, AtNoPos).Value
       End If

       If Element = "Mo" Then
        Sheets("Tabelle2").Cells(RowOffsetW + Particle, MoAtNoPosW) =
           Sheets("Tabelle1").Cells(Row, AtNoPos).Value
       End If

       If Element = "Si" Then
        Sheets("Tabelle2").Cells(RowOffsetW + Particle, SiAtNoPosW) =
           Sheets("Tabelle1").Cells(Row, AtNoPos).Value
       End If

       If Element = "C" Then
        Sheets("Tabelle2").Cells(RowOffsetW + Particle, CAtNoPosW) =
           Sheets("Tabelle1").Cells(Row, AtNoPos).Value
       End If

       If Element = "Cr" Then
        Sheets("Tabelle2").Cells(RowOffsetW + Particle, CrAtNoPosW) =
           Sheets("Tabelle1").Cells(Row, AtNoPos).Value
       End If

       If Element = "Mn" Then
        Sheets("Tabelle2").Cells(RowOffsetW + Particle, MnAtNoPosW) =
           Sheets("Tabelle1").Cells(Row, AtNoPos).Value
       End If

   Next Row

   End Sub
```

This routine does not only rearrange the data, it also calculates the volume of every precipitate by using the information on the atomic volumes that is utilized by IVAS for reconstructing the sample volume. For this step a sub-routine is used that is shown below.

```
Function ElVol(Row, Col)

Vol = "x"

FeVol = 0.0118
SiVol = 0.02
MoVol = 0.0156
CuVol = 0.0118
CrVol = 0.012
MnVol = 0.012
CoVol = 0.011
CVol = 0.009

Wert = Sheets("Tabelle1").Cells(Row, Col).Value

Vol = 0

If Wert = "All" Then
    Vol = 0
```

```
End If

If Wert = "Fe" Then
    Vol = Sheets("Tabelle1").Cells(Row, Col + 1).Value * FeVol
End If

If Wert = "Si" Then
    Vol = Sheets("Tabelle1").Cells(Row, Col + 1).Value * SiVol
End If

If Wert = "Mo" Then
    Vol = Sheets("Tabelle1").Cells(Row, Col + 1).Value * MoVol
End If

If Wert = "Cu" Then
    Vol = Sheets("Tabelle1").Cells(Row, Col + 1).Value * CuVol
End If

If Wert = "Cr" Then
    Vol = Sheets("Tabelle1").Cells(Row, Col + 1).Value * CrVol
End If

If Wert = "Mn" Then
    Vol = Sheets("Tabelle1").Cells(Row, Col + 1).Value * MnVol
End If

If Wert = "Co" Then
    Vol = Sheets("Tabelle1").Cells(Row, Col + 1).Value * CoVol
End If

If Wert = "C" Then
    Vol = Sheets("Tabelle1").Cells(Row, Col + 1).Value * CVol
End If

ElVol = Vol

End Function
```

For evaluating the particle size distribution, another routine was written that performs this task by using the table that has been created by the routine VolVert shown above. This routine has three almost identical parts. The first part evaluates the number of precipitates smaller than the lower size threshold, the second part counts the number of precipitates in every size range while the last part determines the number of precipitates larger than the upper threshold. All input parameters can be adjusted at the very beginning of the routine.

```
Sub SizeDist()

Pi = 3.14159


Smallest = 0.5
Largest = 10
NoOfGroups = 35

Offset = 8
PartNoPos = 1
SizePos = 2
GyrXPos = 3
GyrYPos = 4
GyrZPos = 5
```

```
AllNoPos = 6
LowerElDesignator = 7
UpperElDesignator = 13


RowOffsetW = 8
GroupPosW = 1
NoPosW = 2
SizePosW = 3
GyrXPosW = 4
GyrYPosW = 5
GyrZPosW = 6
NoOfAllAtomsW = 7
LowerElW = 8
```

Until here the user supposed to change the parameters.

```
SizeStep = (Largest - Smallest) / NoOfGroups

Sheets("Tabelle4").Cells(RowOffsetW - 1 + GroupCount, SizePosW) =
"Mean Radius[nm]"
Sheets("Tabelle4").Cells(RowOffsetW - 1 + GroupCount, NoPosW) = "No of
Particles"
Sheets("Tabelle4").Cells(RowOffsetW - 1 + GroupCount, GroupPosW) =
"Fraction (lower bound radius) [nm]"
Sheets("Tabelle4").Cells(RowOffsetW - 1 + GroupCount, GyrXPosW) =
"GyrXMean [nm]"
Sheets("Tabelle4").Cells(RowOffsetW - 1 + GroupCount, GyrYPosW) =
"GyrYMean [nm]"
Sheets("Tabelle4").Cells(RowOffsetW - 1 + GroupCount, GyrZPosW) =
"GyrZMean [nm]"
Sheets("Tabelle4").Cells(RowOffsetW - 1 + GroupCount, 7) = "No of All
Atoms"
Sheets("Tabelle4").Cells(RowOffsetW - 1 + GroupCount, 8) = "Fe Conc"
Sheets("Tabelle4").Cells(RowOffsetW - 1 + GroupCount, 9) = "Co Conc"
Sheets("Tabelle4").Cells(RowOffsetW - 1 + GroupCount, 10) = "Mo Conc"
Sheets("Tabelle4").Cells(RowOffsetW - 1 + GroupCount, 11) = "Si Conc"
Sheets("Tabelle4").Cells(RowOffsetW - 1 + GroupCount, 12) = "C Conc"
Sheets("Tabelle4").Cells(RowOffsetW - 1 + GroupCount, 13) = "Mn Conc"
Sheets("Tabelle4").Cells(RowOffsetW - 1 + GroupCount, 14) = "Cr Conc"
```

End of the labelling section.

```
SizeSum = 0
GyrXSum = 0
GyrYSum = 0
GyrZSum = 0
MoSum = 0
AllSum = 0
NoOfParticles = 0
TotNoOfParticles = 0
Dim NoOfElAtoms(20)

For Row = Offset To 1000
    PartNo = Sheets("Tabelle2").Cells(Row, PartNoPos)
    If TotNoOfParticles < PartNo Then
        TotNoOfParticles = PartNo
    End If
Next Row

TotNoOfParticles = TotNoOfParticles - 1
```

```
For i = 0 To 19
    NoOfElAtoms(i) = 0
Next i



For Row = Offset To 1000

    Size = (4 * Sheets("Tabelle2").Cells(Row, SizePos) / (3 * Pi)) ^
            (1 / 3)
```

The precipitate size is the radius of a sphere that has the same volume as the precipitate.

```
        If Size < Smallest And Size > 0 Then
            SizeSum = SizeSum + Size
            NoOfParticles = NoOfParticles + 1
            GyrXSum = GyrXSum + Sheets("Tabelle2").Cells(Row,
              GyrXPos).Value
            GyrYSum = GyrYSum + Sheets("Tabelle2").Cells(Row,
              GyrYPos).Value
            GyrZSum = GyrZSum + Sheets("Tabelle2").Cells(Row,
              GyrZPos).Value
            AllSum = AllSum + Sheets("Tabelle2").Cells(Row,
              AllNoPos).Value

            Counter = 0

            For ElDesignator = LowerElDesignator To UpperElDesignator
                NoOfElAtoms(Counter) = NoOfElAtoms(Counter) +
                   Sheets("Tabelle2").Cells(Row, ElDesignator).Value
                Counter = Counter + 1
            Next ElDesignator

        End If

    Next Row

    If NoOfParticles = 0 Then
        SizeMean = 0
        GyrXMean = 0
        GyrYMean = 0
        GyrZMean = 0

        Counter = 0

        For ElDesignator = LowerElDesignator To UpperElDesignator
            Sheets("Tabelle4").Cells(RowOffsetW + GroupCount, LowerElW +
              Counter) = 0
            Counter = Counter + 1
        Next ElDesignator

    Else
        SizeMean = SizeSum / NoOfParticles
        GyrXMean = GyrXSum / NoOfParticles
        GyrYMean = GyrYSum / NoOfParticles
        GyrZMean = GyrZSum / NoOfParticles

        Counter = 0

        For ElDesignator = LowerElDesignator To UpperElDesignator
```

```
            Sheets("Tabelle4").Cells(RowOffsetW + GroupCount, LowerElW +
              Counter) = NoOfElAtoms(Counter) / AllSum
            Counter = Counter + 1
        Next ElDesignator

    End If

    Sheets("Tabelle4").Cells(RowOffsetW, SizePosW) = SizeMean
    Sheets("Tabelle4").Cells(RowOffsetW, NoPosW) = NoOfParticles /
    TotNoOfParticles
    Sheets("Tabelle4").Cells(RowOffsetW, GroupPosW) = "<"
    Sheets("Tabelle4").Cells(RowOffsetW + GroupCount, GyrXPosW) = GyrXMean
    Sheets("Tabelle4").Cells(RowOffsetW + GroupCount, GyrYPosW) = GyrYMean
    Sheets("Tabelle4").Cells(RowOffsetW + GroupCount, GyrZPosW) = GyrZMean
    Sheets("Tabelle4").Cells(RowOffsetW + GroupCount, NoOfAllAtomsW) =
    AllSum
```

End of the first section. In the loop that starts 8 lines below, the number of precipitates in every single size range is determined.

```
    SizeSum = 0
    GyrXSum = 0
    GyrYSum = 0
    GyrZSum = 0
    MoSum = 0
    AllSum = 0

    For GroupCount = 1 To NoOfGroups

        SizeSum = 0
        GyrXSum = 0
        GyrYSum = 0
        GyrZSum = 0
        MoSum = 0
        AllSum = 0
        NoOfParticles = 0

        LGroupBound = Smallest + (GroupCount - 1) * SizeStep
        HGroupBound = Smallest + GroupCount * SizeStep

        For i = 0 To 19
            NoOfElAtoms(i) = 0
        Next i

        For Row = Offset To 1000

        Size = (4 * Sheets("Tabelle2").Cells(Row, SizePos) / (3 * Pi)) ^
                  (1 / 3)

            If Size > LGroupBound And Size < HGroupBound Then
                SizeSum = SizeSum + Size
                NoOfParticles = NoOfParticles + 1
                GyrXSum = GyrXSum + Sheets("Tabelle2").Cells(Row,
                   GyrXPos).Value
                GyrYSum = GyrYSum + Sheets("Tabelle2").Cells(Row,
                   GyrYPos).Value
                GyrZSum = GyrZSum + Sheets("Tabelle2").Cells(Row,
                   GyrZPos).Value
                AllSum = AllSum + Sheets("Tabelle2").Cells(Row,
                   AllNoPos).Value

                Counter = 0
```

```
            For ElDesignator = LowerElDesignator To UpperElDesignator
                NoOfElAtoms(Counter) = NoOfElAtoms(Counter) +
Sheets("Tabelle2").Cells(Row, ElDesignator).Value
                Counter = Counter + 1
            Next ElDesignator

        End If


    Next Row

    If NoOfParticles = 0 Then
        SizeMean = 0
        GyrXMean = 0
        GyrYMean = 0
        GyrZMean = 0

        Counter = 0

        For ElDesignator = LowerElDesignator To UpperElDesignator
            Sheets("Tabelle4").Cells(RowOffsetW + GroupCount, LowerElW
+ Counter) = 0
            Counter = Counter + 1
        Next ElDesignator


    Else
        SizeMean = SizeSum / NoOfParticles
        GyrXMean = GyrXSum / NoOfParticles
        GyrYMean = GyrYSum / NoOfParticles
        GyrZMean = GyrZSum / NoOfParticles

        Counter = 0

        For ElDesignator = LowerElDesignator To UpperElDesignator
            Sheets("Tabelle4").Cells(RowOffsetW + GroupCount, LowerElW
+ Counter) = NoOfElAtoms(Counter) / AllSum
            Counter = Counter + 1
        Next ElDesignator


    End If

    Sheets("Tabelle4").Cells(RowOffsetW + GroupCount, GroupPosW) =
      LGroupBound
    Sheets("Tabelle4").Cells(RowOffsetW + GroupCount, NoPosW) =
      NoOfParticles / TotNoOfParticles
    Sheets("Tabelle4").Cells(RowOffsetW + GroupCount, SizePosW) =
      SizeMean
    Sheets("Tabelle4").Cells(RowOffsetW + GroupCount, GyrXPosW) =
      GyrXMean
    Sheets("Tabelle4").Cells(RowOffsetW + GroupCount, GyrYPosW) =
      GyrYMean
    Sheets("Tabelle4").Cells(RowOffsetW + GroupCount, GyrZPosW) =
      GyrZMean
    Sheets("Tabelle4").Cells(RowOffsetW + GroupCount, NoOfAllAtomsW) =
      AllSum


Next GroupCount
```

End of the second section.

```
SizeSum = 0
GyrXSum = 0
GyrYSum = 0
GyrZSum = 0
MoSum = 0
AllSum = 0
NoOfParticles = 0

For i = 0 To 19
    NoOfElAtoms(i) = 0
Next i

For Row = Offset To 1000

    Size = (4 * Sheets("Tabelle2").Cells(Row, SizePos) / (3 * Pi)) ^
(1 / 3)

    If Size > Largest Then
        SizeSum = SizeSum + Size
        NoOfParticles = NoOfParticles + 1
        GyrXSum = GyrXSum + Sheets("Tabelle2").Cells(Row,
          GyrXPos).Value
        GyrYSum = GyrYSum + Sheets("Tabelle2").Cells(Row,
          GyrYPos).Value
        GyrZSum = GyrZSum + Sheets("Tabelle2").Cells(Row,
          GyrZPos).Value
        AllSum = AllSum + Sheets("Tabelle2").Cells(Row,
          AllNoPos).Value

        Counter = 0

        For ElDesignator = LowerElDesignator To UpperElDesignator
            NoOfElAtoms(Counter) = NoOfElAtoms(Counter) +
               Sheets("Tabelle2").Cells(Row, ElDesignator).Value
            Counter = Counter + 1
        Next ElDesignator

    End If

Next Row

If NoOfParticles = 0 Then
    SizeMean = 0
    GyrXMean = 0
    GyrYMean = 0
    GyrZMean = 0

    Counter = 0

    For ElDesignator = LowerElDesignator To UpperElDesignator
        Sheets("Tabelle4").Cells(RowOffsetW + GroupCount, LowerElW +
Counter) = 0
        Counter = Counter + 1
    Next ElDesignator

Else
    SizeMean = SizeSum / NoOfParticles
    GyrXMean = GyrXSum / NoOfParticles
    GyrYMean = GyrYSum / NoOfParticles
    GyrZMean = GyrZSum / NoOfParticles
```

```
        Counter = 0

        For ElDesignator = LowerElDesignator To UpperElDesignator
            Sheets("Tabelle4").Cells(RowOffsetW + GroupCount, LowerElW +
               Counter) = NoOfElAtoms(Counter) / AllSum
            Counter = Counter + 1
        Next ElDesignator


    End If

    Sheets("Tabelle4").Cells(RowOffsetW + NoOfGroups + 1, SizePosW) =
    SizeMean
    Sheets("Tabelle4").Cells(RowOffsetW + NoOfGroups + 1, NoPosW) =
    NoOfParticles / TotNoOfParticles
    Sheets("Tabelle4").Cells(RowOffsetW + NoOfGroups + 1, GroupPosW) = ">"
    Sheets("Tabelle4").Cells(RowOffsetW + GroupCount, GyrXPosW) = GyrXMean
    Sheets("Tabelle4").Cells(RowOffsetW + GroupCount, GyrYPosW) = GyrYMean
    Sheets("Tabelle4").Cells(RowOffsetW + GroupCount, GyrZPosW) = GyrZMean
    Sheets("Tabelle4").Cells(RowOffsetW + GroupCount, NoOfAllAtomsW) =
    AllSum

    End Sub
```

The result of this routine is an Excel-Sheet that contains the number of precipitates as well as the mean chemical composition and the mean radii of gyration of the precipitates in every size range.

Appendix II

The following diagrams illustrate the evolution of the precipitate size distribution upon ageing. On the abscissa the size ranges are indicated while the ordinate represents the relative frequency (i.e. the probability that a precipitate lies within that size range). For finding the precipitates a cluster search algorithm was applied to the datasets.

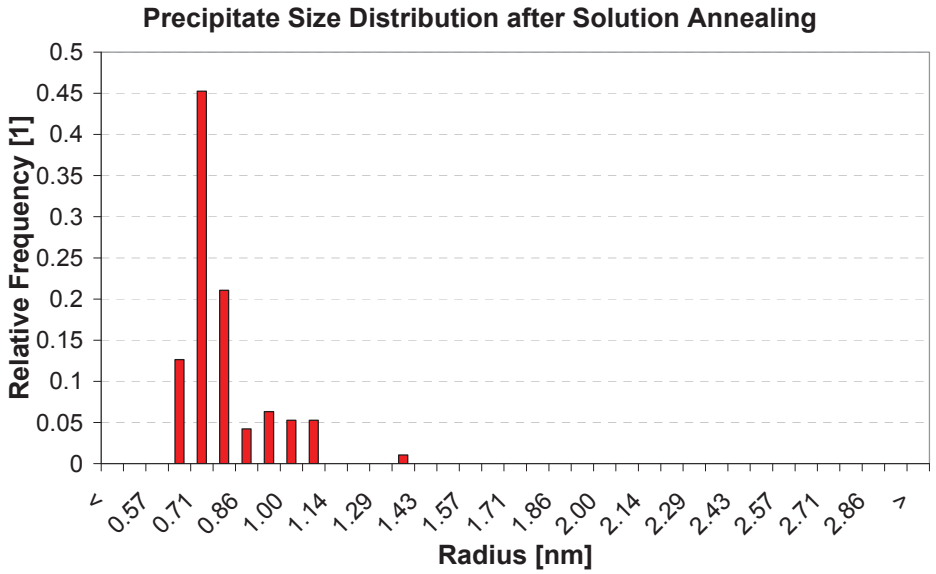

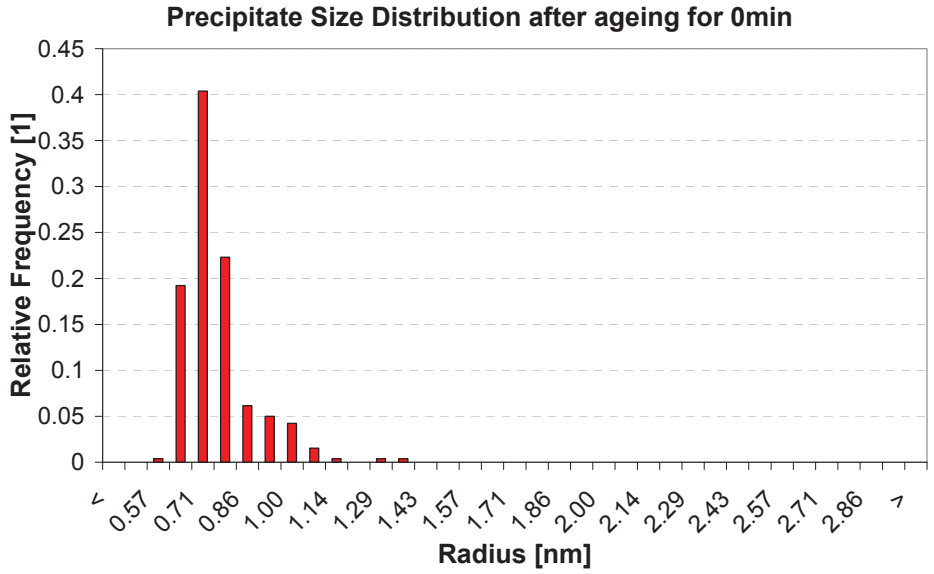

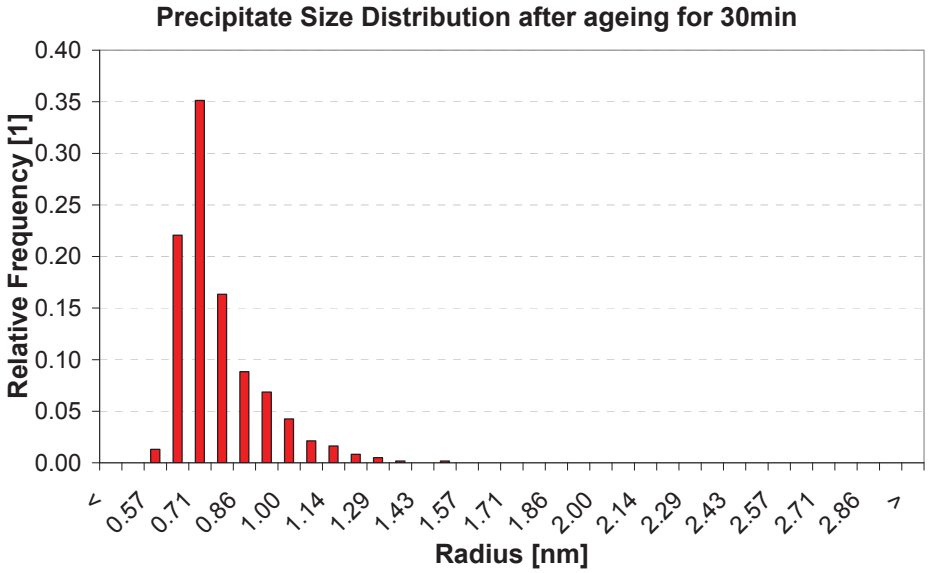
Precipitate Size Distribution after ageing for 30min
Relative Frequency [1]
0.40
0.35
0.30
0.25
0.20
0.15
0.10
0.05
0.00
< 0.57 0.71 0.86 1.00 1.14 1.29 1.43 1.57 1.71 1.86 2.00 2.14 2.29 2.43 2.57 2.71 2.86 >
Radius [nm]

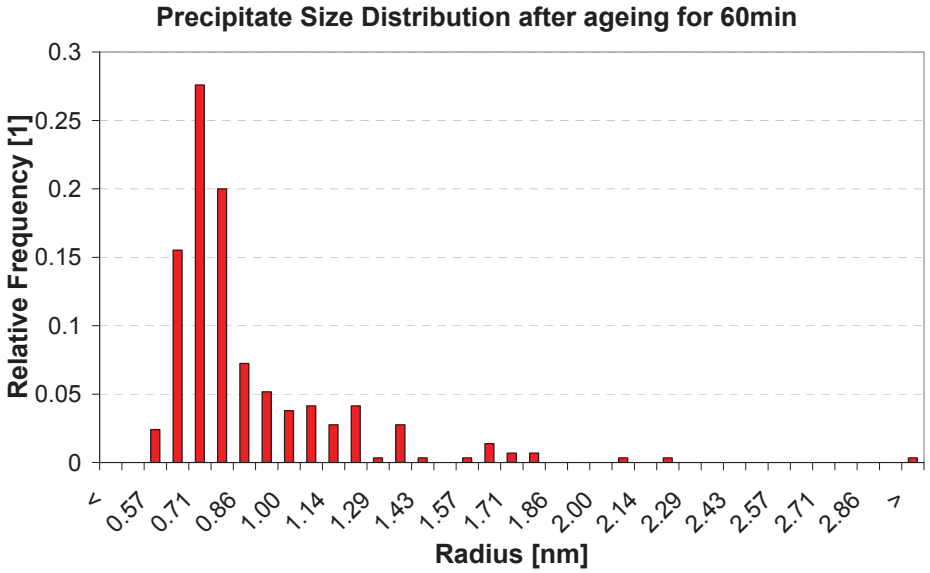
Precipitate Size Distribution after ageing for 60min
Relative Frequency [1]
0.3
0.25
0.2
0.15
0.1
0.05
0
< 0.57 0.71 0.86 1.00 1.14 1.29 1.43 1.57 1.71 1.86 2.00 2.14 2.29 2.43 2.57 2.71 2.86 >
Radius [nm]

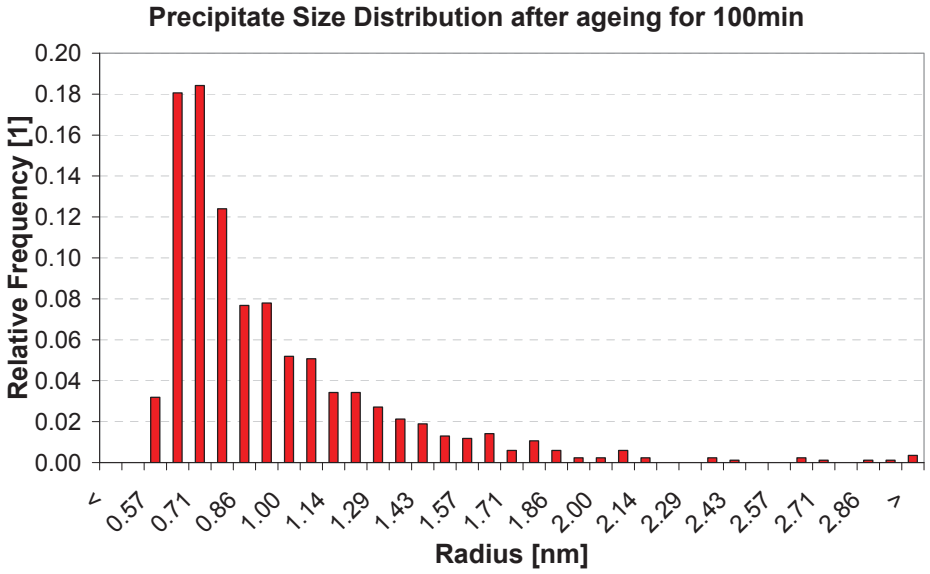
Precipitate Size Distribution after ageing for 100min
Relative Frequency [1]
0.20
0.18
0.16
0.14
0.12
0.10
0.08
0.06
0.04
0.02
0.00
< 0.57 0.71 0.86 1.00 1.14 1.29 1.43 1.57 1.71 1.86 2.00 2.14 2.29 2.43 2.57 2.71 2.86 >
Radius [nm]

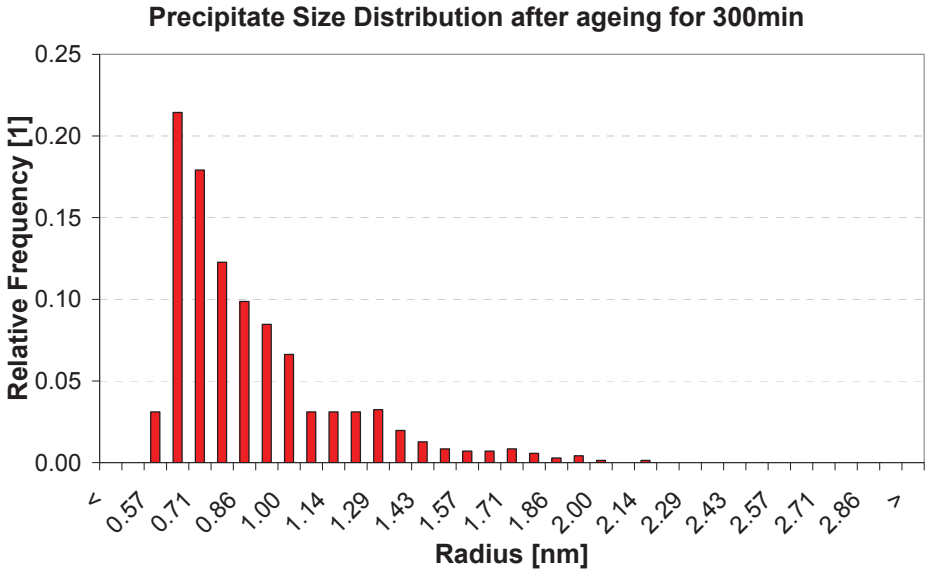
Precipitate Size Distribution after ageing for 300min
Relative Frequency [1]
0.25
0.20
0.15
0.10
0.05
0.00
< 0.57 0.71 0.86 1.00 1.14 1.29 1.43 1.57 1.71 1.86 2.00 2.14 2.29 2.43 2.57 2.71 2.86 >
Radius [nm]

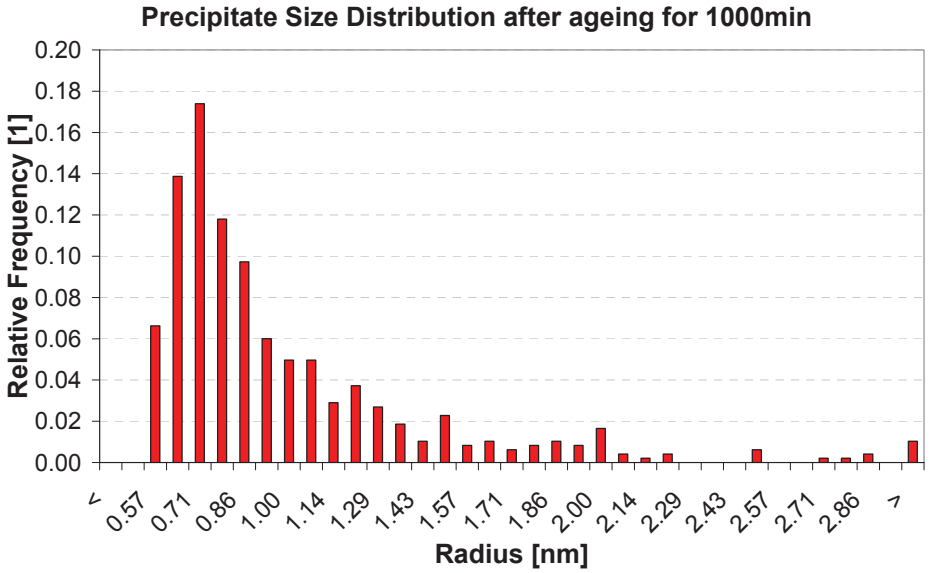
Precipitate Size Distribution after ageing for 1000min
Relative Frequency [1]
0.20
0.18
0.16
0.14
0.12
0.10
0.08
0.06
0.04
0.02
0.00
< 0.57 0.71 0.86 1.00 1.14 1.29 1.43 1.57 1.71 1.86 2.00 2.14 2.29 2.43 2.57 2.71 2.86 >
Radius [nm]

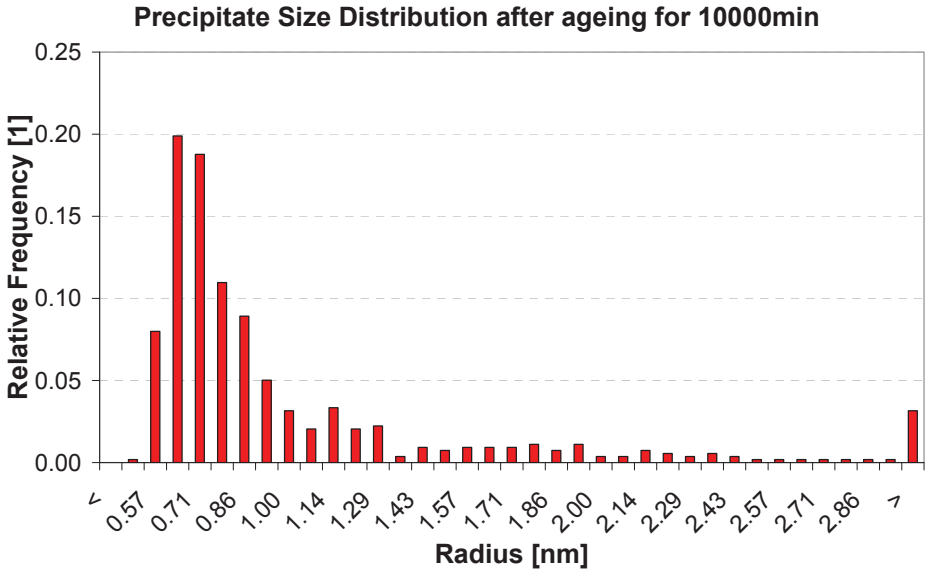
Precipitate Size Distribution after ageing for 10000min
Relative Frequency [1]
0.25
0.20
0.15
0.10
0.05
0.00
< 0.57 0.71 0.86 1.00 1.14 1.29 1.43 1.57 1.71 1.86 2.00 2.14 2.29 2.43 2.57 2.71 2.86 >
Radius [nm]

Here the fraction of precipitate volume fraction that is comprised by precipitates that lie within a certain size range is displayed on the ordinate; the abscissa again indicates the precipitate size range.

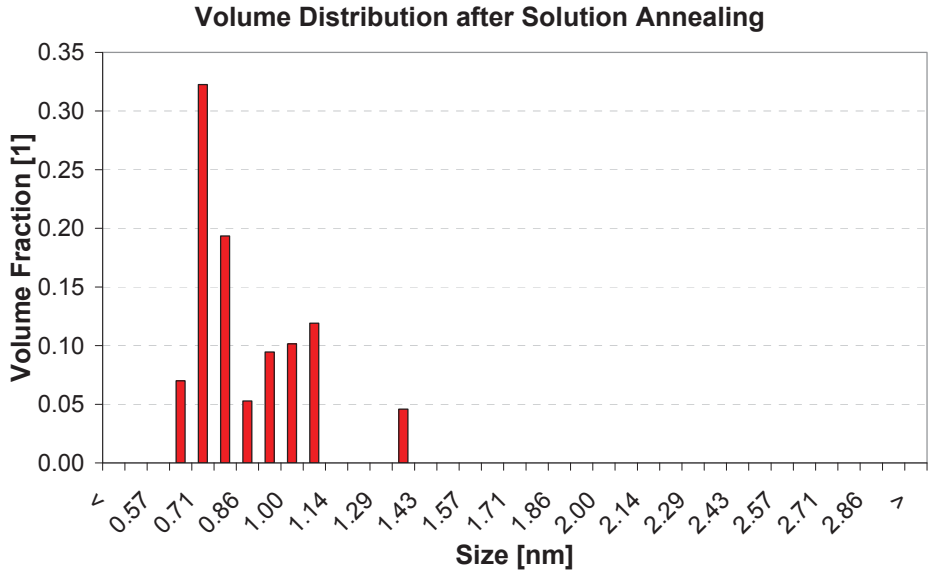

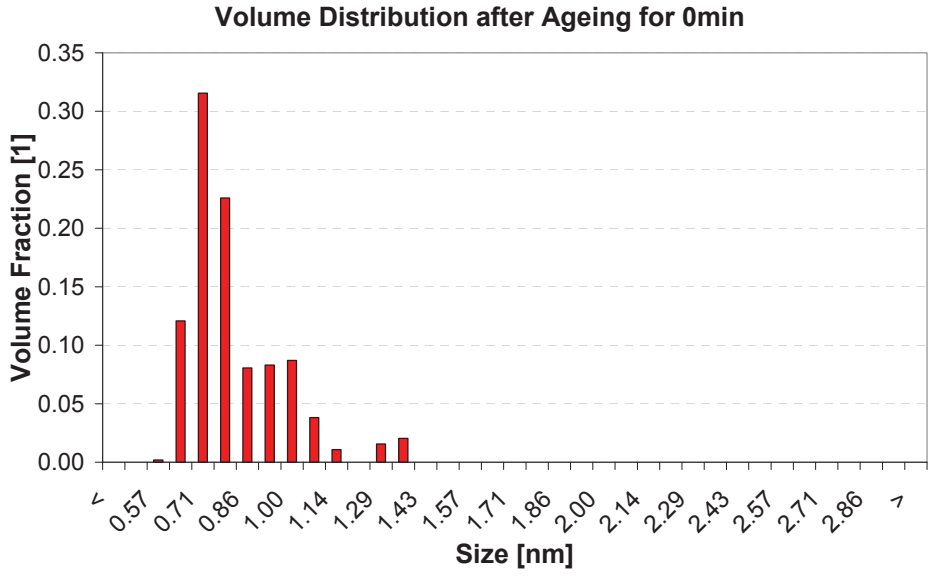

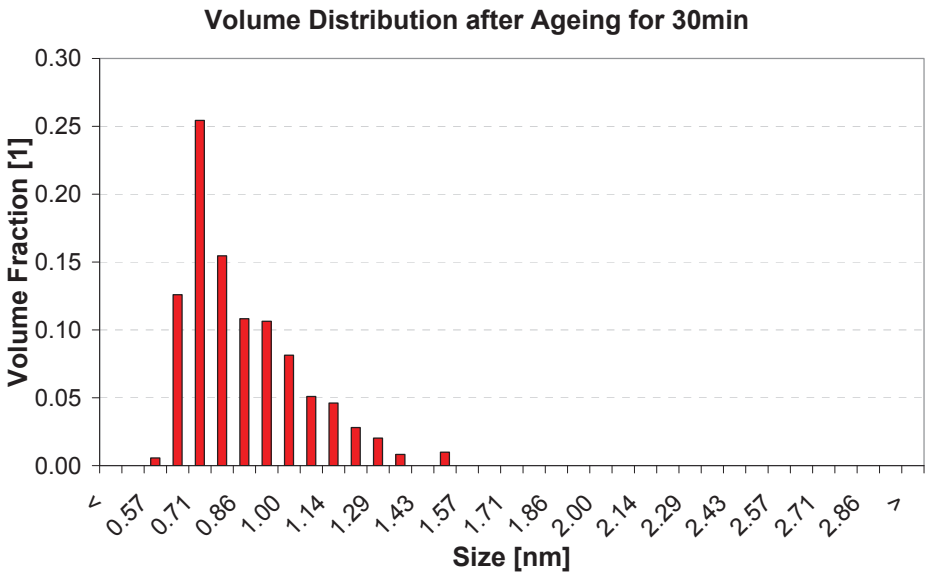
Volume Distribution after Ageing for 30min
Volume Fraction [1]
0.30
0.25
0.20
0.15
0.10
0.05
0.00
< 0.57 0.71 0.86 1.00 1.14 1.29 1.43 1.57 1.71 1.86 2.00 2.14 2.29 2.43 2.57 2.71 2.86 >
Size [nm]

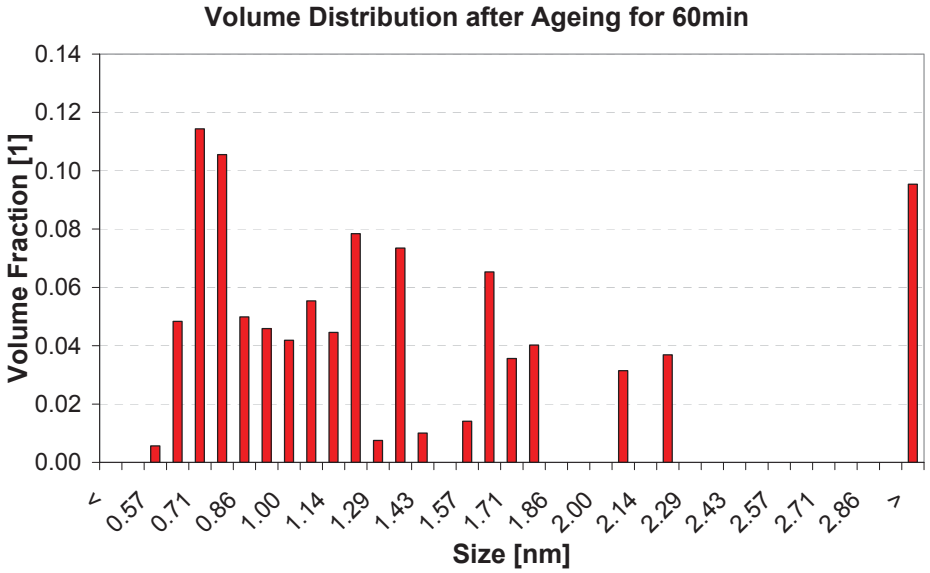
Volume Distribution after Ageing for 60min
Volume Fraction [1]
0.14
0.12
0.10
0.08
0.06
0.04
0.02
0.00
< 0.57 0.71 0.86 1.00 1.14 1.29 1.43 1.57 1.71 1.86 2.00 2.14 2.29 2.43 2.57 2.71 2.86 >
Size [nm]

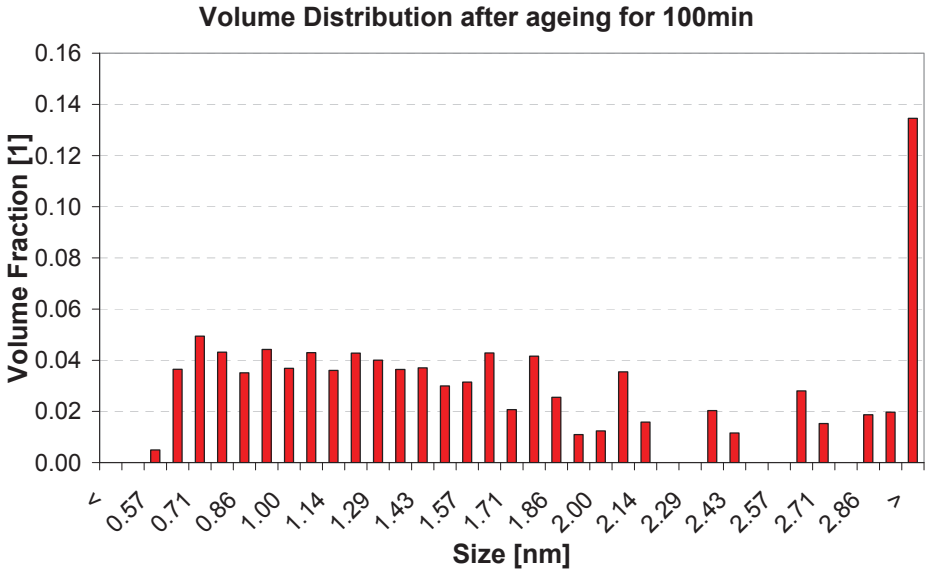
Volume Distribution after ageing for 100min
Volume Fraction [1]
0.16
0.14
0.12
0.10
0.08
0.06
0.04
0.02
0.00
< 0.57 0.71 0.86 1.00 1.14 1.29 1.43 1.57 1.71 1.86 2.00 2.14 2.29 2.43 2.57 2.71 2.86 >
Size [nm]

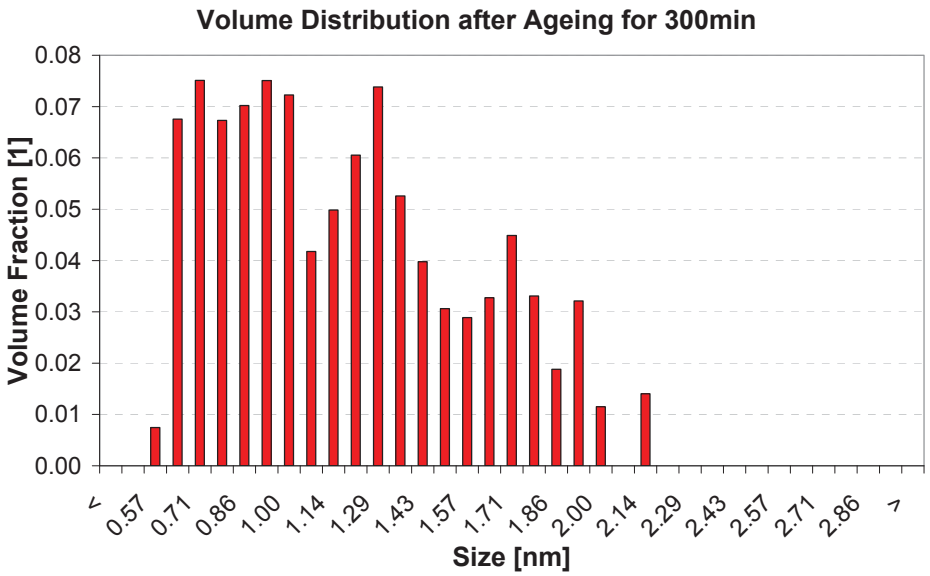
Volume Distribution after Ageing for 300min
Volume Fraction [1]
0.08
0.07
0.06
0.05
0.04
0.03
0.02
0.01
0.00
< 0.57
0.71
0.86
1.00
1.14
1.29
1.43
1.57
1.71
1.86
2.00
2.14
2.29
2.43
2.57
2.71
2.86 >
Size [nm]

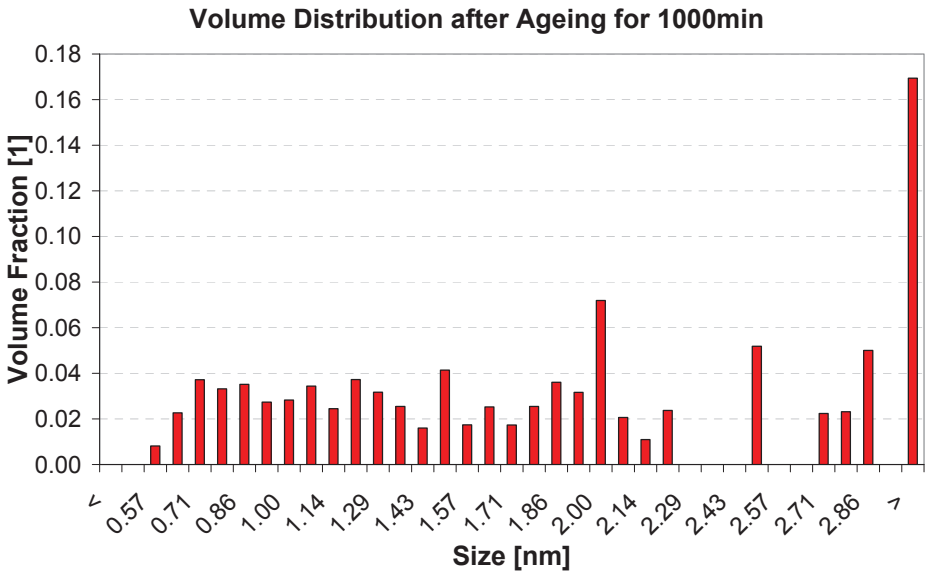
Volume Distribution after Ageing for 1000min
Volume Fraction [1]
0.18
0.16
0.14
0.12
0.10
0.08
0.06
0.04
0.02
0.00
< 0.57
0.71
0.86
1.00
1.14
1.29
1.43
1.57
1.71
1.86
2.00
2.14
2.29
2.43
2.57
2.71
2.86 >
Size [nm]

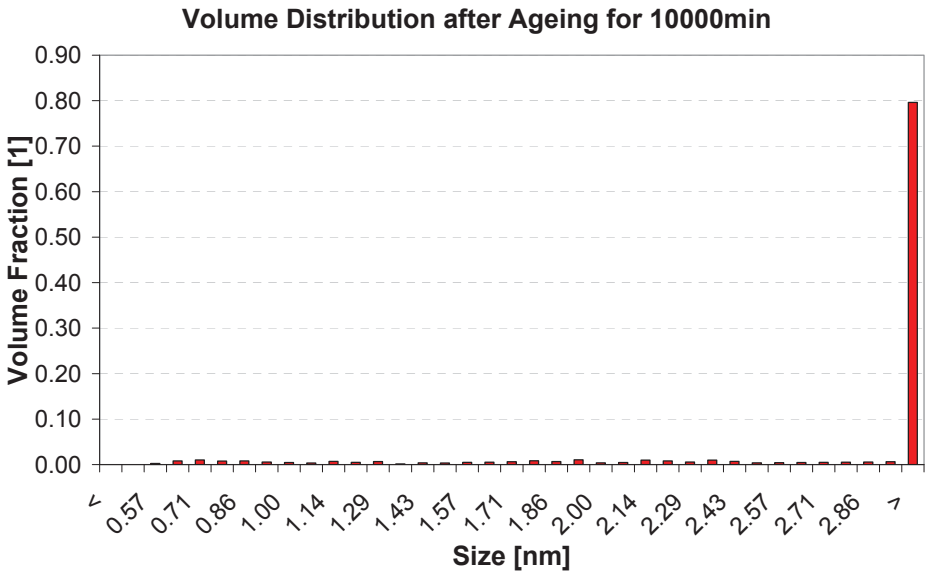
Volume Distribution after Ageing for 10000min
Volume Fraction [1]
0.90
0.80
0.70
0.60
0.50
0.40
0.30
0.20
0.10
0.00
< 0.57
0.71
0.86
1.00
1.14
1.29
1.43
1.57
1.71
1.86
2.00
2.14
2.29
2.43
2.57
2.71
2.86 >
Size [nm]